

AD-A175 777

DEVELOPMENT OF HIGH MODULUS CORROSION RESISTANT
ALUMINUM ALLOYS(U) DREXEL UNIV PHILADELPHIA PA DEPT OF
MATERIALS ENGINEERING M J KOCZAK ET AL. JAN 86

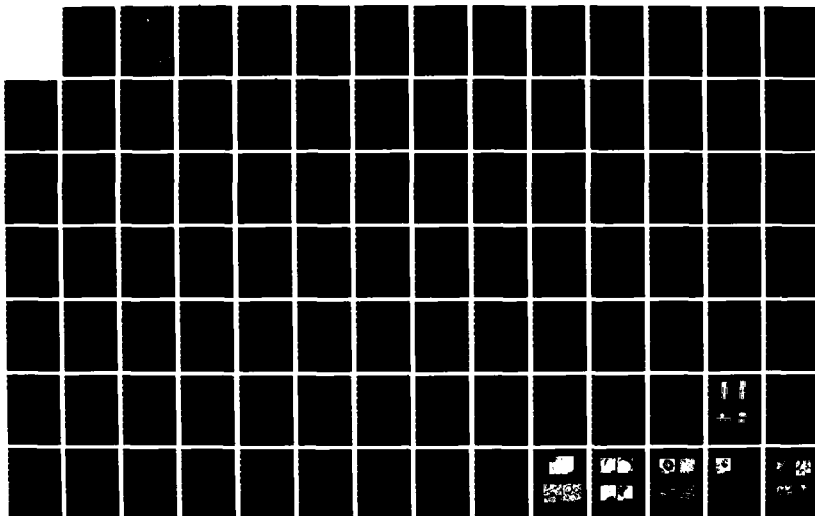
1/2

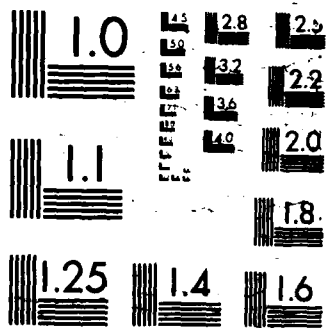
UNCLASSIFIED

NADC-86074-60 N62269-81-R-0743

F/G 11/6

NL





12

REPORT NO. NADC-86074-60

AD-A175 777



DEVELOPMENT OF HIGH MODULUS CORROSION RESISTANT ALUMINUM ALLOYS

Michael J. Koczak and Uday Deshmukh
Drexel University
Department of Materials Engineering
Philadelphia, PA 19104

JANUARY, 1986

FINAL REPORT
CONTRACT NO. N62269-81-R-0743

Approved for Public Release; Distribution is Unlimited

DTIC
ELECTE
S JAN 07 1987
E

FILE COPY

Prepared for
NAVAL AIR DEVELOPMENT CENTER
Department of the Navy
Warminster, PA 18974

UNCLASSIFIED

SECURITY CLASSIFICATION OF THIS PAGE

REPORT DOCUMENTATION PAGE

1a REPORT SECURITY CLASSIFICATION Unclassified		1b RESTRICTIVE MARKINGS	
2a SECURITY CLASSIFICATION AUTHORITY		3 DISTRIBUTION AVAILABILITY OF REPORT Approved for Public Release; Distribution is Unlimited.	
2b DECLASSIFICATION/DOWNGRADING SCHEDULE			
4 PERFORMING ORGANIZATION REPORT NUMBER(S) NADC-86074-60		5 MONITORING ORGANIZATION REPORT NUMBER(S) N/A	
6a NAME OF PERFORMING ORGANIZATION Drexel University	6b OFFICE SYMBOL (If applicable)	7a NAME OF MONITORING ORGANIZATION N/A	
6c ADDRESS (City, State, and ZIP Code) Philadelphia, PA 19104		7b ADDRESS (City, State, and ZIP Code) N/A	
8a NAME OF FUNDING SPONSORING ORGANIZATION Naval Air Development Center	8b OFFICE SYMBOL (If applicable)	9 PROCUREMENT INSTRUMENT IDENTIFICATION NUMBER Contract No. N62269-81-R-0743	
8c ADDRESS (City, State, and ZIP Code) Warminster, PA 18974		10 SOURCE OF FUNDING NUMBERS	
		PROGRAM ELEMENT NO	PROJECT NO
		TASK NO	WORK UNIT ACCESSION NO
11 TITLE (Include Security Classification) Development of High Modulus Corrosion Resistant Aluminum Alloys			
12 PERSONAL AUTHOR(S) Michael Koczak and Uday Deshmukh			
13a TYPE OF REPORT Final	13b TIME COVERED FROM TO	14 DATE OF REPORT (Year, Month, Day)	15 PAGE COUNT
16 SUPPLEMENTARY NOTATION <i>for 8-X1</i> <i>aluminum alloy 7075</i>			
17 COSATI CODES		18 SUBJECT TERMS (Continue on reverse if necessary and identify by block number)	
FIELD	GROUP	SUB-GROUP	
		High Modulus Aluminum, <i>7075</i>	
		Powder Metallurgy, <i>Extrusion,</i>	
		Manganese Addition, <i>Corrosion Testing,</i>	
		<i>Mechanical Testing</i>	
		<i>Microstructure Correlation</i>	
19 ABSTRACT (Continue on reverse if necessary and identify by block number) A program of basic research has been undertaken with the overall goal of establishing quantitative processing-microstructure-mechanical behavior relationships in fully-dense Al-Zn-Mg/Mn modified alloys produced by powder metallurgy. Initial attention has been directed to Mn-Si and Mn-Cr modifications, powder processing, consolidation, mechanical property and corrosion response. Mechanical properties and microstructures have been characterized in the powder in extrusions and correlated with microstructures. Keywords:			
20 DISTRIBUTION AVAILABILITY OF ABSTRACT <input type="checkbox"/> UNCLASSIFIED UNLIMITED <input checked="" type="checkbox"/> SAME AS RPT <input type="checkbox"/> DTIC USERS		21 ABSTRACT SECURITY CLASSIFICATION Unclassified	
22a NAME OF RESPONSIBLE INDIVIDUAL		22b TELEPHONE (Include Area Code)	22c OFFICE SYMBOL

TABLE OF CONTENTS

Page

LIST OF TABLES

LIST OF FIGURES

ABSTRACT

1.0	INTRODUCTION	1
1.1	Objective	1
1.2	Approach	2
2.0	POWDER BLENDED DUPLEX ALLOYS	4
2.1	First Iteration Alloys	4
2.1.1	Summary	4
2.1.2	Structure - Property Optimization Parameters	4
2.2	Second Iteration Alloys	6
2.2.1	Background	6
2.2.2	Material Preparation	6
2.2.2.1	Powder Preparation	6
2.2.2.2	Powder Consolidation and Extrusion	7
2.2.2.3	Heat Treatment and Machining	7
2.2.3	Mechanical Testing	8
2.2.3.1	Tensile Testing	8
2.2.3.2	Impact Testing	9
2.2.3.3	Wear Testing	9
2.2.4	Metallography	10
2.2.5	Summary	11
2.3	Third Iteration Alloys	12
2.3.1	Background	12
2.3.2	Material Preparation	13
2.3.3	Mechanical Testing	14
2.3.4	Metallography	14
2.3.5	Summary	15
2.4	Conclusions	15



Accession For	
NTIS	NTIS
DTIC	DTIC
Unannounced	Unannounced
Distribution/	
Availability Codes	
Dist	Avail and/or Special
A-1	

3.0	PREALLOYING RATIONALE	17
3.1	Background	17
3.2	Prealloyed Compositions	20
3.2.1	Al - Zn - Mg - Cu - Mn Prealloy	20
3.2.2	Al - Zn - Mg - Cu - Mn - Si Prealloy	21
3.2.3	Al - Zn - Mg - Cu - Mn - Cr Prealloy	21
3.3	Material Preparation	22
3.3.1	Powder Preparation	22
3.3.2	Powder Consolidation and Extrusion	22
3.3.3	Heat Treatment and Machining	23
3.4	Testing Procedures	23
3.4.1	Mechanical Testing	23
3.4.2	Corrosion Testing	24
3.4.3	Microscopy Procedures	25
4.0	RESULTS	26
4.1	Mechanical Response	26
4.2	Microstructural Analysis	28
4.3	Corrosion Properties	28
5.0	DISCUSSION	30
5.1	Phase Identification	30
5.2	Microstructural Analysis	30
5.3	Mechanical Behavior	34
5.4	Corrosion Evaluation	41
6.0	CONCLUSIONS	42
	REFERENCES	43
	TABLES	
	FIGURES	

LIST OF TABLES

Table

I	Mechanical Property Data for Powder Blended Duplex Alloys in T6 Temper	52
II	Tensile Test Data for Powder Blended Duplex Alloys* in the O and T6 Temper	53
III	Summary of Processing Parameter/ Property Relations	54
IV	Chemical Compositions of Powders for Duplex Alloys	55
V	Extrusion Parameters for Air Atomized Powder Blended Duplex Alloys	56
VI	Mechanical Property Data for Sieved and Blended Duplex Alloys	57
VII	Wear Test Results	58
VIII	Chemical Analysis of Helium Atomized Al-17 w/o Mn Powder (-325 mesh)	59
IX	Extrusion Parameters for Helium Atomized Powder Blended Duplex Alloys	60
X	Mechanical Property Data for Helium Atomized Blended Duplex Alloys	61
XI	Chemical Analysis of Helium Atomized Mn, Mn-Si, Mn-Cr Modified 7075 Powders	62
XII	Sieve Analysis of Mn, Mn-Si, Mn-Cr Modified Alloy Powders	63
XIII	Extrusion Parameters for Helium Atomized Prealloyed 7075 Powders	64

xiv	Mechanical Property Data for Manganese Modified 7075 Powder	65
xv	Comparison of Modified Alloys at Various Extrusion Temperatures T6 Temper	66
xvi	Comparison of Tensile Properties of Modified Alloys with I/M 7075 and P/M 7090 in T6 Temper	67
xvii	Comparison of Tensile Properties of Modified Alloys with I/M 7075 in O Temper	68
xviii	Phases Present as a Function of Alloy Composition	69

LIST OF FIGURES

Figure

- | | | |
|----|---|----|
| 1 | Duplex microstructure of 7075 + Al-17w/o Mn alloy in the longitudinal section. | 71 |
| 2 | Impact strength, reduction in cross-sectional area, and ultimate tensile strength versus the volume percent of Al-17w/o Mn. | 72 |
| 3 | Microstructure of 20v/o, 75-53 μ m Al-17w/o Mn duplex alloy extrusion in longitudinal section. | 73 |
| 4 | Microstructure of 40v/o, 75-53 μ m Al-17w/o Mn duplex alloy extrusion in longitudinal section. | 73 |
| 5 | Microstructure of 20v/o, <53 μ m Al-17w/o Mn duplex alloy extrusion in longitudinal section. | 74 |
| 6 | Longitudinal section of fractured tensile test bars showing no cracking in Al-17w/o Mn areas. (20v/o, 75-53 μ m, T6 temper, unetched) | 74 |
| 7 | Longitudinal section of fractured tensile test bars showing no cracking in Al-17w/o Mn areas. (40v/o, 75-53 μ m, T6 temper, unetched) | 75 |
| 8 | Longitudinal section of fractured tensile test bars showing microcracking of elongated Al-17w/o Mn areas away from fracture surface. (20v/o, <53 μ m, T6 temper, unetched) | 75 |
| 9 | Longitudinal section of fractured tensile test bars showing microcracking of Al-17w/o Mn areas. (20v/o, 75-53 μ m, O temper, unetched) | 76 |
| 10 | Longitudinal section of fractured tensile test bars showing microcracking of Al-17w/o Mn areas. (40v/o, 75-53 μ m, O temper, unetched) | 76 |

11	Longitudinal section of fractured tensile test bars showing microcracking of Al-17w/o Mn areas. (20v/o, <53 μ m, O temper, unetched)	77
12	Scanning Electron Microscope micrograph of inert gas atomized powders, oversize fraction.	77
13	Scanning Electron Microscope micrograph of inert gas atomized powders, -325 mesh fraction.	78
14	Optical micrograph of inert gas atomized powders, oversize fraction.	78
15	Optical micrograph of inert gas atomized powders, -325 mesh fraction.	79
16	Optical micrographs of duplex alloy extrusions with 20v/o of -325 mesh fraction (a) longitudinal (b) transverse, unetched.	79
17	Optical micrograph of duplex alloy extrusions with 40v/o of -325 mesh fraction, unetched.	80
18	Optical micrographs of duplex alloy extrusions with -325 mesh fraction (a) 20v/o (b) 40v/o , Keller's etch.	80
19	Optical micrograph of fractured tensile bar with 20v/o -325 mesh fraction showing occurrence of failure by crack propagation from an Al-Mn associated void in T6 temper, unetched.	81
20	Optical micrograph of fractured tensile bar with 40v/o -325 mesh fraction showing failure characteristic of the low aspect ratio, air atomized duplex alloys, T6 temper, unetched.	81
21	Optical micrograph of fractured tensile bar with 20v/o -325 mesh fraction showing occurrence of failure by crack propagation from an Al-Mn associated void in O temper, unetched.	82

22	(a) Section of the Aluminum - Magnesium - Manganese - Silicon - Zinc diagram at 730 K and 1% Si. Solid lines, 0% Zn; dotted line, 4% Zn; dashed line, 8% Zn. (b) Aluminum corner of the Aluminum - Chromium - Manganese diagram: phase distribution at 900 K (solid lines) and 820 K (dashed lines).	83
23	Tensile test samples: (a) Room Temperature, (b) High Temperature.	84
24	Corrosion samples: (a) Weight Loss Test, (b) Stress Corrosion Cracking test.	84
25	Vickers hardness versus aging time in minutes representing aging response, alloy aged at room temperature.	85
26	Vickers hardness versus aging time in minutes representing aging response, alloy aged at 120°C.	85
27	Isochronal aging response for a 10 minute time interval during a temperature range of 60°C to 280°C for a 20°C increment.	86
28	Variation of tensile strength with extrusion temperature.	86
29	Variation of yield strength with extrusion temperature.	87
30	Variation of % elongation with extrusion temperature.	87
31	Comparison of mechanical properties in T6 temper of various aluminum alloys. Data for I/M 7075 and I/M 2024 taken from the metals handbook.	88
32	Comparison of mechanical properties in O temper of various aluminum alloys. Data for I/M 7075 and I/M 2024 taken from the metals handbook.	89

33	Comparison of specific mechanical properties in T6 temper of various aluminum alloys. Data for I/M 7075 and I/M 2024 taken from the metals handbook.	90
34	Comparison of specific mechanical properties in O temper of various aluminum alloys. Data for I/M 7075 and I/M 2024 taken from the metals handbook.	91
35	Comparison of notched impact strength of various alloys in T6 and T73 tempers.	92
36	Comparison of tensile strength at elevated temperatures of different alloys. Data for I/M 7075 and I/M 2024 taken from the handbook. Time at test: 10 minutes.	92
37	Comparison of yield strength at elevated temperatures of different alloys. Data for I/M 7075 and I/M 2024 taken from the handbook. Time at test: 10 minutes.	93
38	Comparison of % elongation at elevated temperatures of different alloys. Data for I/M 7075 and I/M 2024 taken from the handbook. Time at test: 10 minutes.	93
39	Figure showing range of strength - elongation combinations obtained for the silicon modified alloy.	94
40	Figure showing range of strength - elongation combinations obtained for the chromium modified alloy.	94
41	Optical micrograph of prealloyed manganese modified inert gas atomized powders, -325 mesh fraction.	95
42	Scanning Electron Microscope micrograph of prealloyed manganese modified inert gas atomized powders, oversize fraction.	95

43	Scanning Electron Microscope micrograph of prealloyed manganese modified inert gas atomized powders, -325 mesh fraction.	95
44	Scanning Electron Microscope micrograph of prealloyed silicon modified helium gas atomized powders, -400 mesh fraction.	96
45	Scanning Electron Microscope micrograph of prealloyed chromium modified helium gas atomized powders, -400 mesh fraction.	96
46	Optical micrographs of the silicon modified alloy in various tempers.	97
47	Optical micrographs of the chromium modified alloy in various tempers.	98
48	Transmission electron micrographs of the manganese modified alloy in T6 temper extruded at 300°C.	99
49	Transmission electron micrographs of the manganese modified alloy in T6 temper extruded at 400°C.	100
50	Transmission electron micrographs of the silicon modified alloy in T6 temper extruded at 300°C.	101
51	Transmission electron micrographs of the silicon modified alloy in T6 temper extruded at 450°C.	102
52	Transmission electron micrographs of the chromium modified alloy in T6 temper extruded at 300°C.	103
53	Transmission electron micrographs of the chromium modified alloy in T6 temper extruded at 450°C.	104
54	Transmission electron micrographs of the silicon modified alloy in as extruded condition at 300°C.	105

55	Transmission electron micrographs of the silicon modified alloy in as extruded condition at 450°C.	106
56	Transmission electron micrographs of the chromium modified alloy in as extruded condition at 300°C.	107
57	Transmission electron micrographs of the chromium modified alloy in as extruded condition at 450°C.	108
58	Fracture surfaces of tensile samples; silicon modified alloy, T6 temper. (a) and (b) extruded at 300°C, (c) and (d) extruded at 450°C.	109
59	Fracture surfaces of tensile samples; chromium modified alloy, T6 temper. (a) and (b) extruded at 300°C, (c) and (d) extruded at 450°C.	110
60	Comparison of weight loss as a function of time. PM represents prealloyed manganese alloy. Corrosion test medium: 1% NaCl + pH2.	111
61	Comparison of corrosion rates of different aluminum alloys. Corrosion medium: 1% NaCl + pH2. Corrosion rate determined by weight loss.	112
62	Plot of increase in critical resolved shear stress with increasing volume fraction and particle size.	113

ABSTRACT

The purpose of this research project was to develop high strength aluminum base alloys with increased modulus and corrosion resistance. In the first stage, processing parameters were established for the preparation of duplex alloys. Based on that experience, the next iteration alloys were air atomized, sieved to a 75-53 μ m and <53 μ m fraction and blended with 7075 powders. The second iteration alloys confirmed the trends made from the first iteration alloys, i.e. reducing the Al-17w/o Mn powder size improves the properties of the alloys. Good strength and ductility result from a 20v/o alloy if the Al-17w/o Mn was sieved to less than 53 μ m. In the third iteration alloys helium was used to atomize the compositions in order to further decrease the powder size. The alloys were sieved to less than 45 μ m and blended with 7075 powder. The resulting alloys had good strength, however, the elongations were low due to poor strain transference. It was observed that there was a critical size for the Al-17w/o Mn powder below which a fine, interlocked, unworkable microstructure existed. The presence of a fine-scale second phase dispersion can improve the strength and elastic modulus of alloys. An Al-Zn-Mg-Cu-Mn type composition, which was later modified with Cr and Si additions has been developed via P/M processing. The alloy chemistries were adjusted to yield between 12-15 volume percent of primary aluminides e.g. $MnAl_6$, Mn_3SiAl_{12} and $(Cr,Mn)Al_{12}$. Prealloyed compositions were helium atomized, canned, degassed and hot extruded at various temperatures with a constant extrusion ratio. The alloys were characterized using optical microscopy, electron microscopy and X-ray diffraction. Ultimate tensile strengths up to 700 MPa (100 ksi), yield strengths up to 650 MPa (90 ksi), elastic moduli up to 81 GPa (11.7 msi) and elongations of the order of 5% have been achieved in the high strength temper. Apart from limited elongation, these properties are superior to I/M 7075 and 2024. Preliminary elevated temperature tests have shown that these alloys exhibit superior strength retention upto 200° C as compared to 2024. The corrosion properties of the alloys are inferior to the I/M 7075 and P/M 7091 alloys. A qualitative analysis of observed room temperature mechanical properties based on Orowan mechanism, microstructure, texturing and particle bonding is presented.

1.0 INTRODUCTION

1.1 Objective

The criteria for material selection in aerospace, both military and commercial are cost and performance. The emphasis may shift, but cost effectiveness over the lifetime of the aircraft is a constant measure. These factors are introducing advanced materials into both existing and new aircrafts.¹ The new generation of aerospace systems currently being developed are expected to have significantly improved capabilities in terms of performance, e.g., range, payload and service life.

As early as the time of the Wright brothers, aluminum alloys have been used to save weight on aerospace structures. At that time, wrought aluminum alloys had low strengths and were not used for aircraft structural members. Higher strengths were achieved by age hardening; but as higher strengths were developed, their ductility, toughness and corrosion resistance decreased. In the 1980's, the aim of the aluminum industry is to produce alloys with decreased density, increased strength while maintaining corrosion resistance. Other considerations involve increasing toughness, elastic modulus, and fatigue resistance, and decreasing the number of parts and fasteners.² It is important to consider the influence of various property improvements on structural efficiency. A recent study indicated decreased density and increased stiffness as the most important parameters, as long as adequate durability and damage tolerance (DADTA) are maintained.³

Many of the ultra high strength or stiffness materials such as beryllium, steels and titanium, alloys are either too expensive or too low in fracture toughness to replace conventional aluminum alloys. The use of metal matrix and epoxy composites have great potential for some applications, however the use is limited due to poor triaxial tensile and in-plane stress properties, high fabrication costs and uncertain DADTA properties. Thus the objective of this program is to develop an advanced aluminum alloy with enhanced specific stiffness and stress corrosion resistance which retains good strength, fracture toughness and fatigue properties. Such an alloy would result in the required performance improvements, yet would still permit conventional design and

manufacturing technology, e.g. powder processing, to be utilized.

1.2 Approach

Powder processing of aluminum alloys is now a commercially viable technology, competitive with conventional ingot metallurgy practice.^{4,5} The high cooling rates achieved in powder atomization result in a fine-scale homogeneous microstructure and minimal solute segregation. Increased alloying flexibility inherent in atomization allows for the production of novel alloys and microstructures which cannot be achieved in conventional ingot casting. The P/M approach is also characterized by a high materials utilization factor, with potential cost advantages particularly in superplastic forming.

Powder metallurgy enables the fabrication of materials having superior properties while maintaining a fine scale microstructure. It is a general rule of metallurgy that the finer the scale of strengthening features, the better the resulting mechanical properties. This conventional wisdom arises because the degree of strengthening obtained by impeding the motion of dislocations with obstacles is inversely proportional to the mean-free-path between the obstacles.⁶ In addition, smaller particles are less apt to serve as fracture initiation sites than larger particles. The aluminum P/M has developed in several areas notably: (i) conventional high strength ingot metallurgy systems,⁷⁻¹⁴ (ii) the development of rapidly solidified powders for aerospace structural applications, e.g., Al-Li, Al-Cu-Li,¹⁵ and (iii) the development of aluminum systems which result in a large volume fraction of an aluminide, e.g., FeNiAl₉, a particulate phase, e.g., SiC, or precipitate phase with concurrent increases in modulus and potential improvements in elevated temperature performance.¹⁶

Traditionally, property improvements in high-performance aluminum P/M alloys have been achieved by developments in the processing technology of powder manufacture and consolidation. Alloys are usually prepared by air/inert gas atomization in which powder size, shape, chemistry and purity are more readily controlled than other methods of powder production. Primary consolidation techniques for these structural powder alloys include direct compaction, e.g., hot isostatic pressing (HIP); the working of a preform, viz., powder forging, powder extrusion; or a

combination of the above processes. Direct powder or billet extrusion and preform forging are the currently preferred approaches for processing aluminum powder alloys.

Recent advances in atomization have resulted in the development of Rapid Solidification Technology (RST). RST is a generic term that refers to fine particulate production ($<40\text{ }\mu\text{m}$) such that high cooling rates are achieved ($>10^4\text{ K/s}$). Such cooling rates result in reduced microsegregation, elimination of low incipient melting temperature phases and ultrafine microstructures. These advantages are balanced by the increased processing difficulties associated with fine powders viz. low apparent densities, higher oxygen levels, pyrophorosity, blending and flow difficulties. The implications of RST processing are currently being examined in several alloy development programs including aluminum alloys, superalloys and specialty steels.¹⁷⁻¹⁹ The combination of processing flexibility and variation in microstructural characteristics available through P/M technology makes it uniquely suitable for the production of alloys to meet the goals of this program.

2.0 POWDER BLENDED DUPLEX ALLOYS

2.1 First Iteration Alloys

2.1.1 Summary

This program is a continuation of some preliminary studies reported in NADC Report #80100-60. In this prefatorial work, a P/M powder blending approach was used to prepare duplex alloys consisting of a high strength 7075 alloy powder, blended with 10, 20 and 40 volume percent of an Al-17w/o Mn powder. Material processing consisted of conventional P/M vacuum hot pressing and hot forging or extrusion to full density. The resulting duplex alloy which comprised a 7075 or 7091 matrix with a dispersed Al-17w/o Mn constituent which consisted of $MnAl_6$ laths enveloped by virtually pure aluminum. An example of this duplex microstructure is shown in Figure 1. The 7075 or 7091 matrix provided toughness and strength; the stiff aluminides provided the modulus contribution, while the inter-lath α -aluminum served to retard stress corrosion cracking.

This initial work revealed, however, that while the alloys exhibited a significant improvement in modulus (16% in the case of the 40v/o alloy), the strength and ductility decreased with increasing volume fraction of the Al-17w/o Mn component. This effect is illustrated in Figure 2 which presents a graphical summary of the results. The results of the preliminary investigation showed that a significant modulus improvement could be achieved by 20 to 40v/o additions of the Al-17w/o Mn component and that the best properties were obtained when the alloy was compacted by the use of direct powder extrusion. Also, the results clearly indicated that while the powder blending technique showed great promise, a substantial amount of alloy development was required to improve the strength and ductility of the resulting alloys.

2.1.2 Structure-property Optimization Parameters

This initial work established the important parameters influencing mechanical properties, i.e. powder and intermetallic size, extrusion temperature and provided guidelines for alloy development and

optimization as detailed below and in Tables I and II.

- i) There was no significant difference in properties between the 7075 and 7091 based alloys. It was noted, however, that in the case of the unblended 7075 and 7091 extrusions, produced for comparison purposes, the 7075 had a much higher strength than could be attained by I/M technology and actually exceeded the strength of the 7091.
- ii) The properties of the duplex alloys improved with increasing deformation during compaction.
- iii) Overaging the 7000 series matrix from the T6 to the O temper condition had a negligible influence on the modulus, but increased the ductility and decreased the strength of the duplex alloys.

The mechanical property trends described were related to the observed microstructural characteristics and the mechanisms operating in the alloys identified. It was found that in the T-6 (full strength) condition, both of the duplex alloys exhibited their maximum yield and ultimate strengths, which were lower than for the matrix phases alone. The duplex alloys had limited ductility in the T-6 condition. The low ductility observed was attributed to crack formation occurring in the Al-Mn areas by a stress concentration in the high modulus phase, the cracks subsequently grow rapidly through the matrix resulting in a low ductility failure.

In the O temper condition, the yield strength of the duplex alloys was slightly higher than the matrix alloys; however, the ultimate strength and ductility were again significantly lower. It should be noted that the O temper condition shows that the duplex alloys had an appreciable amount of inherent ductility. In this case, flow of the matrix phase occurs around the relatively undeformable Al-Mn areas until a stress was reached at which cracks develop in the brittle Al-Mn. These cracks were not expected to propagate so rapidly as in the T-6 condition, since the softer matrix provided some crack blunting.

The modulus of duplex alloys was found to be relatively insensitive to the matrix alloy and its temper condition, since the modulus is principally related to the quantity of the solute elements and volume of the second phase. The improvement in modulus observed in the duplex alloys

was therefore dependent on stress transference to the aluminides by the matrix resulting in the cracking of the Al-17w/o Mn phase.

A correlation of the property data with the microstructural observations, Table III, resulted in recommendations for alloy optimization and are implemented in the second phase.

2.2 Second Iteration Alloys

2.2.1 Background

The preliminary investigation described in Section 2.1 indicated that an improved duplex alloy would be produced if a smaller Al-17w/o Mn powder size were used and/or a larger reduction ratio employed during extrusion. Unfortunately, it was found that if an adequate specimen size was to be maintained, any increase in the extrusion ratio from the 20:1 of the previous work would exceed the capacity of the available extrusion facilities. Thus in these alloys the only parameters investigated were the size and volume fraction of the Al-Mn.

2.2.2 Material Preparation

2.2.2.1 Powder Preparation

The second generation duplex alloys all consisted of a 7075 matrix with an Al-17w/o Mn addition. The powders were air atomized by Gould of Cleveland, Ohio, who also supplied the chemical analyses presented in Table IV.

Air atomized powders were supplied in the unsieved condition and contained a spectrum of powder sizes including a large fraction of coarse particles. To eliminate coarse Al-Mn constituents from these second iteration alloys, the Al-17w/o Mn powder was sieved prior to blending. Two fractions were selected for blending into the duplex alloys: the -200 mesh to +270 mesh (75-53 μ m) fraction and a -270 mesh (<53 μ m) fraction. The sieved Al-17w/o Mn powders were then blended with the unsieved 7075 in a twin shell blender to produce the following three compositions:

7075 + 20v/o Al-17w/o Mn (75-53 μ m)

7075 + 40v/o Al-17w/o Mn (75-53 μ m)

7075 + 20v/o Al-17w/o Mn (<53 μ m)

2.2.2.2 Powder Consolidation and Extrusion

The blended powders were shipped to Nuclear Metals in Concord, Massachusetts for compaction and extrusion. The powders were canned in a 47.50mm (1.870 inch) I.D., 50.80mm (2.000 inch) O.D., 6061 can, cold compacted at 65 tons and then outgassed at 330°C until the vacuum stabilized; the cans were then sealed. Prior to extrusion, the canned powders were preheated at 400°C for 1-3/4 hours before being placed into a 300-ton press with a 51.81mm (2.040 inch) liner at 400°C. The material was then direct powder extruded through a 11.68mm (0.460 inch) die. The extrusion conditions are summarized in Table V.

2.2.2.3 Heat Treatment and Machining

After the consolidation and extrusion operation, all of the alloys were heat treated to the full strength (T6) condition prior to specimen machining. As the constitutional metallurgy of the 7075 matrix was unaffected, the normal 7075 heat treatment schedule was used:

- i) Solution treatment at 465°C (870°F) for 45 minutes,
- ii) rapidly quenching in water at 25°C (78°F),
- iii) aging at 25°C (78°F) for 24 hours, and
- iv) aging at 120°C (250°F) for 24 hours.

At this point, the majority of each alloy was machined into ASTM standard B557, 6.35mm (0.250 inch) diameter round, tension test specimens, with 25.4mm (1.0 inch) gage length and threaded ends. It was found that in this full strength temper condition the alloys machined freely and cleanly. Some of the machined specimens were then heat treated again to put them into alternate temper conditions (Aluminum Development Association standard tempers).

O Temper

The samples that were to be fully annealed were:

- i) Heated to 413°C (775°F) for 3 hours, and
- ii) cooled in air.

T76

- i) Solution treatment at 465°C (870°F) for 45 min.,
- ii) rapidly quenched in water at 25°C (78°F),
- iii) aging at room temperature 25°C (78°F) for at least 24 hours,

- iv) aging at 120°C (248°F) for 4 hours,
- v) aging at 160°C (320°F) for 19-1/2 hours.

T73

- i) Solution treatment at 465°C (870°F) for 45 min.,
- ii) rapidly quenched in water at 25°C (78°F),
- iii) aging at room temperature 25°C (78°F) for at least 24 hours,
- iv) aging at 107°C (225°F) for 7 hours,
- v) aging at 177°C (350°F) for 7 hours.

2.2.3 Mechanical Testing

2.2.3.1 Tensile Testing

The tensile specimens were tested using an Instron TTC tensile testing machine at room temperature, using an Instron extensometer system calibrated to provide a 500:1 magnification on the strain axis. The specimens were loaded at a crosshead speed of 0.5 mm (0.02 inch) per minute.

Ductilities were reported only as percent elongation as it was found that measurements of reduction of area were subject to large variations. To ensure accuracy in the elongation measurements and to preclude the possibility of premature crack initiation from surface irregularities or gage marks, a novel system of marking the gage length was formulated. This consisted of first polishing the specimen gage length down to a 3 μ m finish. A precision ground [25.4 \pm 0.002 mm (1 \pm 0.0001 inch)] masking block was then fitted over the specimen gage length and gold sputtered using a vacuum evaporator. The transition from the gold to the polished alloy surface clearly delineated the gage length, thus permitting the elongation of the failed specimen to be accurately measured using a toolmaker's microscope.

The tensile testing results are summarized in Table VI where it may be seen that the properties of these second generation alloys are superior to those of the initial unsieved alloys (Tables I and II). The alloys with the 75-53 μ m Al-Mn showed some improvement in strength and ductility as compared to their unsieved counterparts, while the 20v/o of <53 μ m Al-17w/o Mn alloy displayed significantly better strength and

ductility. The modulus of the sieved materials was found to be similar to that of the earlier alloys.

These tensile results confirmed the optimization concepts developed from the initial work, i.e. a decrease in the Al-17w/o Mn powder size results in duplex alloys with increased strength and ductility. It should be noted, however, that the ductilities of the alloys, particularly the 40v/o alloy, were low.

2.2.3.2 Impact Testing

Since only subsize impact specimens could be machined from the extrusions, the impact energy that would be absorbed during testing was expected to be low. The specimens were tested using a 0 to 10 ft-lbs Izod impact testing machine. Although the results from this procedure would not allow comparison with standardized tests, they were found to be self-consistent and are presented in Table VI. For comparative purposes, samples of the first iteration alloys were also tested using this procedure, the results being reported in Table II. The tests indicated that while the ductility and strength of the duplex alloys increase with decreasing Al-Mn size, the impact energy decreases.

2.2.3.3 Wear Testing

Samples of the P/M 7075 and of each duplex alloy in the T6 condition were tested for wear resistance using an LFW-1 friction and wear test machine under unlubricated conditions. In this test, a polished, 35.00mm (1.37inch), hardened steel wheel (SAE 4260, Rc 58-63) is rotated at a constant speed and load (72 r.p.m., 40.91 Kg) for a predetermined number of revolutions. Wear coefficients were calculated from the weight loss of the sample block after running the test for 10,000 revolutions. The data obtained from these tests is summarized in Table VII where it can be seen that the wear coefficient varies between 8.1×10^{-5} to 18.4×10^{-5} . The wear coefficient is a measure of the probability of forming a wear particle, thus low values (10^{-6} to 10^{-13}) are typical for lubricated conditions, while higher values represent unlubricated wear. Significant changes in wear rates are usually associated with order of magnitude changes in the wear coefficient. The lowest wear coefficient was obtained for P/M 7075, thus

all of the alloys showed no improvement in wear resistance properties; in fact, a slight decrease in wear resistance was evident.

2.2.4 Metallography

Metallographic sampling of the extruded stock and fractured tensile specimens was performed using a very thin diamond wheel. In preparation for polishing, the samples were mounted in a glass-filled bakelite which gave good edge retention. The samples were then surface ground, polished to 600 grit, then lapped using 1 μ m diamond on a low nap cloth. It was found that this procedure eliminated the tendency of the 0 temper samples to "pick-up" alumina slurry or 6 μ m diamond polishing media. The low nap cloth minimized relief polishing between the relatively soft 7075 matrix and the harder Al-17w/o Mn areas.

To accentuate the microstructure for photomicrography, the samples were sometimes etched in Graff-Sargent Reagent:

0.5 ml HF (concentrated)
15.5 ml HNO₃ (concentrated)
84 ml H₂O
3.0 g CrO₃

Typical microstructures of the duplex alloy extrusions are shown in Figures 3 to 5. It may be seen that the extrusion process resulted in a fully-dense material and that the alloys were workable, showing little evidence of cracking or void formation associated with the Al-17w/o Mn. The structures show no trace of the original interparticle oxide films and are clearly oriented in the extrusion direction.

The microstructure of the 20v/o, 75-53 μ m, Al-17w/o Mn duplex alloy shown in Figure 3 reveals that the aspect ratio of the Al-Mn is, in general, much higher than that found in the first iteration alloys: most particles showing some degree of elongation. In Figure 4, it is evident that the elongation of the 75-53 μ m particles of the Al-17w/o Mn in the 40v/o alloy is slightly more pronounced than in the 20v/o alloy, with virtually all of the particles exhibiting an appreciable aspect ratio. The degree of Al-Mn elongation in the duplex alloy containing 20v/o of <53 μ m Al-17w/o Mn may be seen in Figure 5 to be greater than in the 20v/o of 75-53 μ m alloy.

Metallographic examination of longitudinal sections taken from

tested tensile specimens near the fracture surface revealed a difference in the failure mechanisms operating in the duplex alloys. In the T6 condition, the 75-53 μ m alloys failed in a manner similar to that of the unsieved duplex alloys: rapid brittle fracture occurring as the result of the stress raising effect of an Al-17w/o Mn area cracking. Neither the 20v/o or 40v/o alloy exhibited any evidence of strain distribution away from the fracture surface; this is illustrated in Figures 6 and 7. The duplex alloy containing the 20v/o of <53 μ m Al-17w/o Mn exhibited a slightly different behavior. This is evident in Figure 8 where it may be seen that there is some microcracking of the elongated Al-17w/o Mn areas away from the fracture surface.

In the O temper condition, the fracture behavior of the alloys was different, as may be seen in Figures 9 to 11. The 40v/o alloy (Figure 10) still failed in a manner similar to that observed in the T6 condition; however, the other two alloys displayed markedly different fracture characteristics to those observed in the T6 condition. The 20v/o of 75-53 μ m Al-17w/o Mn alloy is shown in Figure 9, where it is clearly visible that considerable strain transference has occurred over a large volume of the specimen: every Al-Mn particle near the fracture showing at least one crack. This strain distribution behavior was also noted in the <53 μ m alloy (Figure 11) and was found to extend throughout the gage length of the specimen. It should be noted from Figure 11 that the spacing of the multiple cracking occurring in the Al-Mn areas was much smaller in the very high aspect ratio particles, indicating the operation of a more effective stress transfer mechanism.

2.2.5 Summary

The second iteration alloys confirmed the trends made from the initial unsieved duplex alloy study, i.e. reducing the Al-17w/o Mn powder size improves the properties of the alloys (Table III). Good strength and reasonable ductility result from a 20v/o alloy if the Al-Mn was sieved to less than 53 μ m.

The improvement in properties was attributed to a more efficient strain transfer mechanism operating as the particles became more elongated: the more effective stress transfer resulting in finer and more

homogenous microcracking of the Al-Mn, hence reducing the tendency for large isolated cracks which act as stress raisers and propagate in a brittle manner through the 7075 matrix. The mechanism responsible for an increasing aspect ratio with decreasing particle size was not fully identified but is thought to be a feature of interparticle interactions during the extrusion process. This type of mechanism would depend on the volume of 7075 matrix in between the particles, which is a feature of the particle spacing, the elongation increasing as the particle spacing decreases. If the Al-Mn particles are assumed to be spheres of radius, r , distributed in a random manner through the volume as a whole, then the center-to-center nearest neighbor distance $\Delta_{3(R)}$, may be expressed²⁰ as below:

$$\Delta_{3(R)} = 0.554 r \left(\frac{4\pi}{3F_v} \right)^{1/3}$$

where F_v = the volume fraction of the dispersed phase. This relationship implies that the interaction between the particles and matrix elongation would increase with decreasing particle radius or increasing particle volume fraction. This was found to be the case in the duplex alloys, the aspect ratio of the 75-53 μ m Al-17w/o Mn being generally greater in the 40v/o alloy than in the 20v/o alloy; while the 20v/o <53 μ m alloy exhibited more elongation than the 20v/o 75-53 μ m alloy.

2.3 Third Iteration Alloys

2.3.1 Background

The first and second generation duplex alloys clearly indicated that decreasing the Al-17w/o Mn powder size resulted in increasing strength and ductility. The air atomization technique used for these alloys is inherently limited to producing a rather coarse powder, therefore, as mechanical comminution was not practical with the facilities available, a different atomization method was prescribed: Helium atomization. In this inert gas technique, a much finer powder size can be achieved without encountering any significant surface reaction problems. Thus, to achieve a

fine Al-Mn size and uniform blending in the third generation alloys, the Al-17w/o Mn was helium atomized and screened to -325 mesh ($<45\mu\text{m}$). The trends observed in the previous alloys indicated that these finer alloys should show a more highly oriented structure and hence be endowed with better properties than the previous alloys.

2.3.2 Material Preparation

The powder was atomized by Valiment Incorporated of Stockton, California, who also sieved the powder into +325 and -325 mesh fractions and supplied the analysis presented in Table VIII.

The sieved powder fractions supplied were examined using the techniques outlined for the second generation alloys in Section 2.2.2.1. Scanning electron microscopy revealed that the powders were characteristic of inert gas atomization, the oversize fraction being smooth and rounded (Figure 12) while the -325 mesh was smooth and spherical (Figure 13). It was also noted that the -325 mesh powder was of a bimodal distribution, the powder size being mostly above $25\mu\text{m}$, or below $15\mu\text{m}$ diameter.

Optical metallography of the oversize powder showed that this microstructure was very similar to that of the air atomized powders (Figure 14), consisting of relatively coarse, discrete MnAl_6 laths in an alpha aluminum matrix. In the -325 mesh fraction, however, a subtle modification of the microstructure was evident (Figure 15). In these fine powder particles, the intra-particle structure consists of a greater number of finer MnAl_6 laths, the laths touching each other in all but the biggest particles.

The -325 mesh Al-17w/o Mn powder fraction was blended with the unsieved, air atomized 7075 powder to give alloys of the following composition:

7075 + 20v/o Al-17w/o Mn ($<45\mu\text{m}$)

7075 + 40v/o Al-17w/o Mn ($<45\mu\text{m}$)

The same procedure was followed as for the second generation alloys (Section 2.2.2.2), the consolidation and extrusions again being performed by Nuclear Metals. The only difference in schedule was slightly different preheating conditions prior to extrusion: 2.5 hours at 390°C . The

extrusion conditions are summarized in Table IX where it may be seen that the 40v/o extrusion exhibited severe "fir treeing" along virtually its entire length.

A length of the 40v/o alloy long enough to machine a single tensile bar form was located; then identical heat treating and machining schedules to those employed for the second iteration alloys (Section 2.2.2.3) were used for both alloys. It was found that the alloys machined freely and cleanly in all temper conditions.

2.3.3 Mechanical Testing

The one specimen of the 40v/o alloy and the samples of the 20v/o alloys were tested in the manner described for the second generation alloys in Section 2.2.3.1; the results are summarized in Table X. It may be seen from these tests that while the strength of the alloys was higher than those of comparable second iteration alloys, the ductilities were no better, or worse, depending on temper.

Impact testing was carried out using the same method as that described in Section 2.2.3.2. The results are summarized in Table X, which on comparison to Tables II and VI, reveals that this 20v/o of <53 μ m Al-17w/o Mn alloy had very poor impact properties. This reflects the trend observed in the preceding work in which the impact resistance decreased with decreasing Al-Mn powder size.

Specimens of the 20v/o and 40v/o alloy were tested for wear resistance in a similar manner to that described in Section 2.2.3.3. The results are summarized in Table VII, where it may be seen that the alloys have less wear resistance than the comparable air atomized powder alloys, which in themselves were inferior to the P/M 7075.

2.3.4 Metallography

Metallographic sampling of the extruded stock and fractured tensile specimens was performed using the techniques specified in Section 2.2.4.

Representative microstructures of the 20v/o alloy extrusions in the unetched condition are shown in Figure 16. It may be seen that although the material is largely fully dense and that there is no evidence of

interparticle oxide, there is occasional cracking and void formation associated with the Al-17w/o Mn powder constituent. It should also be noted that each individual Al-Mn powder particle shows virtually no elongation in the extrusion direction.

Figure 17 shows the microstructure of the 40v/o alloy which, despite the gross "fir tree" cracking, shows some elongation of the Al-Mn and no evidence of the Al-Mn associated cracking or voids. Examination of the microstructures of both alloys at higher magnifications in the etched condition revealed that the Al-Mn areas were of a different structure to that observed in the air atomized powders (Figure 18) where it may be seen that instead of discrete $MnAl_6$ laths, as was observed in the previous alloys, the Al-Mn areas contained a network of interlocking, coarsened aluminides.

Samples taken from fractured tensile specimens reflected the poor strain transfer occurring due to the lack of aspect ratio of the Al-Mn constituent. In the T6 condition, it appears that in the 20v/o alloy failure occurred by crack propagation from an Al-Mn associated void (Figure 19); while in the 40v/o alloy, the fracture characteristics (Figure 20) were similar to those of the low aspect ratio, air atomized duplex alloys. In the O temper 20v/o alloys, as shown in Figure 21, there is some evidence of strain transfer with some cracking of Al-Mn particles; however, the majority of the cracks near the fracture appear to be nucleating at Al-Mn associated voids.

2.3.5 Summary

These third generation alloys did not follow the trend established by the first two iterations. In these alloys, the reduction in size of the Al-17w/o Mn powder did produce a small increase in strength, but the anticipated increases in ductility were not observed.

The poor ductility of the alloys was attributed to the lack of elongation of the Al-Mn during extrusion. This not only gave poor strain transference in the final alloy, it also prevented full density being attained during extrusion, and hence promoted cracking from the pre-existing voids. The 40v/o alloy showed some elongation of the Al-Mn, however, it exhibited a severe "fir tree" effect during extrusion.

The poor hot workability of the helium atomized Al-17w/o Mn powder was attributed to its very fine structure. This fine structure was a feature of the atomization process used, which tended to produce small droplets of molten metal. Because of the high surface of volume ratio and the high conductivity of the inert helium atmosphere, the cooling rate experienced by these small droplets is very high. This rapid cooling results in a high nucleation rate for the aluminides and hence produces a very fine structure in the resulting powder. It may be seen from the spacing expression in Section 2.2.5 that reducing the aluminide size will result in a reduction in aluminide spacing for a constant volume fraction, until at some point the aluminides will touch. It is believed that in the -325 mesh, helium atomized powder, this has occurred, and that during the extrusion preheating cycle the aluminides have interlocked to form a semi-continuous, rigid network within each Al-17w/o Mn powder particle. The high hardness coupled with an aluminide "skeleton" could drastically reduce the hot workability of the Al-Mn powder.

2.4 Conclusions

It has been shown that the properties of these powder blended duplex alloys can be improved by decreasing the size and increasing the aspect ratio of the Al-17w/o Mn constituent in the final extruded product. The work has also shown that there is an unforeseen, inherent limitation of the extent to which this goal can be achieved, thus placing a restriction on the optimization of these alloys before their full potential was attained. The cutoff point for optimization appears to be defined by a lower limit on the size of the Al-17w/o Mn powder. Below this critical size, the cooling rate experienced by the Al-17w/o Mn during atomization results in a fine, interlocked, unworkable microstructure.

3.0 PREALLOYING RATIONALE

3.1 Background

The objective of this program is to develop an aluminum alloy with enhanced modulus, superior strength, good corrosion resistance, which still maintains reasonable fracture strength and can be utilized by established aerospace technologies. It is important to identify the shortcomings of the presently available high strength aluminum alloys:

(1) The Young's modulus of the alloys is virtually independent of temper conditions and depends on the alloying additions. Magnesium significantly lowers the modulus of aluminum alloys, but is an essential constituent of the age hardening precipitate, $MgZn_2$.²⁰⁻²⁴

(2) High strength aluminum alloys have poor stress corrosion resistance in the peak aged (T6) temper. 1/M 7075 typically has a U.T.S of 572 MPa (83 ksi), but the SCC threshold for the 7075 extrusions in the short transverse direction is less than 55.12 MPa (8 ksi).²⁵

(3) Increasing volume fraction of $MgZn_2$ increases the strength, but decreases fracture toughness and corrosion resistance.²⁵⁻³²

(4) The application and service of high strength aluminum alloys is limited by their poor fatigue properties.^{28,33}

(5) The comparatively low fracture toughness of most high strength aluminum alloys imposes design and application limitation.²⁸

All the above factors combine to abrogate the high strengths of currently available aluminum alloys. This results in lower performance and/or shorter lifespan of aerospace systems. Development of techniques to overcome these shortcomings would require an understanding of the mechanisms responsible for these shortcomings.

The rapid decrease in fracture toughness with increasing solute content in all high strength aluminum alloys is due to a reduction in ductility combined with an increase in strength. Work on 7000 series alloys²⁷ has shown that the fine semi-coherent $MgZn_2$ present as the strengthening precipitate in the T6 condition promotes local shear instabilities during deformation. In a precipitation hardening alloy that has small coherent or semi-coherent precipitates which are below the critical

diameter (d_c) for dislocation bypassing to occur, the dislocations cut through these precipitates.³⁴ This leads to the softening of the slip band since each dislocation passing through these precipitates reduces the shear resisting cross section of the particle. Hornbogen and Gahr³⁵ have demonstrated the connection between precipitate cutting and the formation of coarse slip bands. The equation developed predicts that the tendency for coarser slip is more pronounced the higher the volume fraction of the particles and smaller particle sizes. This "work softening" has been shown to occur in Fe-Ni-Al alloy by Hornbogen and Gahr³⁶ and in 7000 series alloys by Ludtka and Laughlin.²⁷ Therefore for the same macroscopic strain there is more strain localization for a given slip band in the alloys containing higher volume fraction of shearable precipitates. This can cause void nucleation at the grain boundaries³⁷ at earlier macroscopic strains or under plane strain conditions may result in microcracking.³⁰ This microscopic slip localization can therefore affect macroscopic properties such as ductility and toughness.²⁷

The fatigue properties of high strength aluminum alloys in their full strength condition have also been found to be closely related to fatigue crack initiation by planar slip.³⁷ Fatigue deformation and crack initiation are strongly dependent on microstructure and cyclic slip behavior.³⁸ Fatigue cracks nucleate directly at intense slip bands or indirectly by grain boundary cracking, by particle matrix interface decohesion, or by particle fracture, as dislocation pile-ups reach a critical value. Therefore the fatigue crack initiation (FCI) resistance is enhanced by homogeneous deformation and slip length shortening. Microstructurally small grains and fine particles enhance FCI. This latter requirement is in direct conflict with that for good fracture toughness. Fatigue crack propagation resistance (FCP) on the other hand increases with increasing grain size. This is attributed to the dislocation slip being more reversible, or to less plastic strain being accumulated, or to greater degree of crack closure.

Stress corrosion cracking (SCC) of high strength aluminum alloys has traditionally been mitigated by overaging the alloys to the lower strength T7 condition. It is generally accepted that the decrease in stress corrosion susceptibility imparted by this overaging treatment is due to a

modification in grain boundary structure and chemistry.^{25, 29} The results of Joshi, et. al³⁹ show that in the peak aged (T6) condition there is more solute in the grain boundaries than in the overaged (T7) condition. This leads to a lower susceptibility for SCC in T73 temper. Other explanations based on the action of hydrogen in these alloys were considered invalid since it was difficult to rationalize how the extremely slow lattice transport of hydrogen in aluminum would allow it to keep up with the moving crack. Recent work has shown however that hydrogen transport can be greatly enhanced in the T6 condition by the presence of planar slip. The localized planar shear instabilities ahead of the crack tip have two-fold effect: first, they produce steps or jogs in the crack surface, disrupting the oxide barrier and hence allowing the penetration of hydrogen into the lattice; second, the shear planes promote rapid transportation of hydrogen by pipe diffusion and hence facilitate hydrogen embrittlement of the structure ahead of the crack tip. This phenomenon has been demonstrated in the T6 temper.⁴⁰ This effect is not seen in T73 temper since the precipitates are incoherent and do not promote planar slip.

Thus the major shortcomings in the presently available high strength aluminum alloys could be rectified by suppression of planar slip. Localization of planar slip can be overcome by the addition of fine, incoherent dispersion such as oxides in P/M alloys. This size of dispersoids is critical if good properties are to be obtained. Fine incoherent dispersoids increase the strength of the alloy by making the dislocations bow around them. This results in the formation of dislocation loops around the dispersoid particles. As more and more loops are generated, it becomes difficult to move the successive loops at a given stress level thereby increasing the yield strength of the alloy. There are two independent variables that control the dispersion, viz., particle size and volume fraction. The yield strength can be increased either by decreasing the particle size or by increasing the volume fraction of the dispersoid particles. The former results in a more significant increase even at modest levels of volume fraction. This is because the decrease in mean free path for dislocation motion is affected more by the particle size. As enumerated previously, having fine particles is highly desirable since they suppress coarse slip.

Also a large dispersoid usually decreases the fracture toughness, as it either cracks or decoheres in the plastic zone ahead of the crack tip, while a small dispersoid if semi-coherent may be sheared. Particles in the range of $0.05\mu\text{m}$ to $0.1\mu\text{m}$ in diameter, such as those added to control recrystallization and grain growth, do not affect the fracture toughness as long as they do not nucleate void sheets.

If this dispersoid is an intermetallic phase with high stiffness, then the Young's modulus of the alloy as a whole will be increased. Thus this addition will not only improve the strength but also the modulus of the alloy. The 7075 alloy composition was selected to be modified by this approach. The determining factors in the choice of high strength alloy were the good literature base available and the excellent tensile strength of the P/M 7075 T6 reference specimens produced as a part of the powder blending investigation.

3.2 Prealloyed Compositions

3.2.1 Al-Zn-Mg-Cu-Mn Prealloy

The effect of various alloying elements on the Young's modulus of aluminum has been studied by Dudzinski^{21, 22} and others.²³ Most of the transition elements increase Young's modulus of aluminum. Among them manganese is one of the most effective alloying elements. This is due to its dual action. Manganese in solid solution increases the Young's modulus of the alloy, however, a more significant contribution comes from the formation of high modulus intermetallics. The first modification of 7075 alloy therefore constituted addition of manganese.

Examination of the phase diagram reveals that manganese would form MnAl_6 as the intermetallic phase. This was confirmed by melting a small amount in the laboratory. Since a very fine dispersoid was required, it was decided to produce the dispersoid via a P/M route as an I/M route would produce a coarse intermetallic, and refinement of these particles by subsequent processing is limited as they are thermally quite stable. Based on the results of duplex alloys,⁴¹ additions of 3.6 wt.% manganese to a 7075 base alloy were formulated. To achieve a sufficiently fine dispersion of MnAl_6 , a P/M route was adopted. Finer powders with high cooling rates

result in a finer dispersion, therefore it was decided to helium atomize the powders and sieve them to -325 mesh. Helium gas was used because it has better thermal conductivity, a rapid heat extraction by the gas medium, and increased cooling rates, resulting in a finer MnAl_6 dispersion.

3.2.2 Al-Zn-Mg-Cu-Mn-Si

Alternatively, two further modifications were considered. Since the manganese addition resulted in an alloy with very low ductility, it was decided to change the structure of the intermetallic phase. MnAl_6 is orthorhombic in nature and thus has a limited ductility because of limited availability of slip systems. If, therefore, a cubic intermetallic could be substituted, it was expected to result in better ductilities in the alloy. Literature^{42, 43} indicated that a ternary intermetallic of manganese, silicon and aluminum- $\text{Mn}_3\text{SiAl}_{12}$ was cubic and had limited ductility. It was anticipated that there would be a small loss in the modulus as this intermetallic is not as stiff as MnAl_6 . Based on the stoichiometry and phase diagram considerations, Figure 22a, 1 wt.% of silicon was added to partition manganese with aluminum and prevent any formation of MnAl_6 .

3.2.3 Al-Zn-Mg-Cu-Mn-Cr

The manganese modification of 7075 resulted in an alloy with better Young's modulus but with limited ductilities. The specific contribution was reduced because of substitution by an element with a high atomic weight. To further increase the specific modulus, there were two options:

- (1) An alloying constituent which for an equal weight addition forms an intermetallic of the same modulus as MnAl_6 , but with higher stiffness.
- (2) An alloying constituent which for an equal weight addition forms an intermetallic of the same stiffness as MnAl_6 , but of larger volume.

The literature^{22, 44-48} indicated that the simultaneous addition of chromium and manganese to aluminum would increase the Young's modulus more than manganese in isolation. This increase is the combined result of a

solid solution effect and the precipitation of $(\text{Cr,Mn})\text{Al}_{12}$, which is of lower density and higher stiffness than MnAl_6 . Due to the very low diffusivity of chromium in aluminum, this phase has extremely good thermal stability, but when present in large volume fractions, causes a drastic reduction in the ductility of pure aluminum. Examination of the phase relationships as seen in Figure 22b, between manganese, chromium and the 7075 constituents⁴⁹ indicated that at the high cooling rates only $(\text{Cr,Mn})\text{Al}_{12}$ should be present. During subsequent processing, however, it is possible for some reaction to occur with magnesium, and the equilibrium phases $\text{Cr}_2\text{Mg}_3\text{Al}_{18}$ and MnAl_6 may result⁵⁰. Provided this transformation can be suppressed, the chromium addition would prove beneficial, providing an increase in specific modulus with no loss of strength due to Mg partitioning.

The chromium present in solid solution would severely interfere with the MgZn_2 precipitation from the 7075 constituents. This is due to the vacancy sink effect of chromium, which would result in heterogeneous nucleation of MgZn_2 on the dispersoid, oxides and grain boundaries.⁵¹ This quench sensitivity may be reduced by the addition of small amounts of silver which is known to suppress the nucleation barrier for MgZn_2 precipitation. The modified 7075 was expected to show all of the advantages of the manganese modified alloy, yet have better specific modulus and be less sensitive to processing.

3.3 Material Preparation

3.3.1 Powder Preparation

As mentioned earlier, the prealloyed compositions were helium atomized by Valimet Incorporated of Stockton, California who also sieved the powder into +325 and -325 mesh. The chemical compositions of the three alloys is shown in Tables XI and XII. After atomization, the powders were shipped to Nuclear Metals Incorporated of Concord, Massachusetts for degassing and consolidation.

3.3.2 Powder Consolidation and Extrusion

The extrusion route followed was exactly the same as outlined in section 2.2.2.2. The hot extrusion parameters were similar to those given in

Tables V and IX and are given in Table XIII. The precompaction and extrusion parameters for these RST powders require more careful control. A range of extrusion temperatures was investigated since the aluminides may coarsen rapidly,⁵² particularly during deformation at high temperatures, whereas at low temperatures poor consolidation, i.e., poor powder bonding, may result. The extrusion ratio was kept constant for all cylindrical extrusions at 16:1. In addition, a plate extrusion was extruded at a ratio of 32:1.

3.3.3 Heat Treatment and Machining

The atomized and consolidated alloys were tested mainly in T6 and O tempers. Occasionally the alloys were tested in T73 temper. As the constitutional metallurgy of the 7075 matrix was unaffected, the normal 7075 heat treatment schedule was used as outlined in section 2.2.2.3.

3.4 Testing Procedures

3.4.1 Mechanical Testing

The tensile bars were machined in accordance to ASTM standard B557, 0.25 inch round, with 1.0 inch gage length and threaded ends and tested in a similar manner as outlined in section 2.2.2.3. Some high temperature tensile testing was also conducted to determine the response of these alloys at high temperature. The specimen geometry, as depicted in Figure 23, had one modification. Since it was intended to monitor the yield strength at high temperature, strain measurements were required. The tensile specimen was therefore modified so as to have a ridge at the two ends in order to calculate the 0.2% offset yield strength rather accurately. An electrically heated radiation type furnace was used to heat the samples to the required temperatures. The temperature control was exercised by varying the power input to the furnace through a variac. The test was started after the sample had reached the required temperature and was held there for 10 minutes. Considering all the times, the exposure at a temperature would be of the order of half an hour.

Since the extrusion diameter was only 12.7 mm (0.5 inch), standard impact specimen could not be machined. Therefore, subsize specimen of the modified alloys and identical specimen of X7091 were used

for making comparison. The specimens were tested using a 0-10 ft.lbs. Izod impact testing machine.

3.4.2 Corrosion Testing

Corrosion testing was performed utilizing weight loss test. Effort to determine the susceptibility of the modified alloys towards SCC met with limited success. Weight loss tests prove to be a very simple method of determining general corrosion rate of an alloy. In this test, loss in weight after immersion in a corrosive medium is monitored as a function of time. Samples for weight loss test were prepared by machining the heat treated rods into small buttons 8.89 mm (0.35 inch) in diameter and 1.27 mm (0.05 inch) thick with a small hole close to the circumference. Next, they were surface ground on a 600 grit paper to remove the machining marks and also to make all the surfaces uniform. The buttons were then weighed tied to a rod by means of a thread and suspended in the corrosion medium consisting of 1% NaCl + pH2 prepared in distilled water. After regular intervals of time, the samples were removed, cleaned in acetone using an ultrasonic cleaner, dried, and weighed again. The loss in weight was taken to be that resulting from the corrosion of the samples. Corrosion rate was calculated as weight loss/area.time. Since this is not a standardized test, absolute values from the test cannot be compared; therefore, the alloys were always tested with some standard alloy such as 7075 or X7091 in the T6 and T73 conditions. The SCC test was conducted on the specimens developed by NADC,⁵³ shown in Figure 24a. The test procedure is detailed below.

Heat treated samples were machined to the required geometry. A test sample was stressed by tightening the screw and the slot width measured. After unloading, the width was noted again. No change in width during this loading-unloading cycle was taken as elastic loading. The smallest change in width during the cycle and the corresponding deflection was taken as the yield point. Then the remaining samples were loaded to a fraction of that deflection, i.e., fraction of the yield strength (e.g. 75%). Later on, the stress corresponding to that deflection was calculated. The loaded samples were kept in a corrosive environment and visually observed at regular intervals of time. The time when the first crack was seen was

noted, and various samples were rated on the basis of time they took to crack. Thus, it can be seen that this is not a very quantitative test and gives only the propensity of crack initiation in the alloys. Nevertheless, it serves as a good screening test for rating the corrosion response of different alloys.

3.4.3 Microscopy Procedures

Samples for metallographic observation were taken from the as extruded stock as well as from the heat treated and fractured samples. In preparation for polishing, the samples were mounted in bakelite, surface ground, polished to 600 grit, and lapped using 6 μ m and 1 μ m diamond pastes on a low nap cloth. After polishing, the samples were etched with various reagents, e.g. Keller's, Graff-Sargent, 10% phosphoric acid, etc. Samples were then observed on an Olympus metallograph capable of taking photographs. Some of samples were observed in a JEOL 35CF scanning electron microscope. Fracture surfaces were directly observed in the scanning electron microscope.

Thin foils for observation in a transmission electron microscope (TEM) were prepared by polishing and jet thinning. Samples for foils were cut from extruded stock and heat treated tensile bars using a very thin diamond wheel. The samples were mechanically ground on a 240 grit polishing paper until sufficiently thin. 3 mm discs were then punched out and jet thinned in a Fischione apparatus. The electrolyte used was a 75:25 mixture of methanol and concentrated nitric acid solution maintained at -50°C with an applied d.c. voltage of 40 volts. After jet thinning, the foils were observed in a 100 kV JEOL TEM as well as a Philips 120 KV STEM.

4.0 RESULTS

4.1 Mechanical Response

In order to determine the effect of manganese on the aging kinetics of 7075, a series of experiments were conducted, the results of which are shown graphically in Figures 25-27. Three samples were taken, solution treated at 465°C for 45 minutes and water quenched. One sample was left at room temperature and its hardness measured periodically (up to 64,000 minutes); the second was aged at room temperature for 24 hours and monitored while aging at 120°C. The third sample, after quenching, was aged at room temperature for 24 hours, and its hardness was measured after a series of 10-minute tempering treatments at 20°C temperature increments between 60 and 280°C. The graphs show that the aging process of 7075 is not severely altered by the addition of manganese, and therefore the alloy should achieve high strength through the aging process. The results of tensile tests conducted on manganese prealloy in various heat-treated conditions are shown in Tables XIV and XV. Higher tensile and yield strengths are obtained when these alloys are extruded at lower (e.g. 300°C) temperatures; ductilities, although limited, do not vary much with extrusion temperature. (Table XV)

The results of room temperature tensile testing for the silicon and chromium modified alloy in the T6 temper are given in Table XV and are depicted graphically in Figures 28-30. Contrary to what was observed for the manganese prealloy, the ultimate and yield strengths increase with increasing extrusion temperature up to 400°C but drop later at 450°C. The percent elongation in general increases with the extrusion temperature. It can be seen from Table XV that strengths decrease from manganese modified to manganese-silicon modified to manganese-chromium modified in that order while the elongations increase from Mn to Mn-Cr to Mn-Si modified alloys. The elastic moduli of the alloys are very similar in the T6 temper.

O temper properties of the modified alloys are also depicted in Figures 28-30. There is a less gradual variation in the properties with the extrusion temperature as compared to the T6 temper. In fact, the Mn-Cr modified alloy hardly shows any change in tensile strength and moderate

changes in yield strength and elongation. In contrast to the T6 condition, the Mn-Cr modified alloy exhibits better strengths than the Mn-Si modified alloys, however, the Mn-Si modified alloy has better elongations. The reasons for this phenomenon will be discussed later.

Figures 31 and 32 and Tables XVI and XVII show the room temperature comparisons of developmental alloys with 7075 and 2024, 7075 and 7090, respectively. Clearly, the developmental alloys have better properties except elongation. The Mn-Si modified alloy, for example, has 19% higher tensile strength, a 27% higher yield strength and a 14% higher elastic modulus in T6 temper. Compared to the established P/M alloy 7090, the Mn-Si modified alloy shows about 9% increase in tensile strength and 9.3% increase in yield strength in the T6 temper. The increases are more dramatic in the O temper. For example, over the P/M 7075, the Mn-Si alloy shows over 100% increase in tensile strength and over 200% increase in yield strength. Figures 33 and 34 show a comparison of specific properties. Even though the densities of modified alloys are higher than 7075, their specific properties are better due to high property levels. Thus, except for limited elongations, the modified alloys represent significant improvements in static mechanical properties over the existing 7XXX series alloys. It would therefore be interesting to compare their toughness properties.

The notched impact properties of the modified alloys are shown in Figure 35 and Table XIV. The impact properties of Mn-Si and Mn-Cr modified are better than Mn modified. This is because of better elongations in the former alloys. As compared to 7091, the modified alloys have about a third of impact strength. Tests on unnotched samples indicated that 7091 has higher crack initiation resistance than the Mn-Si and Mn-Cr modified alloys.

Figures 36-38 show the high temperature response of the alloys. As a comparison, data for 2024 and 7075 has been plotted along with the developmental alloys. Clearly, the developmental alloys retain higher strength up to about 200°C. This retention in strength is attributed to the presence of stable intermetallics present in the modified alloys.

Figures 39 and 40 show the various combinations of strength and ductility that have been obtained. These graphs show that a range of combinations can be obtained. The O temper obviously has a better ductility as compared to the T6 temper. Interestingly, the T73 temper results in a very good elongation, but the strengths are too low. Therefore, the

commercial T73 treatment may not be suitable for these alloys.

4.2 Microstructural Analysis

Optical metallography of the -325 mesh fraction of manganese modified alloy showed an extremely fine cast cellular microstructure as shown in Figure 41. Scanning electron microscopy revealed that the powders were characteristic of inert gas atomization: the oversize fraction being smooth and rounded (Figure 42) while the -325 mesh was smooth and rounded (Figure 43). It was also noted that the -325 mesh powder was of a bimodal distribution, the powder generally being above 25 μ m, or below 15 μ m diameter. Scanning electron microscopy of the silicon and chromium modified alloy powders revealed that the powders are spherical and have relatively smooth surfaces. This is typical of gas atomized powders. Some large particles have satellite particles attached to them as seen in Figures 44 and 45. When etched, the powders show a dendritic structure. In the extruded or heat treated condition, the alloys were difficult to etch, therefore, the grain structure could not be revealed optically. Typical microstructures, as seen optically, are shown in Figures 46 and 47.

Transmission electron microscopy was conducted on the alloys in heat treated as well as in as-received condition. Some typical microstructures in T6 temper are shown in Figures 48-53. There is no observable difference between the different extrusion temperatures. The micrographs in the as-received condition are depicted in Figures 54-57. Here again there are no discernible differences. A detailed discussion on the interpretation of these micrographs follows later on. X-ray analysis was done on the alloys in the as extruded, annealed and solutionized condition. The results are given in Table XVIII.

Fracture surfaces of tensile specimens were observed in the SEM and also optically. In most cases, the surfaces had an appearance typical of materials having limited ductility. At low magnification, no dimples can be seen; however, at high magnifications, dimpled fracture is evident. Some typical fracture surfaces are shown in Figures 58 and 59.

4.3 Corrosion Properties

The results of corrosion work are shown in Figures 60 and 61. The results in Figure 60 are for prealloyed manganese alloy. To judge its

performance, it was compared with I/M 7075. The results show that the manganese alloy has a poor corrosion response as compared to 7075. In Figure 61, a similar test was done for the silicon modified and chromium alloy. Here it was compared with 7091. The modified alloys have an inferior response as compared to 7091, especially chromium modified alloy. The initial corrosion rates in all the modified alloys are very high.

So far, we have presented the significant results of the study. In the next chapter, an attempt will be made to explain the mechanical behavior with the aid of microstructural analysis.

5.0 DISCUSSION

5.1 Phase identification

The various phases present in 7075 and modified alloys were determined using X-ray diffraction. In the I/M material, MgZn_2 and MgCuAl are major phases, although traces of $\text{Mg}_2\text{Zn}_{11}$ were observed. After annealing, the same phases were found to be present indicating that these are relatively stable if not equilibrium phases. On solutionizing, only traces of MgZn_2 and $\text{Mg}_2\text{Zn}_{11}$ were found.

In the case of prealloyed manganese alloy, in as-extruded condition, in addition to the age hardening phases, MnAl_6 is present. This is the primary intermetallic phase in this system and is formed during solidification. The same phases are present after annealing, and on solutionizing only MnAl_6 is present. The cubic $\text{Mn}_3\text{SiAl}_{12}$ is present as the primary intermetallic in the case of Mn-Si modified alloy along with MgZn_2 and $\text{Mg}_2\text{Zn}_{11}$ in extruded as well as annealed condition. On solutionizing, only $\text{Mn}_3\text{SiAl}_{12}$ is present indicating that the partitioning of manganese and silicon was as expected in this alloy. In the Cr modified alloy, the partitioning was not as expected. Instead of forming $(\text{Cr}, \text{Mn})\text{Al}_{12}$, the chromium reacted with magnesium to form $\text{Cr}_2\text{Mg}_3\text{Al}_{18}$. It has been reported in literature⁵⁴ that when % Cr is > % Mg, the above phase should be expected to form; however, it was anticipated that the non-equilibrium solidification conditions existing during rapid solidification might favor formation of $(\text{Cr}, \text{Mn})\text{Al}_{12}$. In addition, MnAl_6 and CrAl_7 were also found. On annealing, the same phases were present, and also in the annealed condition, MgZn_2 was observed only in traces in this alloy, although TEM analysis did show some presence of it. The impact of this change in intermetallic on the mechanical properties will be discussed later.

5.2 Microstructural Analysis

Since the optical metallography did not reveal much information about the microstructure, extensive transmission electron microscopy was done to characterize the microstructure. In this section, therefore, most of the discussion pertains to transmission electron microscopy. Recent

work^{55, 56} on rapid solidification of the binary Al-Mn system has shown that there are four phases present in these alloys. The MnAl_6 phase is generally seen as globular with no particular preference in growth direction in the aluminum matrix. This phase occurs either on subgrain boundaries or within subgrains depending on the composition and heat treatment. The G phase is semicoherent with the aluminum matrix and is therefore surrounded by misfit dislocations. The hexagonal G' phase is faulted parallel to the basal plane and the plane normal to the c direction. The T phase, which does not correspond to any previously reported phase, has the shape of an elongated plate and contains a complex faulted structure on planes perpendicular to its length. The T phase was observed to be metastable and disappeared on annealing at 450°C.

A systematic attempt to identify the phases present, viz., by electron diffraction or by the use of a STEM in the modified alloys was not made so that the identification is mainly based on visual comparison of our micrographs with those reported in the literature. Based on this, it appears that in the prealloyed manganese alloy, the main phase present is MnAl_6 . A lot of rod-like particles are present in this alloy, and there is a possibility that these particles belong to the T phase. Although the extrusions were subjected to solutionizing at 465°C for 45 minutes, this period may not be sufficient to dissolve the T phase completely. The primary intermetallics are of a diameter ranging from about 0.1 μm to about 0.5 μm , with the majority around 0.2 μm . The rod-like particles are coarser than the equiaxed ones. This may be due to the coarsening of the T phase during solutionizing. The distribution of particles is fairly homogeneous. MgZn_2 can be seen to have nucleated throughout the matrix, with some on the subgrain boundaries having nucleated heterogeneously.

The Mn-Si alloy has an intermetallic $\text{Mn}_3\text{SiAl}_{12}$ which is predominantly equiaxed. There is no specific orientation preference of these particles, and the particle distribution is homogeneous. The rod-like precipitates can be seen in this alloy, too, although their frequency is much less. The average particle diameter in this alloy is about 0.2 μm . Copious nucleation of MgZn_2 can be seen throughout the matrix accompanied by some on the subgrain boundaries.

The Mn-Cr modified alloy has different types of intermetallics, viz., $\text{Cr}_2\text{Mg}_3\text{Al}_{18}$, MnAl_6 , possibly CrAl_7 and perhaps T phase. Since the

different types have not been identified separately, it is not possible to comment on their relative abundance and morphology. The expected intermetallic $(\text{Cr}, \text{Mn})\text{Al}_{12}$ did not form in this alloy; therefore, some manganese-bearing particles have to be present, as it is difficult to expect all the manganese to be in solid solution. Thus, some of the equiaxed particles could be MnAl_6 . The rod-shaped particles are observed in this alloy, too, and these could be the T phase particles. The particles are about the same size as before, however the distribution appears to be relatively inhomogeneous. The volume fraction of intermetallics in this alloy seems to be higher than the Mn-Si modified, presumably because both Mn and Cr form intermetallics separately.

The age hardening phase, MgZn_2 , can be seen clearly in the alloy, although it was not detected during the X-ray analysis. The volume fraction appears to be smaller, and also the precipitates appear coarser. As before, the PFZs can be seen in this alloy; however, they are not limited only to the vicinity of the subgrain boundaries but can be seen around some larger particles. These particles must be Cr-bearing since chromium reacts with magnesium and therefore should leave a magnesium-depleted zone around it. So far, we have considered the morphology, size and distribution of the precipitates. We will now consider the grain and subgrain morphology.

When a metal is hot worked and cooled, one or more of the following four softening processes take place:⁵⁷

- (a) Static Recovery
- (b) Static Recrystallization
- (c) Dynamic Recovery
- (d) Dynamic Recrystallization

Softening occurring during cooling is referred to as static recovery and static recrystallization, while that occurring during the process of deformation itself is called dynamic recovery and dynamic recrystallization. In a commercial hot working operation in which the strain is low, as in rolling, the grains soften during deformation by dynamic recovery. In metals having high stacking fault energy such as aluminum, static recovery takes place during cooling; whereas in metals having low stacking fault energy such as copper, static recrystallization occurs readily. In an operation producing high strains such as extrusion, metals having high stacking fault energy undergo dynamic recovery followed by

static recovery and recrystallization. On the other hand, metals having low stacking fault energy undergo both dynamic recovery and recrystallization followed by static recovery and recrystallization.

Since dynamic recovery involves the occurrence of climb, cross-slip and node unpinning, it takes place readily in metals with high stacking fault energy. This leads to well-formed substructures in such metals. The metals having low stacking fault energies, on the other hand, have very tangled substructures. A certain critical strain is necessary before an alloy can undergo recrystallization, and therefore the latter metals undergo dynamic recrystallization. When dynamic recovery is taking place, the grains become elongated in the direction of flow; meanwhile, the substructure undergoes a process of polygonization, which keeps it dimensionally stable and equiaxed.

In situations where the particles are not cut by the dislocations and are relatively stable, they serve as obstacles which help initially to build up the substructure and finally to stabilize it. The presence of precipitates can prevent the formation of a subgrain structure altogether if the spacing is small enough, or if, as a result of their shearing, they induce the formation of matrix superdislocations, which cannot leave their slip planes. By preventing grain boundary migration, the particles can shift the initiation of dynamic recrystallization to higher strains and prevent it. If a concurrent precipitation is occurring, then the dislocation substructure assures a uniform distribution of precipitating particles.

Observation of the micrographs of the modified alloys indicates that the subgrains are about $0.5\mu\text{m}$ - $1.0\mu\text{m}$ in diameter and are elongated in the extrusion direction. There is a substantial grain boundary pinning by the precipitates in all the modified alloys (Figures 48-53). In the as-received condition, the dislocation substructure can be clearly seen (Figures 54 and 57). Thus it is reasonable to conclude that the modified alloys are dynamically recovered after hot extrusion. Comparing the micrographs in peak-aged condition to the as-extruded condition, there is no considerable difference in grain size or morphology. Solutionizing, therefore, does not coarsen the grain size. Also, the remnant dislocation substructure probably helped assure a homogeneous precipitation of MgZn_2 during aging.

There are no observable differences in microstructure between various extrusion temperatures. Thus, the following conclusions can be

drawn from the above discussion:

- (a) After hot extrusion, the alloys seem dynamically recovered with subgrains elongated in the extrusion direction. The average subgrain size is about 0.5-1.0 μ m.
- (b) There is no grain coarsening or static recrystallization during solutionizing.
- (c) Expected intermetallics are formed in Mn and Mn-Si modified, not in the Mn-Cr alloy. $MgZn_2$ is present in the former. Particle distribution is relatively inhomogeneous in the Mn-Cr alloy.
- (d) No observable difference in microstructure between various extrusion temperatures is noted.

Fracture surfaces of tensile specimens were observed in the SEM and also optically. In most cases, the surfaces had an appearance of brittle fracture. At low magnification, no dimples can be seen; however, at high magnifications, dimpled fracture is evident. The dimples are caused, in all probability, by the intermetallics present in the alloy. In some cases, the particles causing the dimples can be seen. An interesting feature of the fracture surface is the presence of holes in extrusions at lower temperatures. Examination of these holes at higher magnification reveals that there are particles sticking out. These could be the aluminides or oxide particles on the surface of each powder particle. Since the process of densification during extrusion consists of a constant breakup and rewelding of powder surfaces, the above observation could suggest a decohesion along the particle boundaries. Better particle bonding could therefore result at higher extrusion temperatures.

5.3 Mechanical Behavior

The results of tensile tests conducted on the manganese prealloy show that very good strengths are obtained in the high strength temper, although the ductilities are limited. The ductilities are low due to the presence of orthorhombic $MnAl_6$, which has fewer slip systems and thus will not deform with the matrix to accommodate the plastic strain. In the O temper, maximum ductility is obtained with concomitant lowest strength. In the intermediate tempers, there is a considerable drop in strength with only marginal gain in ductility. This is because the strength in the high

temper condition is controlled by MgZn_2 and not by the aluminides. The aluminides contribute to the strength over and above that obtained by the age hardened precipitate. The ductility on the other hand is controlled by the aluminides. Thus when the alloy is heat treated to T73 temper, the MgZn_2 loses its coherency due to coarsening and hence its strengthening effect. The aluminides, however, remain unchanged and therefore affect the ductility only marginally. Extruding the alloy at different temperatures causes a variation in strength of the alloy in the T6 temper. Highest strengths were obtained when extruded at 300°C and slightly lower at 400°C with strengths at 350°C being intermediate. The ductilities were quite similar. This is because of more softening taking place at 400°C than at 300°C by the process of dynamic recovery.

Contrary to what was observed for the manganese prealloy in the Mn-Si and in the Mn-Cr alloy to a lesser extent, the ultimate and yield strengths increase with increasing extrusion temperature from 300°C to 400°C but drop later at 450°C . The percent elongation in general increases with the extrusion temperature. These results are quite surprising, for it is expected that the strength would drop with higher extrusion temperature due to higher degree of dynamic recovery occurring at higher temperatures. The reasons for this behavior could be one or more of the following:

- (a) Different degree of recovery leading to a very small change in subgrain size.
- (b) Precipitation at higher extrusion temperatures.
- (c) Texturing of the alloys.
- (d) Particle bonding

Let us take each of these and consider briefly their contribution.

Dynamic recovery should lead to a softening at higher temperatures since the dislocation annihilation rate should be higher. Also, the processes of cross-slip, climb and node unpinning occur easily at higher temperature. However this process, viz., dynamic recovery combined with the process of precipitation, can lead to an increase in strength. In fact, mere higher precipitate densities could lead to higher strengths. Since it is difficult to visually differentiate between 10% and 12% volume fraction of precipitates, a subtle change in microstructure is not ruled out. As we shall see later, this change can cause an increase in strength by about 13%. Secondly, these precipitates can nucleate heterogeneously on the subgrain

boundaries, thereby stabilizing them. The resulting subgrain size could be finer. The contribution due to the latter factor, however, is not very significant, at least in the case of aluminum alloys.

Since the powders are prepared by RST, the solid solubilities of the solutes will be extended. Thus the powders will be supersaturated with manganese, chromium or silicon. Although it has been reported that the solid solution is stable up to 300°C, and that the solubility of manganese at higher temperatures does not change appreciably, a certain amount of precipitation will take place during degassing and further extrusion. Efforts are directed towards further quantifying these factors.

In the case of pure aluminum extruded at higher temperature and higher speeds, a duplex texture has been observed, viz., $\langle 111 \rangle$ and $\langle 001 \rangle$.⁵⁸ The $\langle 111 \rangle$ is a deformation texture, whereas the $\langle 001 \rangle$ has been associated with recrystallization. It was also observed that as the temperature increases, the amount of $\langle 001 \rangle$ component increases, presumably due to increased propensity for recrystallization.⁵⁹ Texture measurements were carried out on the silicon modified alloy, and resulting pole figures showed that all the round extrusions exhibited $\langle 111 \rangle$ texture. A $\langle 100 \rangle$ texture was also observed in these alloys. However, the exact amount of each component is not calculated yet, and further work on interpretation of the pole figures is currently underway.

As stated earlier, there was a subtle difference in the fracture surfaces between the lowest and highest extrusion temperatures which suggested that there could be a variation in particle bonding. Comparison between different extrusion temperatures of fracture surfaces in various heat-treated conditions should help clarify this aspect as the observation made in T6 temper should also be seen in other tempers as the heat treatments do not change the degree of particle bonding.

In summary, therefore, one or more of the above processes could account for increase in strength. It should be noted, however, that any appreciable increase in strength is usually associated with a drop in ductility. We find that percent elongations do increase with increasing strength. Thus in that respect, "particle bonding" hypothesis looks attractive as it can account for both phenomena.

Among the three modified alloys, prealloyed manganese alloy exhibited higher strengths and lowest elongations. Mn-Si and Mn-Cr had

lower strengths with the former having better properties. The prealloyed manganese alloy has a finer distribution of intermetallics as compared to the other two (Figures 48-53). As we shall see later, the major strengthening mechanism in these alloys is that due to Orowan, which predicts higher strengths with finer particle sizes. The elongations on the other hand are lower because of the coarse rod-like particles. There is no conclusive evidence for this hypothesis in these alloys; however, coarse particles are known to severely reduce ductilities in metals.

The Mn-Cr modified alloy has lower strengths as compared to the Mn-Si in the T6 temper due to a coarser and reduced volume fraction of $MgZn_2$. However this results in an increased volume fraction of aluminides in this alloy and therefore in the O temper, Cr-modified alloy has higher strength. $MgZn_2$ coarsens when the alloy is heat treated to O temper. Since the strength is controlled by $MgZn_2$, coarsening of that phase leads to a drop in strength. Ardell⁶⁰ has shown that as the volume fraction of precipitates increases, the coarsening rates also increase, leading to a broad particle size distribution. Thus the Mn-Si alloy has lower strengths in the O temper. A brief comment about the reduced strength of the plate extrusion: It was observed that the texture in plate was quite different than that in the round bars. The reasons for this could be that the extrusion ratio for plate was 32:1 as compared to 16:1 for a rod. Also, a plain strain component of texture may be present in the plate extrusion since it is extruded from a cylindrical can. It is not quite clear yet if this explains the strength variation satisfactorily. After having considered the individual alloy systems, we will now attempt to explain the strength increases achieved in the modified alloys over a typical alloy such as 7075.

Yield stress of particle-hardened alloys has been the subject of numerous reviews over the past two decades.⁶¹⁻⁶³ Kelly and Nicholson⁶¹ have distinguished between two types of dislocation-particle interactions: One in which the particles are sheared and the other in which the dislocations bow around the particles.

The latter mechanism has been a subject of numerous studies, notably in the 60's and 70's, and has been very clearly established as a major strengthening mechanism in dispersion-hardened alloys. The former mechanism is rather difficult to analyze since the particle shearing could occur by one or more process.

Following are the possible sources for the shearing force.^{64, 65}

(i) Coherency hardening arising from the elastic coherency stresses surrounding a particle that does not fit the matrix exactly. The increase in yield stress is proportional to $r^{1/2}$ and $f^{1/2}$.

(ii) Surface or chemical hardening arises from the energy required to create an additional particle/matrix interface when the particle is sheared by the dislocation. In this case, the increase in yield stress is proportional to r^{-1} and $f^{1/2}$.

(iii) Order hardening is due to the additional work required to create an antiphase boundary in the case of dislocations passing through precipitates which have an ordered lattice. The increase in yield stress is proportional to $(fr)^{1/2}$.

(iv) Stacking fault hardening occurs when there is a difference between the stacking fault energy of the particle and that of the matrix when these are either both face-centered cubic (fcc) or both hexagonal close-packed (hcp) in structure. An increase in yield strength is proportional to $(fr)^{1/2}$.

(v) Modulus hardening arises from differences between the elastic moduli of matrix and particle. The predicted increase in yield strength is again proportional to $(fr)^{1/2}$.

Since a lot of mechanisms predict a $(fr)^{1/2}$ dependence of yield stress, isolating the contribution due to individual mechanism is very difficult. There is a considerable lack of experimental data to test these theories, and the task is hindered due to insufficiency of systems which harden by a single mechanism.

Although a considerable amount of work has been done in characterizing the Al-Zn-Mg system, there have been very few attempts to correlate the strengths with the microstructure. Recently, ⁶⁶⁻⁶⁸ some attempts have been made to explain the mechanical properties of these alloys based on their structure. We will not describe in detail the models developed in these studies, but shall briefly review their conclusions.

Of the five shearable type mechanisms, two are clearly ruled out, viz., order hardening and stacking fault hardening, since the $MgZn_2$ is not internally ordered and does not have fcc crystal structure. Of the remaining three, coherency hardening is not considered a major mechanism. We are not sure why this mechanism has not been a part of strengthening mechanisms,

and further work is being done to clarify the matter. Melander and Person⁶⁶ in their study have shown that the yield strength of the alloy is controlled by the screw dislocations in the under and overaged condition. They interpreted their experimental results on the basis of shear modulus hardening of GP zones. The incoherent MgZn_2 particles are overcome by Orowan mechanism.

The other study conducted by Kovacs, et.al.^{67, 68} explained their results on the basis of surface hardening mechanism for GP zones and Orowan mechanism for the MgZn_2 particles. The equation developed by them predicts a $(fr)^{1/2}$ type of dependence for the yield stress, which is different from the Kelly and Nicholson model (see equation [4] in ref. 65). We are currently working on resolving this issue.

Thus, the major mechanisms contributing towards the strength of precipitation hardened Al-Zn-Mg alloy are modulus, surface hardening for the GP zones and Orowan mechanism for the incoherent MgZn_2 precipitate.

When an aluminide dispersion was introduced in these alloys, it was anticipated that the dislocations would bow out between the stiff intermetallic particles. This is the classical Orowan mechanism for dispersion strengthening. The original equation, later modified by Kocks⁶⁹ and Ashby^{70, 71}, is given as:

$$\tau = \frac{0.81 G b \ln(2r_s/r_0)}{2\pi(1-\nu)^{1/2} (\lambda_s - 2r_s)}$$

where τ = increase in critical resolved shear stress of matrix
 G = shear modulus of matrix
 b = Burger's vector of the dislocations
 $r_s = \sqrt{2/3} r$, r = particle radius
 λ_s = average center-to-center spacing
 r_0 = inner cut-off radius for the dislocation core (usually r_0 is approximated by b)

Not directly apparent is the effect of volume fraction, but it comes when substitution for λ_s is made. A theoretical plot of this equation is shown in Figure 62 for different volume fractions. It can be clearly seen that particle size has a more pronounced effect on the yield

stress than the volume fraction, especially at smaller particle sizes.

Based on this equation, it was attempted to predict the increase in strength over a 7075 matrix. The numbers are not in exact agreement but are close to the predicted values. In T6 temper, therefore, one can explain the increase in strength in the modified alloys. The increases are more dramatic in the O temper, and the Orowan mechanism alone cannot account for it. Some other factors could be adding to the strength such as texture, fine grain size, etc. A detailed analysis will be done to explain the properties.

To evaluate the high temperature response of these modified alloys, they were compared with 2024 and 7075. Clearly, the developmental alloys retain higher strength up to about 200°C. This retention in strength is attributed to the presence of stable intermetallics present in the developmental alloys. 7075 shows a rapid drop in strength since the precipitate from which it derives its strength, viz., $MgZn_2$, coarsens at around 200°C. In comparison, 2024 derives its strength from $CuAl_2$ which is more stable. The coarsening rates of intermetallics in the developmental alloys are low because of two factors. First, the diffusion rates of transition elements in aluminum are very low, and second, their solid solubility at higher temperature does not change appreciably. Therefore, even though the diffusion distances are smaller in P/M alloys due to the finer microstructure, these modified alloys are still able to retain their strength at elevated temperatures.

As compared to 7091 in both the T6 and T73 tempers, the impact properties of developmental alloys are slightly inferior. A comparison of notched vs. unnotched data indicated that 7091 has higher resistance to crack initiation than the developmental alloys. It is anticipated that the crack propagation rates would be of the same order in both. In general, crack propagation rates in P/M alloys are higher compared to their I/M counterparts because in P/M alloys, it is easier for the cracks to propagate due to smaller grains. The lower impact strength of developmental alloys as compared to 7091 is attributed to the presence of higher volume fraction of dispersoid phase in the former. These particles are brittle in nature and thus have lower crack initiation resistance.

5.4 Corrosion Evaluation

The results of weight loss test showed manganese alloy has a poor corrosion response as compared to 7075. A similar test was done for the silicon and chromium modified alloy, when compared with 7091, showed that the modified alloys have an inferior response, especially the chromium modified alloy. The initial corrosion rates in all of the modified alloys are very high. This is probably due to the presence of fine intermetallics. Since these intermetallics are incoherent, the interphase between these intermetallics and the matrix has a high energy associated with it. These regions are most likely to be attacked first by a corrosive medium. Also, since the volume fraction of these particles is large and they are finer in size, the total surface area of this interphase is large. This could possibly explain higher corrosion rates in these alloys. Some SCC testing was done but was met with limited success. All of the samples failed in one day because the samples inadvertently got loaded beyond their yield point. Therefore, no conclusion could be derived about their propensity for SCC.

6.0 CONCLUSIONS

(1) Modification of 7075 base alloy through additions of manganese, chromium and silicon results in increased strength and modulus with limited elongations.

(2) For the prealloyed manganese alloy, highest strengths were achieved in extrusions at 300°C, while for the Mn-Si and Mn-Cr modified alloys, highest strengths were achieved at 400°C. Better elongations were achieved when extruded at 450°C in the latter alloys.

(3) Up to 200°C, strength retention is better for modified alloys as compared to 7075 or 2024. This is attributed to the presence of fine intermetallics.

(4) Both Mn-Si and Mn-Cr alloys exhibit similar levels of toughness in T6 and T73 tempers. The impact energy is about a third of 7091 for the notched samples.

(5) Partitioning of manganese is as expected in the Mn and Mn-Si modified alloy, the resulting intermetallics being MnAl_6 and $\text{Mn}_3\text{SiAl}_{12}$, respectively. In the chromium modified alloy, the intermetallic formed is $\text{Cr}_2\text{Mg}_3\text{Al}_{18}$.

(6) Age hardening precipitates are present in Mn and Mn-Si modified alloys, whereas in the Mn-Cr modified alloy, the volume fraction is reduced.

(7) After hot extrusion, the alloys are dynamically recovered, leaving elongated subgrains. The average particle size is about 0.2 μm -0.5 μm . The particle distribution is homogeneous in Mn and Mn-Si alloys.

(8) The high strength of the alloys is still controlled by the MgZn_2 dispersion. Aluminides contribute above that limit. On the lower end, the strength is controlled by the aluminide dispersion.

(9) Corrosion resistance of prealloyed manganese alloy is inferior to 7075 and that of modified alloys inferior to 7091. Silicon modified alloy, however, has a better corrosion response.

(10) Overall, the Mn-Si modified alloy is superior than the Mn or the Mn-Cr alloys.

REFERENCES

1. B. H. LeCerf and A. M. Greene, "Advanced materials given room to fly in aerospace," Iron Age, Vol. 221, No.25, June 19, (1978), p. 53.
2. D. J. Holt, "Aluminum: the next decade," Aerospace Engg., Vol. 4, No. 5, Sept/Oct (1984), p. 62.
3. A. W. Demmler, "Aluminum and titanium compared," Aerospace Engg., Vol. 5, No. 3, (1985), p. 33.
4. High Strength Powder Metallurgy of Aluminum Alloys, Eds. M. J. Koczak and G. J. Hildeman, The Metallurgical Society of AIME, Warrendale, Pa, (1982).
5. J. R. Pickens, "Aluminum powder metallurgy technology for high strength applications," J. of Mat. Sci., Vol.16, (1981), p.1437.
6. Physical Metallurgy by Peter Haasen, Cambridge University Press, Cambridge, U. K., (1978).
7. J. P. Lyle and W. S. Cebulak, "Properties of high strength aluminum P/M products," Metals Engg. Quarterly, Vol. 14, No. 1, (1974), p. 52.
8. J. P. Lyle and W. S. Cebulak, "Powder metallurgy approach for control of microstructure and properties in high strength aluminum alloys," Met. Trans. A, Vol. 6A, (1975) p. 685.
9. W. S. Cebulak, E. W. Johnson and H. Markus, "High strength aluminum P/M products," Metals Engg. Quarterly, Vol. 16, No. 4, (1976), p. 37.
10. W. S. Cebulak, E. W. Johnson and H. Markus, "High strength P/M mill

products," *Int. J. of P/M and Pow. Tech.*, Vol. 12, No. 4, (1976), p. 299.

11. W. S. Cebulak, "Processing/Property Interactions in High Strength P/M Mill Products," in Rapid Solidification Processing: Principles and Technologies, R. Mehrabian, B. H. Kear and M. Cohen, Eds., Vol. 2, Claitor's Publishing Div., Baton Rouge, La. (1980), p. 324.
12. M. Rafalin, A. Lawley and M. J. Koczak, "Fatigue of high strength of powder metallurgy aluminum alloys," in ref. 4, p. 63.
13. M. J. Koczak and M. J. Topolski, "Development of duplex Al-Zn-Mg/Al-Mn high modulus P/M aluminum alloys," in ref. 4, p. 297.
14. V. W. C. Kuo and E. A. Starke, Jr., "The effect of ITMT's and P/M processing on the microstructure and mechanical properties of the X7091 alloy," in ref. 4, p. 41.
15. T. H. Sanders, "Factors influencing toughness and other properties of aluminum-lithium alloys," NADC contract #N62269-76C-0271, June 14, (1979).
16. R. E. Sanders, Jr., G. J. Hildeman and D. J. Lege, "Elevated temperature alloy development," AFML contract #F33615-77-C-5086, March 31, (1979).
17. Rapid Solidification Processing. Principles and Technologies, Vol. 1 Eds. R. Mehrabian, B. H. Kear and M. Cohen, Claitor's Publishing Div., Baton Rouge, LA, (1977).
18. Rapid Solidification Processing. Principles and Technologies, Vol. 2, Eds. R. Mehrabian, B. H. Kear and M. Cohen, Claitor's Publishing Div., Baton Rouge, LA, (1980).
19. Rapidly Quenched Metals III, B. Cantor, Ed., The Metals Society, London, UK, (1978).

20. Recrystallization and Grain Growth in Metals, P. Cotterill and P. Mould, Ed., Surrey University Press, London, (1976).
21. N. Dudzinski, J. R. Murray, B. W. Mott and B. Chalmers, "The moduli of aluminum alloys in tension and compression," J. Inst. of Metals, Vol. 74, (1948), p. 291.
22. N. Dudzinski, "The Young's modulus, Poisson's ratio and rigidity modulus of some aluminum alloys," J. Inst. of Metals, Vol. 81, (1952-1953), p. 49.
23. E. Kovacs-Csetenyi, "The effect of small amounts of addition elements on the Young's modulus of high purity aluminum," Aluminum, Vol. 52, (1976), p. 669.
24. Low density aluminum alloy development (First interim technical report), Contract # F33615- 81-C-5053, The Boeing Company, Seattle, Wa. June (1982).
25. M. O. Speidel, "Stress corrosion cracking of aluminum alloys," Met. Trans. A, Vol. 6A, (1975), p. 631.
26. D. S. Thompson, "Metallurgical factors affecting high strength aluminum alloy production," Met. Trans. A, Vol. 6A, (1975), p. 671.
27. G. Ludtka and D. E. Laughlin, "The effect of solute content on the slip behaviour in 7XXX series aluminum alloys," Met. Trans. A, Vol. 12A, (1983), p. 2083.
28. R. J. H. Wanhill, "Aluminum alloys for advanced structural applications," Aluminum, Vol. 54, (1978), p. 455.
29. E. A. Starke, Jr., "Aluminum alloys of the 70's : Scientific solutions to engineering problems," Mat. Sci. and Engg., Vol. 29, (1977), p. 99.

30. G. T. Hahn and A. R. Rosenfeld, "Metallurgical factors affecting fracture toughness of aluminum alloys," *Met. Trans. A*, Vol. 6A, (1975), p. 653.
31. C. G. Garrett and J. F. Knott, "The influence of compositional and microstructural variations on the mechanism of static fracture in aluminum alloys," *Met. Trans. A*, Vol. 9A, (1978), p. 1187.
32. J. S. Santner, "A study of fracture in high purity 7075 aluminum alloys," *Met. Trans. A*, Vol. 9A, (1978), p. 769.
33. J. S. Santner and D. Eylon, "Fatigue behaviour and failure mechanisms of modified 7075 aluminum alloys," *Met. Trans. A*, Vol. 10A, (1979), p. 841.
34. N. Ryum, "The influence of precipitate free zones on the mechanical properties of an Al-Zn-Mg alloy," *Acta Met.*, Vol. 16, No. 3, (1968), p. 327.
35. E. Hornbogen and K. H. Zuhm Gahr, "Distribution of plastic strain in alloys containing small particles," *Metallography*, Vol. 8, (1975), p. 181.
36. E. Hornbogen and K. H. Zuhm Gahr, "Microstructure and fatigue crack growth in a γ -Fe-Ni-Al alloy," *Acta Met.*, Vol. 24, No. 6, (1976), p. 581.
37. V. W. C. Kuo and E. A. Starke, Jr., "The effect of ITMT's and P/M processing on the microstructure and mechanical properties on the X7091 alloy," *Met. Trans. A*, Vol. 14A, (1983), p. 435.
38. E. A. Starke and G. Lutjering in Fatigue and Microstructure, American Society for Metals, Metals Park, OH, (1978), p. 205.
39. A. Joshi, C. R. Shastri and M. Levy, "Effect of heat treatment on solute

concentration at grain boundaries in 7075 aluminum alloy," Met. Trans., Vol. 12A, (1981), p. 1081.

40. J. Albrecht, I. M. Bernstein and A. W. Thompson, "Evidence for dislocation transport of hydrogen in aluminum," Met. Trans. A, Vol. 13A, (1982), p. 811.
41. M. J. Koczak, NADC Report # 80100-60
42. R. E. Lewis et al, "Development of advanced aluminum alloys from rapidly solidified powders for aerospace structural applications," Interim technical reports on Defense Advanced Research Projects Agency Contract, F33615-78-C-5203, Order # 3575.
 - (a) LMSC-D674504 (March 1979)
 - (b) LMSC-D678772 (September 1979)
 - (c) LMSC-D686125 (March 1980)
 - (d) LMSC-D777825 (September 1980)
 - (e) LMSC-D802523 (January 1981)
 - (f) LMSC-D832356 (September 1981)
43. H. G. Paris, J. W. Mullins and T. H. Sanders, "The effect of solidification microstructures in the strength ductility and toughness of dispersion-hardened P/M alloys," in ref. 4, p. 277.
44. R. E. Sanders and G. J. Hildeman, "Elevated temperature aluminum alloy development," Final Technical Report on Air Force Material Laboratory Contract F33615-77-C-5086, Report AFWAL-TR-81-4076, May 1981.
45. G. V. Raynor and K. Little, "The Constitution of Aluminum Rich Alloys of Aluminum, Chromium and Manganese," J. of Inst. of Metals, Vol. 71, (1945), p. 429.
46. J. W. Clare, "The Constitution of Aluminum Rich Alloys of the Aluminum - Chromium - Manganese System," Trans. of the Met. Soc. of AIME, Vol. 215, (1959), p. 429.

47. W. Rostoker, R. P. Dudek, C. Freda and R. E. Russell, "Fast Freezing by Atomization for Aluminum Alloy Development," Int. J. of Powder Met., Vol. 4, (1973), p.139.
48. C. E. Freda, "The Properties of Aluminum - Manganese Polycomponent Powder Alloys," M. S. Thesis, (1975), University of Illinois.
49. Aluminum Alloys, Structure and Properties by L. E. Mondolfo, Butterworths, London, UK, (1979)
50. L. A. Jacobson and M. M. Cook, "Microstructures of powder and conventionally processed 7075 aluminum alloy," Air Force Materials Laboratory Report AFML-TR-71-240.
51. Aluminum Volume 1 : Properties Physical Metallurgy and Phase Diagrams, Ed. K. R. Van Horn, American Society for Metals, Metals Park, OH, (1967).
52. P. L. Morris and B. J. Duggan, "Precipitation and Recrystallization in an Al - 1.8% Mn alloy," Met. Sci. J, Vol. 12, No. 1, (1978) p. 1.
53. J. DeLuccia, NADC, Warminster Pa., private communication (1983).
54. L. F. Mondolfo, "Structure of the aluminium : magnesium : zinc alloys," Metallurgical Review, Vol. 16 (1971) p. 95.
55. R. J. Schaefer, D. Shechtman, and F. S. Biancaniello, "Rapid Solidification Microstructures and Precipitation in Al-Mn Alloys" in Rapidly Solidified Metastable Materials, Eds. B. H. Kear and B. C. Giessen MRS Symposia Proceedings, Vol. 28 (1984) Elsevier Science Publishers, NY, pp. 323-327.
56. D. Shechtman, R. J. Schaefer and F. S. Biancaniello, "Precipitation in Rapidly Solidified Al-Mn Alloys," Met. Trans. A, Vol. 15A (1984), pp. 1987-1997.

57. H. J. McQueen and J. J. Jonas, "Recovery and Recrystallization in hot worked materials" in Treatise on Materials Science and Technology Ed. R. J. Arsenault, Vol. 6 (1975) Acad. Press, NY, pp. 393-493.
58. C. J. McHargue, L. K. Jetter and J. C. Ogle, "Preferred orientation in extruded aluminum rod," Trans. of Met. Soc. of AIME, Vol. 215 (1959), p. 831.
59. R. A. Vandernieer and C. J. McHargue, "The nature of the $\langle 001 \rangle$ fibre-texture component in extruded aluminum rods," Trans. of Met. Soc. of AIME, Vol. 230 (1964), p. 667.
60. A. J. Ardell, "The effect of volume fraction on particle coarsening : theoretical considerations," Acta Met., Vol. 20, No. 1 (1972), p. 61.
61. A. Kelly and R. B. Nicholson, "Precipitation Hardening," Prog. in Materials Science, Ed. B. Chalmers, Vol. 10 (1961) Pergamon Press, NY, pp. 1439-391.
62. G. S. Ansell, "The Mechanism of Dispersion Strengthening : A Review" in Oxide Dispersion Strengthening, Eds. G. S. Ansell, T. D. Cooper and F. V. Lenel, Proc. of the Second Bolton Landing Conf., Bolton Landing, June 1966, Gordon and Breach, Science Publishers (1968), pp. 61-141.
63. L. M. Brown and R. K. Ham, "Dislocation-Particle interactions" in Strengthening Methods in Crystals, Eds. A. Kelly and R. B. Nicholson (1971), Elsevier, Amsterdam, pp. 9-131.
64. J. W. Martin, "Micromechanisms in particle-hardened alloys," Cambridge University Press, Cambridge, UK, (1980).
65. P. M. Kelly, "The Quantitative Relationship between Microstructure and Properties in Two-Phase Alloys," Int. Met. Reviews, Vol. 18 (1973), pp. 31-36.

66. A. Melander and Per Ake Persson, "The Strength of a Precipitation Hardened AlZnMg Alloy," *Acta Met.*, Vol. 26 (1978), pp. 267-278.
67. I. Kovacs, J. Lendvai, T. Ungar, T. Turmezey and G. Broma, "The Properties of an AlZnMg Alloy Deformation Strengthened by Guinier-Preston Zones," *Acta Met.*, Vol. 25 (1977), pp. 673-680.
68. I. Kovacs, J. Lendvai, T. Unger, G. Groma and J. Lakner, "Mechanical Properties of AlZnMg Alloys," *Acta Met.*, Vol. 28 (1980), pp. 1621-1631.
69. U. F. Kocks, *Phil. Mag.*, Vol. 14 (1966), p. 1629.
70. M. F. Ashby in ref. 62, pp. 143-205.
71. M. F. Ashby, "On the Orowan Stress," in Physics of Strength and Plasticity, Ed. Ali S. Argon, Publisher MIT Press, Cambridge, MA, USA (1969), pp. 113-131.

TABLES

TABLE I
Mechanical Property Data for Powder Blended Duplex Alloys in T6 Temper

Alloy + Processing	E Elastic Modulus GPa (10 ⁶ Psi)	σ_{UTS} Ultimate Strength MPa (ksi)		% RA Reduction in Area %	Full Size Charpy Impact Strength J (ft-lb)		Subsize Charpy Impact Strength J (ft-lb)	
		MPa	(ksi)		J	(ft-lb)	J	(ft-lb)
7075								
2:1 forge	---	---	---	---	---	---	---	---
7:1 forge	66.2 (9.60)	586	(85.0)	36.5	6.1	(4.5)	---	---
7:1 forge + coarsen	---	587	(85.2)	34.4	5.4	(4.0)	---	---
20:1 extrusion	65.8 (9.55)	678	(98.3)	18.7	---	---	---	---
7075 + 10 %/o (Al-17 %/o Mn)								
2:1 forge	65.6 (9.52)	---	---	<1	2.0	(1.5)	---	---
7:1 forge	74.0 (10.74)	514	(74.5)	2.1	4.1	(3.0)	---	---
7:1 forge + coarsen	---	495	(71.8)	2.4	2.0	(1.5)	---	---
20:1 extrusion	---	---	---	---	---	---	---	---
7075 + 20 %/o (Al-17 %/o Mn)								
2:1 forge	69.3 (10.05)	414	(60.0)	<1	2.3	(1.7)	---	---
7:1 forge	72.9 (10.58)	475	(68.9)	<1	2.7	(2.0)	---	---
7:1 forge + coarsen	---	467	(67.7)	<1	2.0	(1.5)	---	---
20:1 extrusion	80.0 (11.60)	496	(72.0)	<1	---	---	1.0	(0.86)
7075 + 40 %/o (Al-17 %/o Mn)								
2:1 forge	86.1 (12.49)	310	(45.0)	<1	2.0	(1.5)	---	---
7:1 forge	76.9 (11.16)	468	(67.9)	<1	1.4	(1.0)	---	---
7:1 forge + coarsen	---	420	(61.0)	<1	1.4	(1.0)	---	---
20:1 extrusion	---	---	---	---	---	---	---	---
X7091								
20:1 extrusion	60.8 (8.82)	627	(90.9)	30.6	---	---	---	---
X7091 + 20 %/o (Al-17 %/o Mn)								
20:1 extrusion	75.0 (10.88)	503	(73.0)	<1	---	---	---	---

TABLE II
Tensile Test Data for Powder Blended Duplex Alloys* in the 0 Temper and T6 Condition

Alloy	Temper	E Elastic Modulus GPa (10 ⁶ Psi)	σ_{YS} Yield Strength MPa (ksi)	σ_{UTS} Ultimate Strength MPa (ksi)	% EL Elongation	Subsize Charpy Impact Strength J (ft-lb)
7075	0	70.3 (10.2)	144 (20.9)	299 (43.2)	18.4	8.0 (6.26)
	T6	72.4 (10.5)	600 (87.0)	654 (94.8)	10.4	3.3 (2.50)
7075 + 20 %o (Al-17 %o Mn)	0	77.2 (11.2)	154 (22.4)	239 (34.7)	5.3	2.5 (1.96)
	T6	80.7 (11.7)	471 (68.3)	487 (70.7)	≤ 1	1.3 (1.01)
X7091	0	70.3 (10.2)	140 (20.3)	290 (42.1)	21.4	--
	T6	71.0 (10.3)	571 (82.8)	596 (86.5)	13.5	--
X7091 + 20 %o (Al-17 %o Mn)	0	----	165 (24.0)	240 (34.8)	6.6	--
	T6	79.3 (11.5)	496 (71.9)	496 (71.9)	≤ 1	--

*Direct powder extrusions 20:1

TABLE III
SUMMARY OF PROCESSING PARAMETER/PROPERTY RELATIONS

Duplex Alloy Addition Parameter		Modulus	Strength	Ductility	Hardness
Powder Size	Size	--	➡	➡	--
Volume Fraction	V_f	➡	➡	➡	➡
Manganese Content	Z_{Mn}	➡	➡/➡	➡	➡
Degree of Deformation	Z_D	--	➡	➡	--

➡ Property Improvement

➡ Property Degradation

➡/➡ Dependent on Interplay of S , V_f , Z_{Mn} , Z_D

-- No Change

TABLE IV
Chemical Compositions of Powders for Duplex Alloys

Alloy	(weight percent)								
	Si	Fe	Cu	Mn	Mg	Cr	Zn	Co	Ti
7075	0.40	0.50	1.2 - 2.0	0.30	2.1 - 2.9	0.18 - 0.28	5.1 - 6.1	--	0.20
Al-Mn	--	--	--	17.0	--	--	--	--	--

Balance Aluminum

TABLE V
Extrusion Parameters for Air Atomized Powder Blended Duplex Alloys

Can:	6061, 2.0 inch O.D. x 1.870 inch I.D.				
Compaction:	Uniaxial 65 tons				
Degassing:	330°C until vacuum stabilized				
Preheat Temperature:	400°C				
Preheat Time:	1.75 hours				
Extrusion Temp:	400°C				
Die Size:	0.460 inch				
		Extrusion Speed	Upset Load	Running Load	Reduction
Alloy					
7075 + 20 % (Al-17 % Mn) [75-53µm]		25 i.p.m.	200 tons	180 tons	20:1
7075 + 40 % (Al-17 % Mn) [75-53µm]		25 i.p.m.	200 tons	180 tons	20:1
7075 + 20 % (Al-17 % Mn) [<53µm]		25 i.p.m.	200 tons	180 tons	20:1

TABLE VI
Mechanical Property Data for Sleved and Blended Duplex Alloys

		E	σ_{YS}	σ_{UTS}	% EL	Subsize Charpy	
		Elastic Modulus GPa (10 ⁶ Psi)	Yield Strength MPa (ksi)	Ultimate Strength MPa (ksi)	Elongation	Impact Strength J (ft-lb)	
7075 + 20 %o (Al-17 %o Mn)	[75-53µm]	T6	77.9 (11.3)	484 (70.2)	495 (71.8)	1.0	0.73 (0.56)
		0	73.1 (10.6)	167 (24.2)	253 (36.7)	5.0	1.72 (1.32)
		T76	86.9 (12.6)	439 (63.7)	461 (67.0)	1.1	--
7075 + 40 %o (Al-17 %o Mn)	[75-53µm]	T6	86.2 (12.5)	----	----	--	0.35 (0.27)
		0	91.0 (13.2)	204 (28.6)	277 (40.2)	0.9	0.49 (0.38)
		T76	83.4 (12.1)	----	395 (57.3)	--	--
7075 + 20 %o (Al-17 %o Mn)	[<53µm]	T6	79.2 (11.5)	512 (74.2)	525 (76.2)	1.4	0.52 (0.40)
		0	82.7 (12.0)	170 (24.6)	272 (39.5)	7.9	1.46 (1.12)
		T76	81.4 (11.8)	459 (66.6)	463 (67.2)	1.3	--

TABLE VII

Wear Test Results

Apparatus:	LFM-1 Friction and Wear Tester (Located at NADC, Warminster, PA)						
Test Ring:	SAE 4620 Steel, Rc 58-63, Diameter 35.0mm, Surface Finish 5-15 Micro inch						
Speed:	72 rpm, 131.9 mm/sec.						
Load:	40.91 Kg						
Distance Traveled:	10,000 revolutions, 1,099,200 mm.						
Temperature:	Room Temperature						
Alloy	Hardness P(Kg/mm ²)	Wt. Loss (mg) After 10,000 Cycles	Volume of Wear V(mm ³)	Wear Coefficient (K)	Friction Coefficient (μ)		
P/M 7075	207	16.5	5.89	8.1×10^{-5}	0.56		
7075 + 20 % (Al-17 % Mn) [Unsieved]	207	22.6	8.18	11.3×10^{-5}	0.44		
7075 + 40 % (Al-17 % Mn) [75-53μm]	183	27.0	9.64	11.8×10^{-5}	0.39		
7075 + 20 % (Al-17 % Mn) [<53μm]	207	22.8	8.14	11.3×10^{-5}	0.44		
7075 + 20 % (Al-17 % Mn) [<45μm]	217	23.6	8.43	12.2×10^{-5}	0.41		
7075 + 40 % (Al-17 % Mn) [<45μm]	235	32.0	11.43	17.9×10^{-5}	0.44		
7075 + 36 % Mn (Prealloyed)	240	23.4	8.36	13.4×10^{-5}	0.44		

TABLE VIII

Chemical Analysis of Helium Atomized Al-17 w/o Mn Powder (-325 mesh)

(weight percent)

Alloy	Al	Mn	Fe	Zn	-325 mesh traction
Al-17 ^{w/o} Mn (-325 mesh)	81.3	17.32	0.14	1.22	93.1

TABLE IX
Extrusion Parameters for Helium Atomized Powder Blended Duplex Alloys

Can:	6061, 2.0 inch O.D. x 1.870 inch I.D.				
Compaction:	Uniaxial 65 tons				
Degassing:	330°C until vacuum stabilized				
Preheat Temperature:	390°C				
Preheat Time:	2.5 hours				
Extrusion Temp:	390°C				
Die Size:	0.460 inch				
		Extrusion Speed	Upset Load	Running Load	Reduction
7075 + 20 % (Al-17 % Mn) [$<45\mu\text{m}$]		25 i.p.m.	150 tons	145 tons	20:1
7075 + 20 % (Al-17 % Mn) [$<45\mu\text{m}$]		25 i.p.m.	155 tons	150 tons	20:1
7075 + 40 % (Al-17 % Mn) [$<45\mu\text{m}$]		25 i.p.m.	200 tons	180 tons	20:1

TABLE X
Mechanical Property Data for Helium Atomized Blended Duplex Alloys

		E Elastic Modulus GPa (10 ³ Psi)	σ_{YS} Yield Strength MPa (ksi)	σ_{UTS} Ultimate Strength MPa (ksi)	% EL Elongation	Subsize Charpy Impact Strength J (ft-lb)
7075 + 20 % (Al-17 % Mn) [$<45\mu\text{m}$]	T6	77.2 (11.2)	----	536 (77.7)	0.6	0.38 (0.29)
	0	75.1 (10.9)	210 (30.6)	303 (43.9)	5.6	1.14 (0.88)
7075 + 40 % (Al-17 % Mn) [$<45\mu\text{m}$]	T6	85.6 (12.42)	----	516 (74.8)	0.2	----

TABLE XI
 Chemical Analysis of Helium Atomized Mn, Mn-Si, Mn-Cr Modified 7075 Powders

(weight percent)

Alloy	Zn	Mg	Cu	Mn	Cr	Si	Fe	Al	Ag
7075 + Mn	6.48	2.77	1.95	3.87	0.21	--	0.16	Bal	--
7075 + Mn-Si	7.84	1.92	2.08	3.73	--	1.05	0.05	Bal	--
7075 + Mn-Cr	6.35	2.80	2.19	1.79	1.53	<0.10	0.10	Bal	0.29

TABLE XIISieve Analysis of Mn, Mn-Si and Mn-Cr Modified Alloy Powders

Alloy	Mesh Size	Weight Percent
7075 + Mn	+325	6.5
	-325	93.5
7075 + Mn-Si	+400	5.7
	-400	94.3
7075 + Mn-Cr	+400	9.8
	-400	90.2

TABLE XIII
Extrusion Parameters for Helium Atomized Prealloyed 7075 Powders

Alloy	Can Size O.D. x I.D. (ins)	Outgassing Temp. (°C)	Preheat Temp. (°C)	Preheat Time (hrs.)	Extrusion Temp. (°C)	Die Size (inches)	Reduction Ratio	Extrusion Speed (i.p.m.)	Upset Load (tons)	Running Load (tons)
7075 + Mn	2.0 x 1.87	330	390	2.5	390	.460	20:1	25	150	135
7075 + Mn	2.0 x 1.87	330	390	2.5	390	.460	20:1	25	150	140
7075 + Mn	2.0 x 1.87	330	290	1.75	300	.45	16:1	25	230/280	180
7075 + Mn	2.0 x 1.87	330	290	1.5	350	.45	16:1	25	170	140/150
7075 + Mn	2.0 x 1.87	330	290	1.5	400	.45	16:1	25	150/130	130/110
7075 + Mn/Si	2.04 x 1.87	330	300	1.5	300	.45	16:1	25	210	190
7075 + Mn/Si	2.04 x 1.87	330	350	1.5	350	.45	16:1	25	150	100
7075 + Mn/Si	2.04 x 1.87	330	400	1.5	400	.45	16:1	25	150	100
7075 + Mn/Si	2.04 x 1.87	330	450	2.0	450	.45	16:1	25	145	155
7075 + Mn/Si	5.565 x 5.502	400	450	3.0	450	0.5 x 1.5	32:1	5	1056	1162
7075 + Mn/Cr	2.04 x 1.87	330	300	1.5	300	.45	16:1	25	230	150
7075 + Mn/Cr	2.04 x 1.87	330	350	1.5	350	.45	16:1	25	150	100
7075 + Mn/Cr	2.04 x 1.87	330	400	1.5	400	.45	16:1	25	190	150
7075 + Mn/Cr	2.04 x 1.87	330	450	2.0	450	.45	16:1	25	210	200

TABLE XIV
Mechanical Property Data for Manganese Modified 7075 Powder

Temper Condition	Extrusion Temp °C	Extrusion Ratio	Elastic Modulus GPa (10 ⁶ Psi)	Yield Strength MPa (ksi)	Ultimate Strength MPa (ksi)	% EL Elongation	Subsize Charpy J (ft-lb)
T6	390	20:1	76.5 (11.1)	693 (100.5)	750 (108.7)	1.7	0.44 (0.34)
0	390	20:1	77.2 (11.2)	282 (41.7)	439 (63.6)	5.2	0.98 (0.75)
T73	390	20:1	75.2 (10.9)	521 (75.6)	601 (87.2)	1.9	0.52 (0.40)
T76	390	20:1	75.2 (10.9)	558 (80.9)	575 (83.4)	0.5	0.51 (0.39)
4hr/120°C + 20hr/170°C	390	20:1	75.2 (10.9)	454 (65.8)	568 (82.4)	3.3	----
4hr/120°C + 20hr/180°C	390	20:1	75.2 (10.9)	425 (61.6)	558 (81.0)	6.1	----
4hr/120°C + 20hr/190°C	390	20:1	75.2 (10.9)	341 (49.5)	498 (72.2)	6.7	----
4hr/120°C + 20hr/200°C	390	20:1	75.2 (10.9)	325 (47.2)	488 (70.8)	7.1	----

TABLE XV
Comparison of Modified Alloys at Various Extrusion Temperatures T6 Temper

Ext. Temp.	Mn-Modified				Mn-Si Modified				Mn-Cr Modified			
	UTS (MPa)	YS (MPa)	Elastic Modulus (GPa)	% Elongation	UTS (MPa)	YS (MPa)	Elastic Modulus (GPa)	% Elongation	UTS (MPa)	YS (MPa)	Elastic Modulus (GPa)	% Elongation
300°C	788.0	--	--	<1	636.4	--	--	2.17	610.5	546.5	72.65	2.65
350°C	763.0	--	--	<1	676.0	663.5	77.57	3.58	606.9	536.6	83.76	2.58
400°C	754.25	--	--	<1	724.0	692.6	78.26	4.16	635.2	548.9	81.03	4.26
450°C	--	--	--	--	680.7	640.4	82.26	6.19	593.8	529.8	78.2	5.6
450°C Plate	--	--	--	--	614.15	562.73	69.86	7.89	--	--	--	--

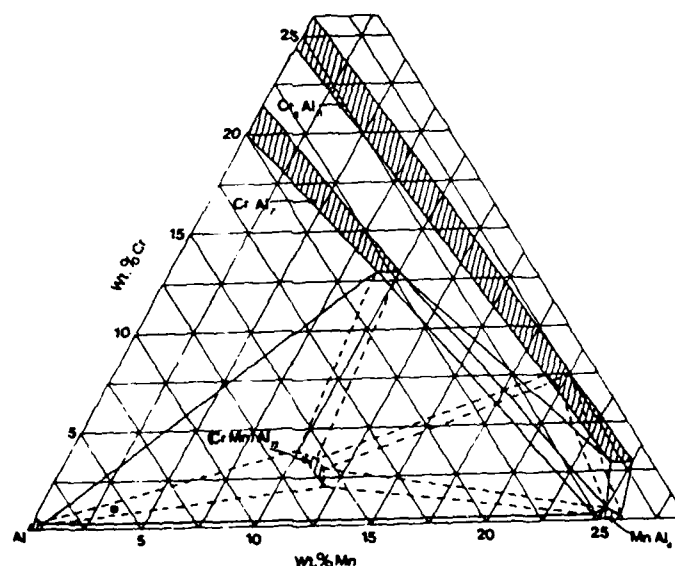
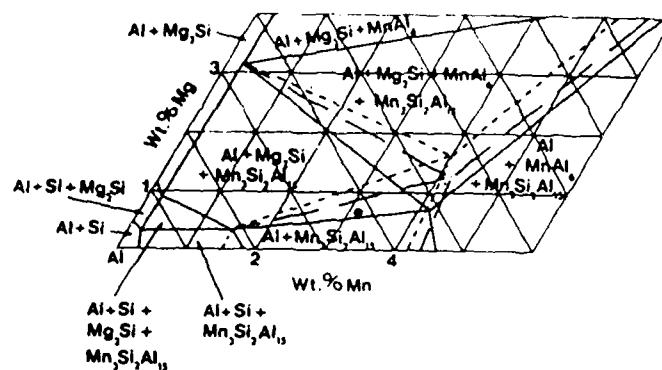


Figure 22 (a) Section of the Aluminum - Magnesium - Manganese - Silicon - Zinc diagram at 730 K and 1% Si. Solid lines, 0% Zn; dotted line, 4% Zn; dashed line, 8% Zn, (b) Aluminum corner of the Aluminum - Chromium - Manganese diagram showing phase distribution at 900 K (solid lines) and 820 K (dashed lines).

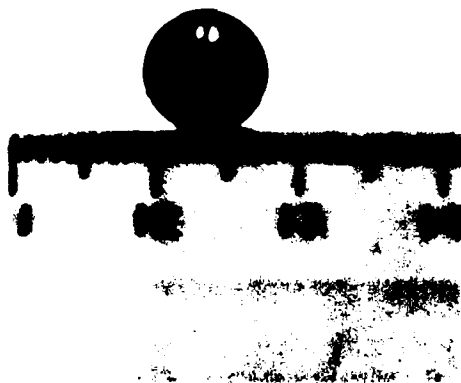


(a)

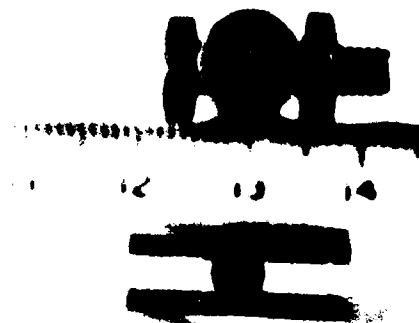


(b)

Figure 23 Tensile test samples: (a) room temperature, (b) high temperature.



(a)



(b)

Figure 24 Corrosion samples: (a) weight loss test, (b) stress corrosion cracking.

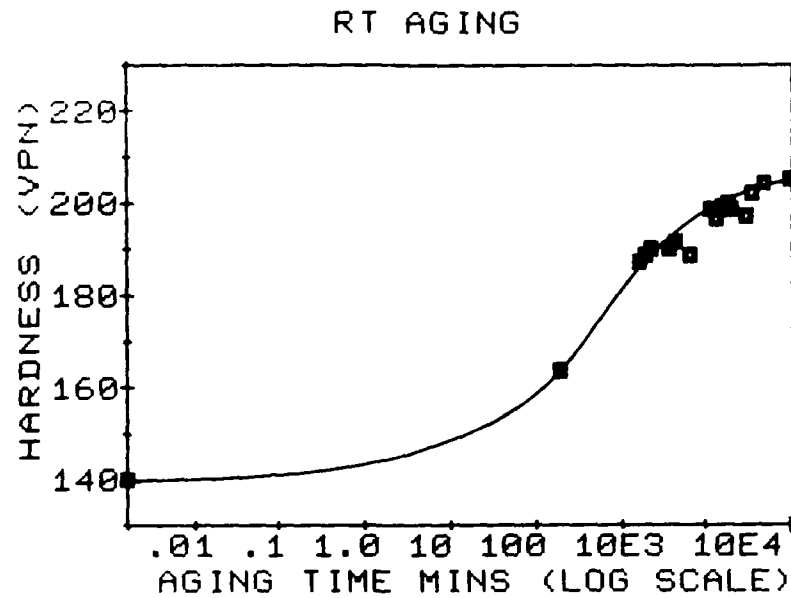


Figure 25 Vickers hardness versus aging time in minutes representing aging response, alloy aged at room temperature.

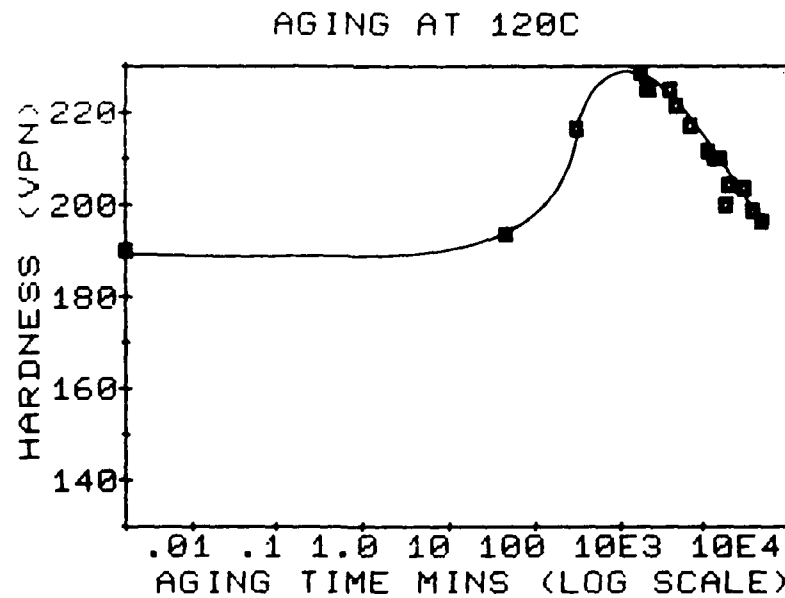


Figure 26 Vickers hardness versus aging time in minutes representing aging response, alloy aged at 120°C.

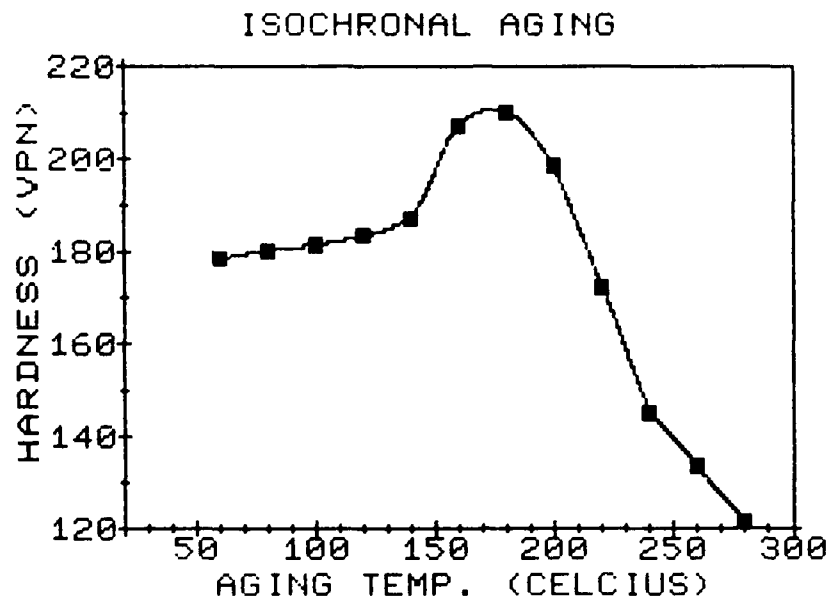


Figure 27 Isochronal aging response for a 10 minute time interval during a temperature range of 60° C to 280° C for a 20° C increment.

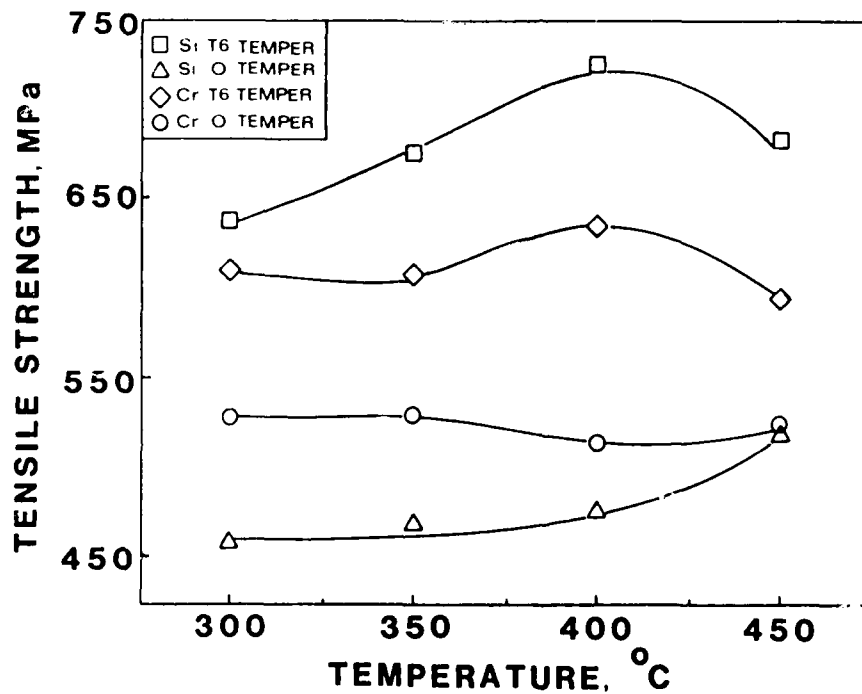


Figure 28 Variation of tensile strength with extrusion temperature.

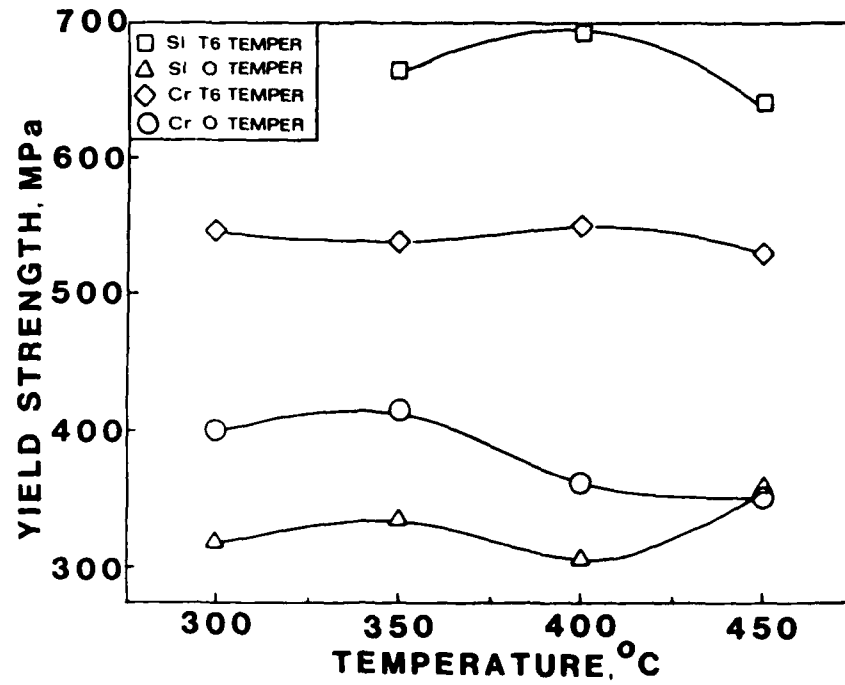


Figure 29 Variation of yield strength with extrusion temperature.

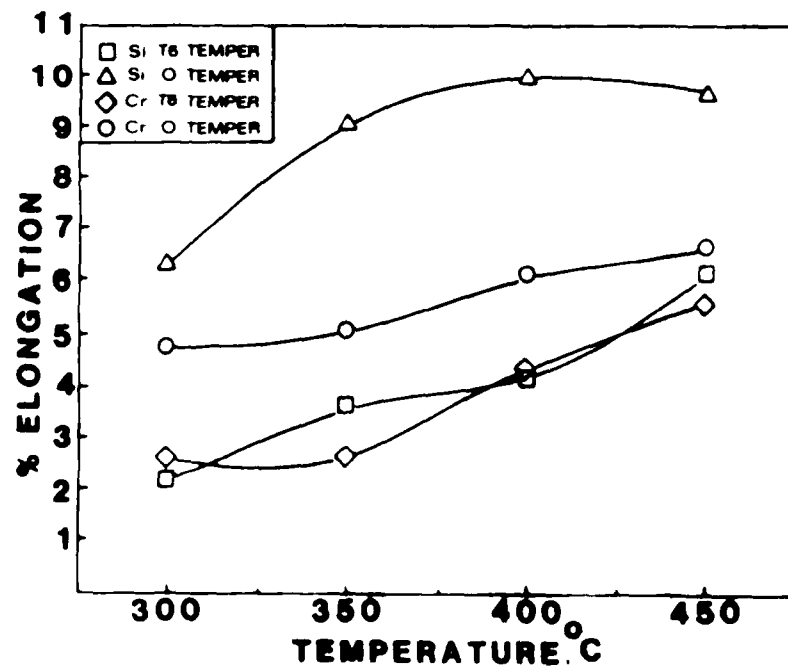


Figure 30 Variation of % elongation with extrusion temperature.

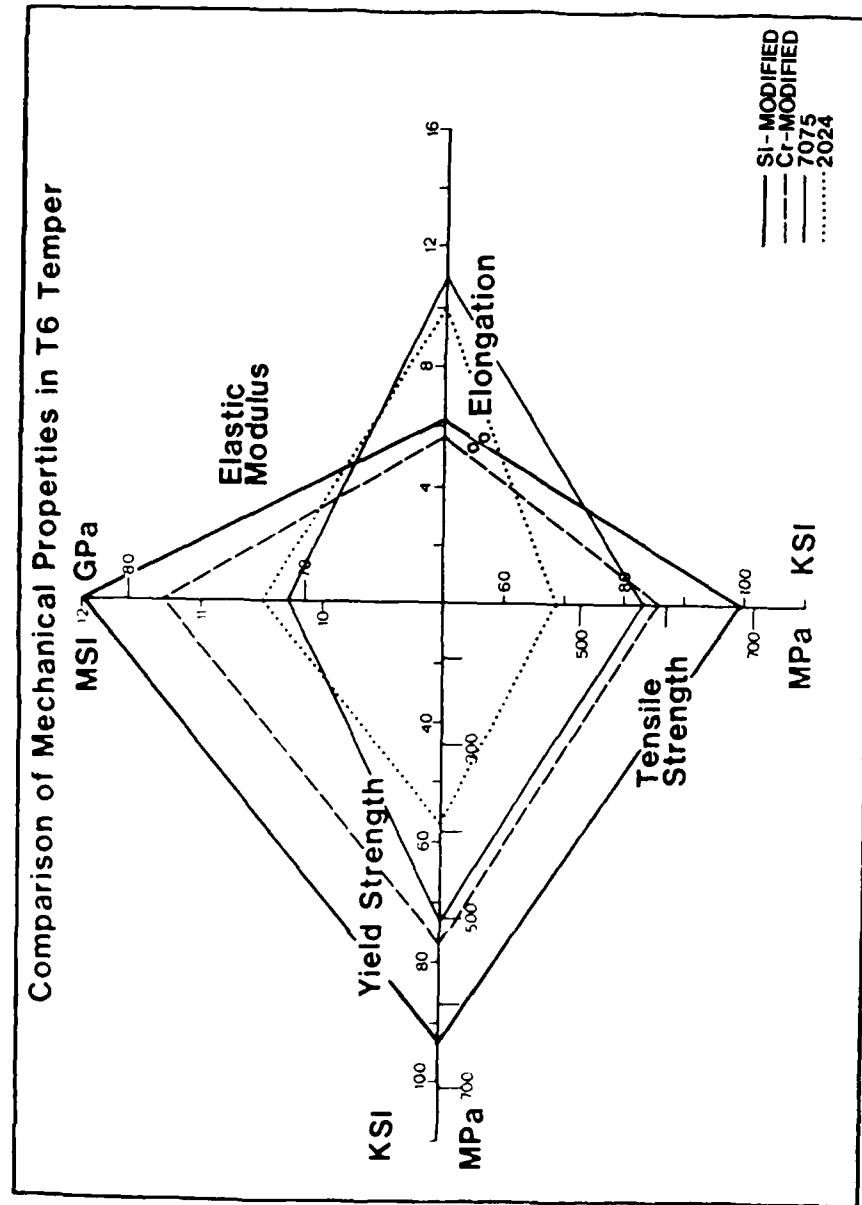


Figure 31 Comparison of mechanical properties in T6 temper of various aluminum alloys. Data for I/M 7075 and I/M 2024 taken from metals handbook.

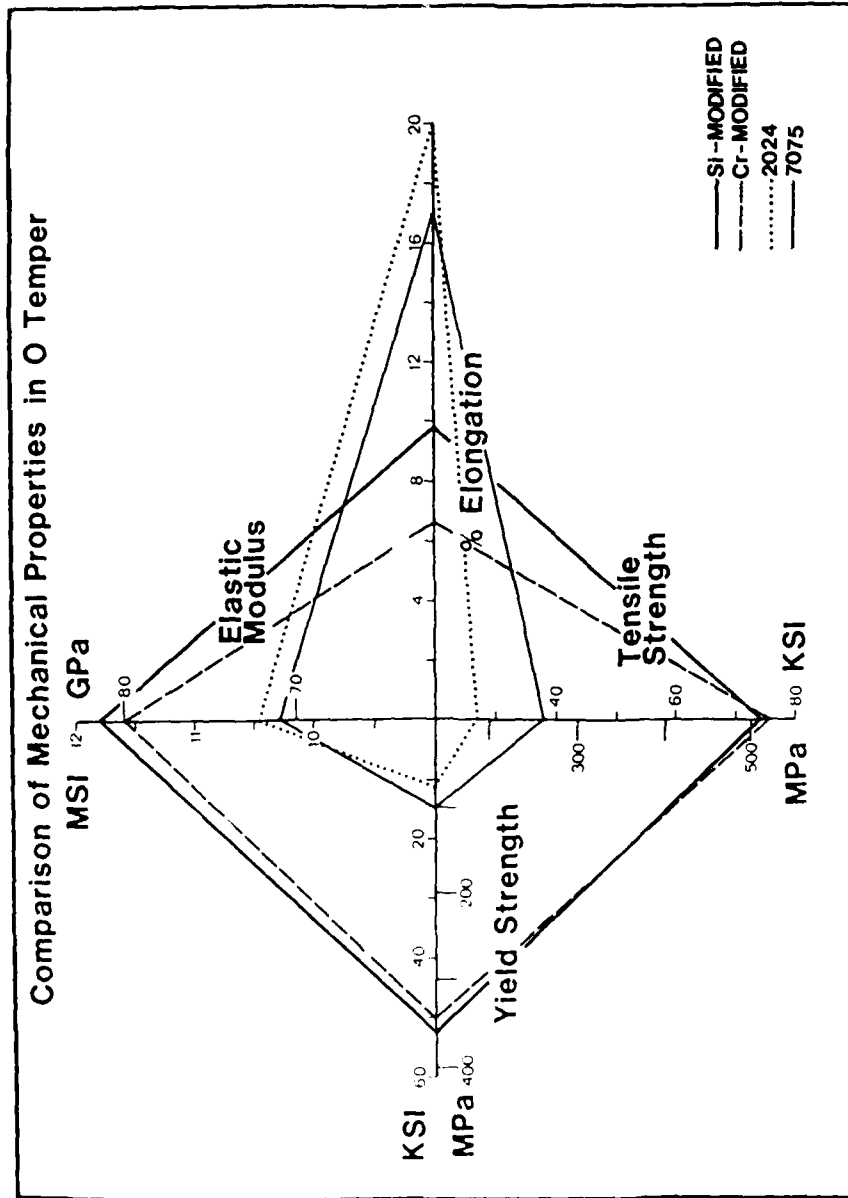


Figure 32 Comparison of mechanical properties in O temper of various aluminum alloys. Data for I/M 7075 and I/M 2024 taken from metals handbook.

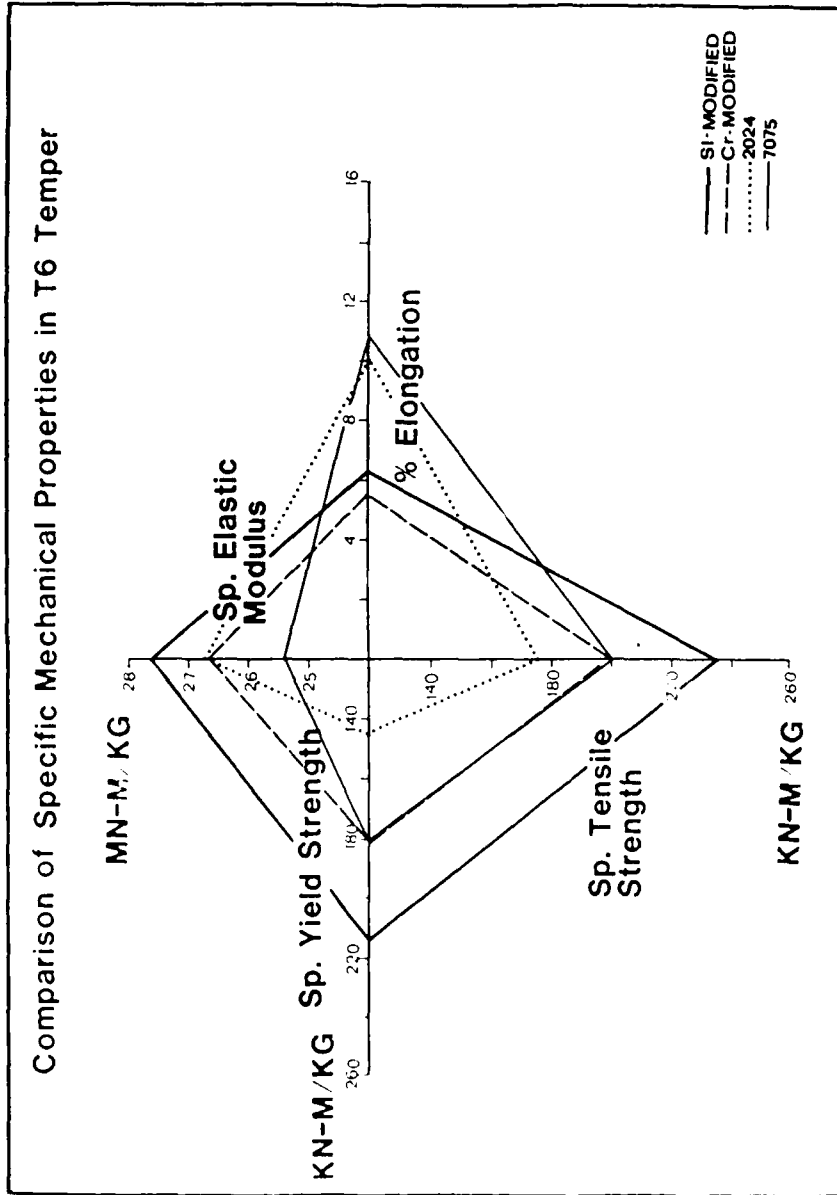


Figure 33 Comparison of specific mechanical properties in T6 temper of various aluminum alloys. Data for I/M 7075 and I/M 2024 taken from metals handbook.

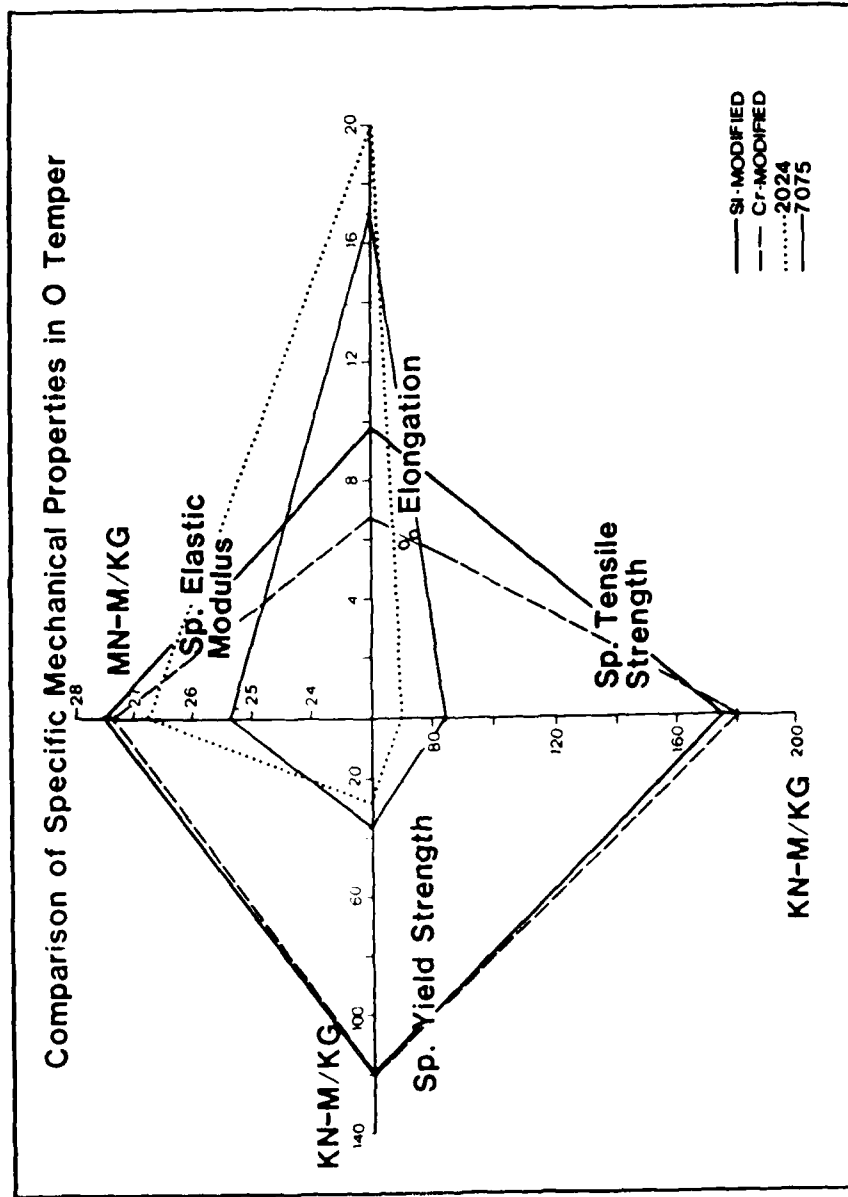


Figure 34 Comparison of specific mechanical properties in O temper of various aluminum alloys. Data for I/M 7075 and I/M 2024 taken from metals handbook.

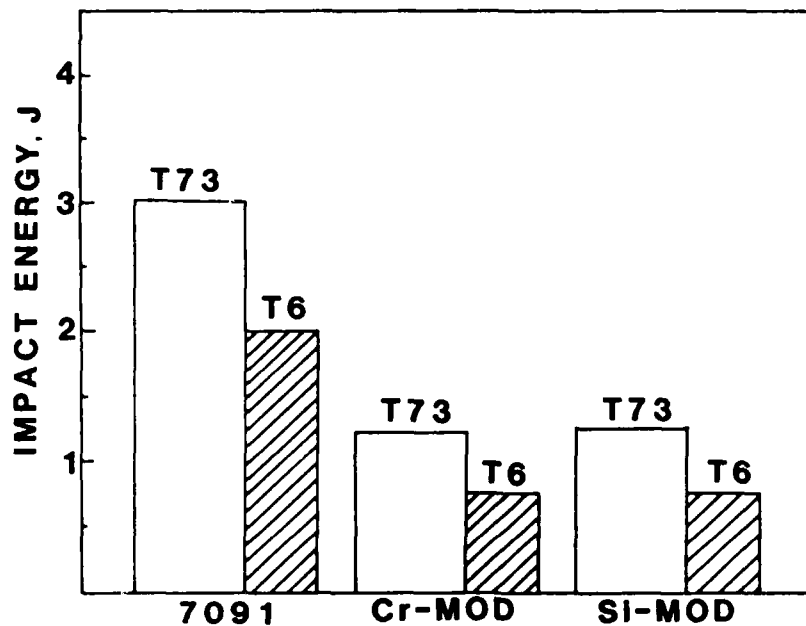


Figure 35 Comparison of notched impact strength of various alloys in T6 and T73 tempers.

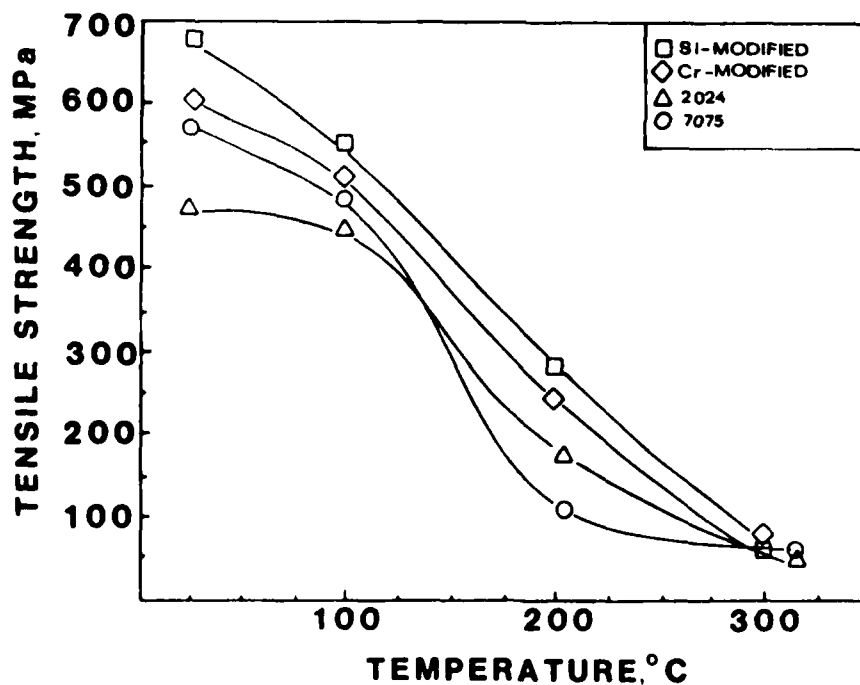


Figure 36 Comparison of tensile strength at elevated temperatures of different aluminum alloys. Data for I/M 7075 and I/M 2024 taken from handbook. Time at test: 10 minutes.

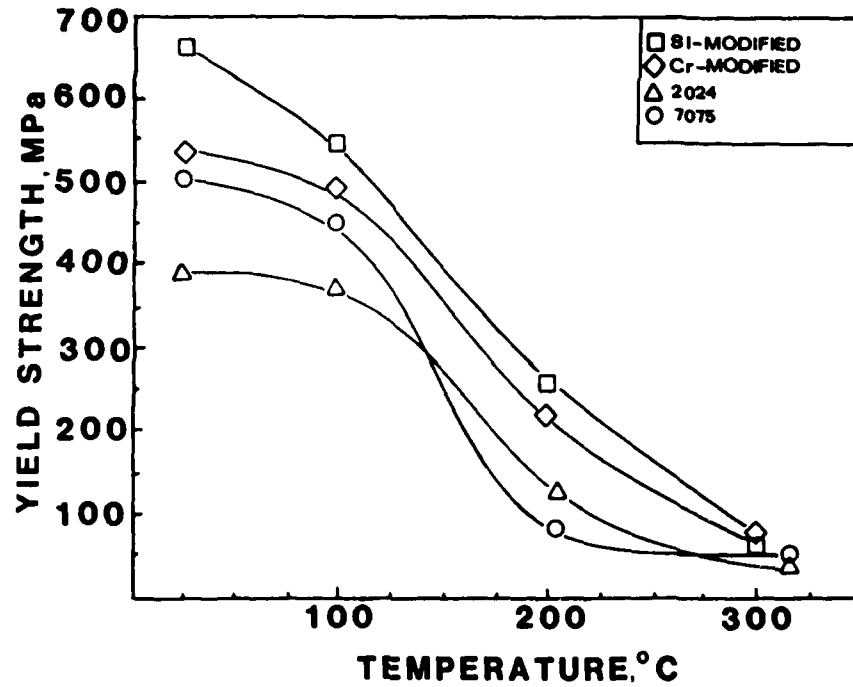


Figure 37 Comparison of yield strength at elevated temperatures of different aluminum alloys. Data for I/M 7075 and I/M 2024 taken from handbook. Time at test: 10 minutes.

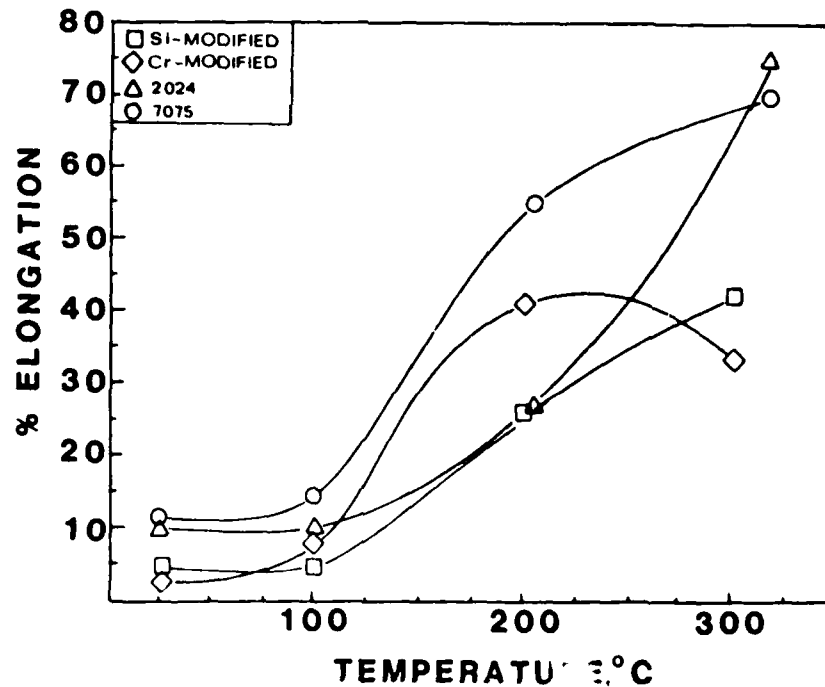


Figure 38 Comparison of % elongation at elevated temperatures of different aluminum alloys. Data for I/M 7075 and I/M 2024 taken from handbook. Time at test: 10 minutes.

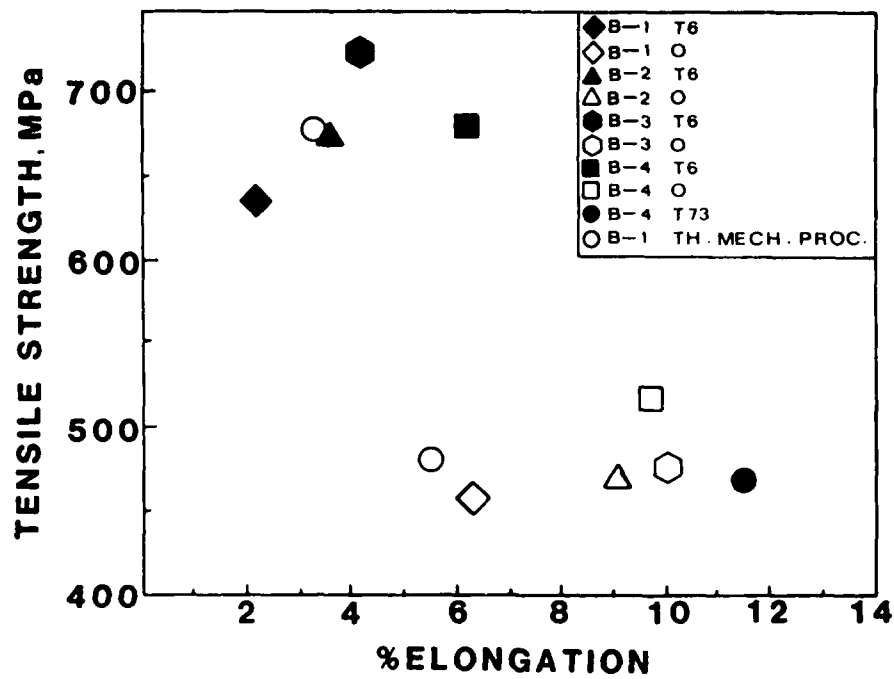


Figure 39 Figure showing range of strength-elongation combinations obtained for the silicon modified alloy.

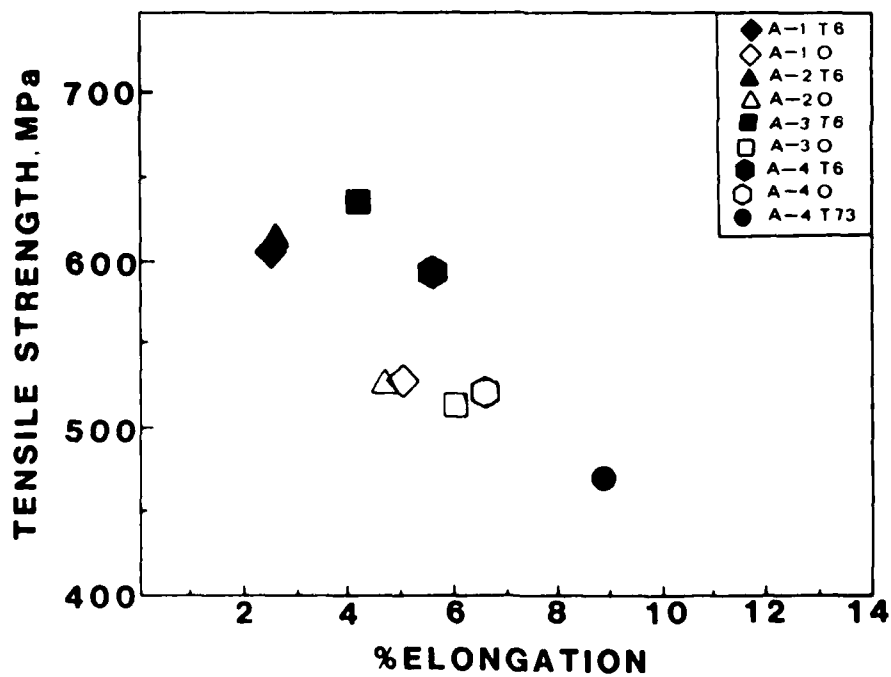


Figure 40 Figure showing range of strength-elongation combinations obtained for the chromium modified alloy.



Figure 41 Optical micrograph of prealloyed Mn modified inert gas atomized powder, oversize fraction.



Figure 42 SEM micrograph of prealloyed Mn modified inert gas atomized powder, oversize fraction.

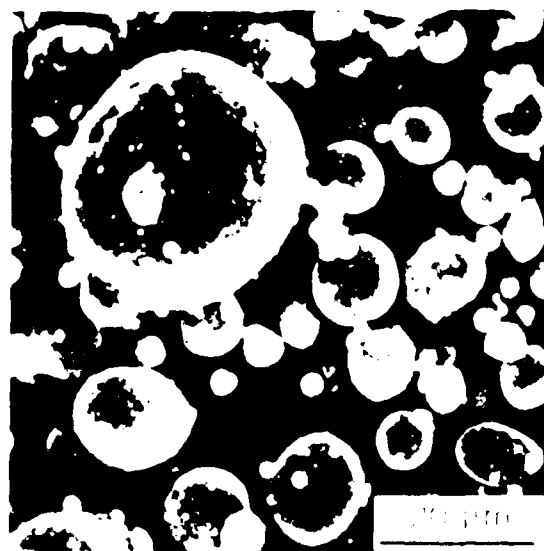


Figure 43 SEM micrograph of prealloyed Mn modified inert gas atomized powder, -325 mesh fraction.

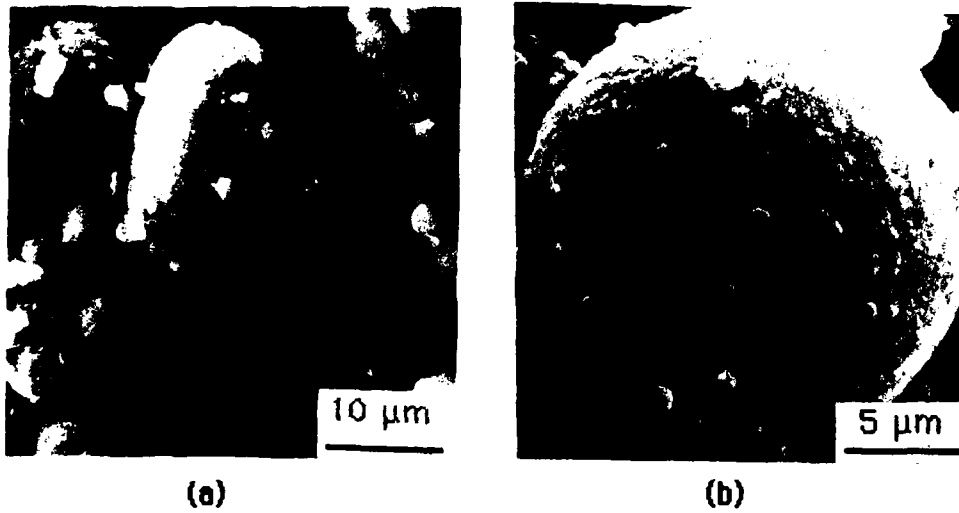


Figure 44 Scanning Electron Microscope micrograph of prealloyed silicon modified helium gas atomized powders, -400 mesh fraction.

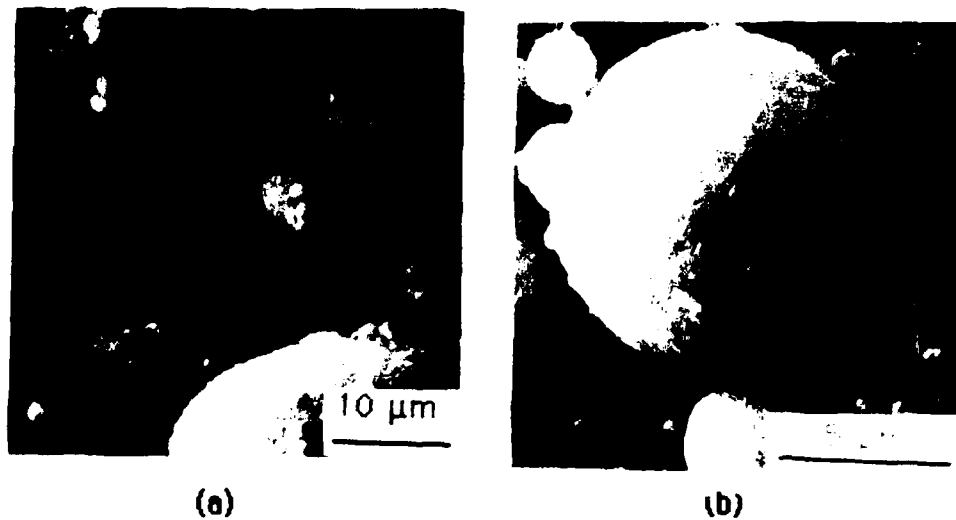
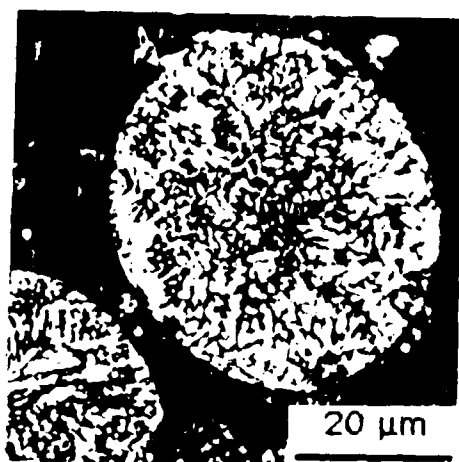
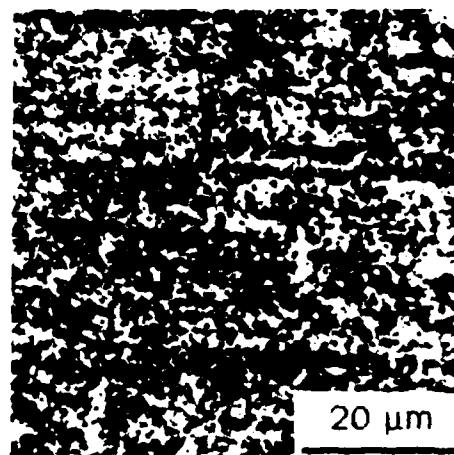


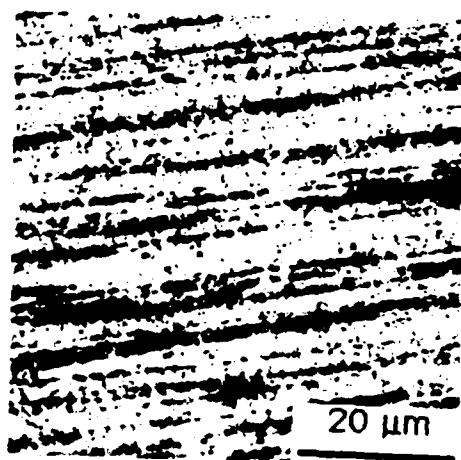
Figure 45 Scanning Electron Microscope micrograph of prealloyed chromium modified helium gas atomized powders, -400 mesh fraction.



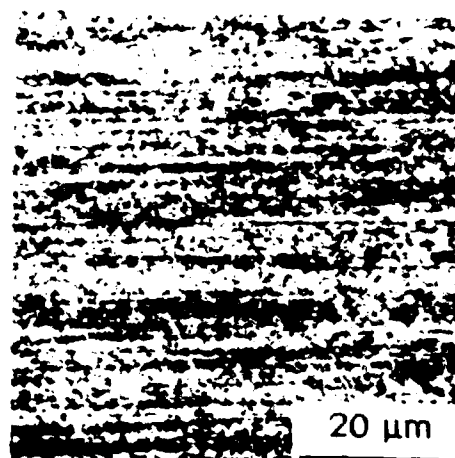
(a) powder



(b) as received

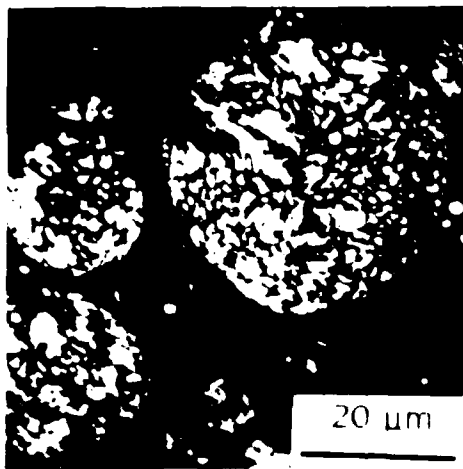


(c) T6 Temper

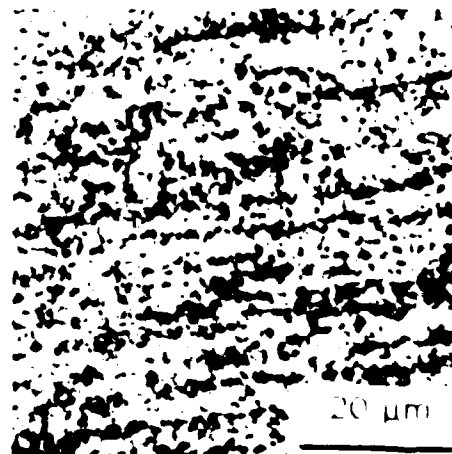


(d) O Temper

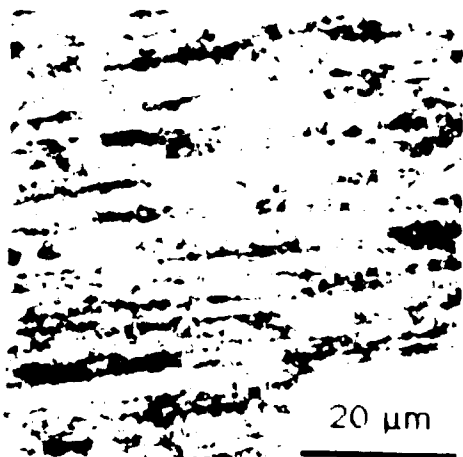
Figure 46 Optical micrographs of the silicon modified alloy in various tempers.



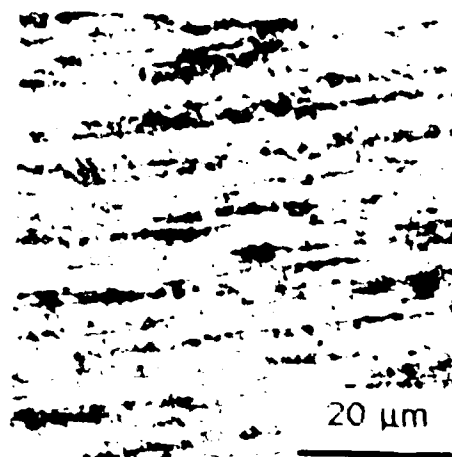
(a) powder



(b) as received



(c) T6 Temper



(d) O Temper

Figure 47 Optical micrographs of the chromium modified alloy in various tempers.

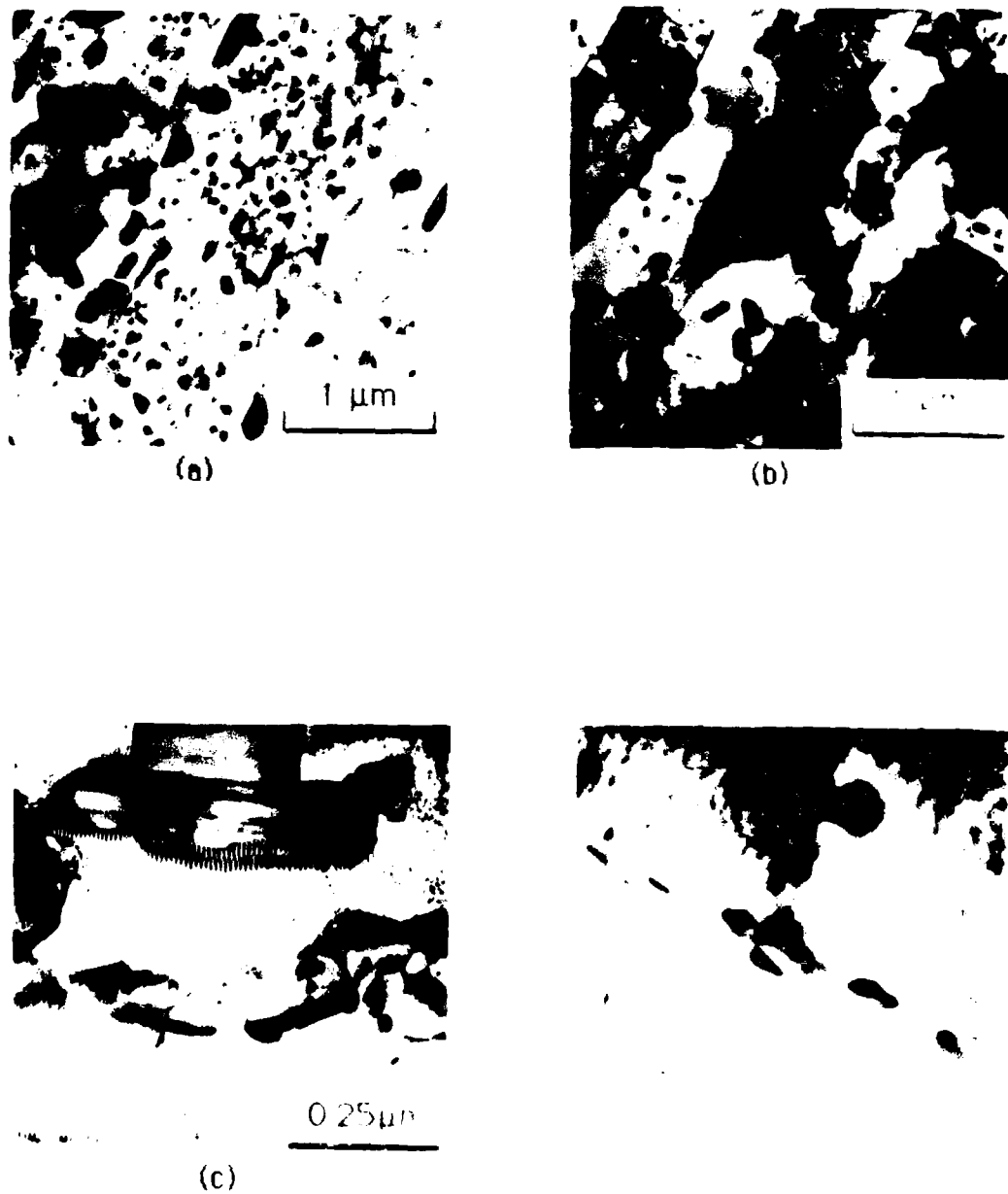


Figure 48 Transmission electron micrographs of modified alloy in 16 temperature range.

AD-A175 777

DEVELOPMENT OF HIGH MODULUS CORROSION RESISTANT
ALUMINUM ALLOYS(U) DREXEL UNIV PHILADELPHIA PA DEPT OF
MATERIALS ENGINEERING H J KOCZAK ET AL. JAN 86
NADC-86074-60 N62269-81-R-0743

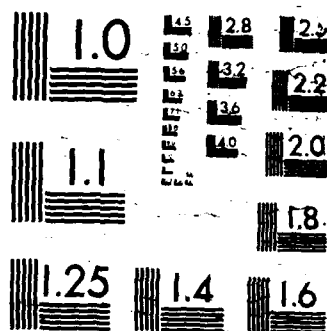
2/2

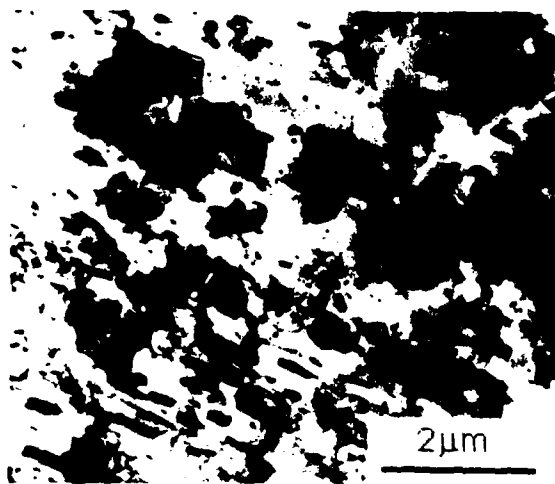
UNCLASSIFIED

F/G 11/6

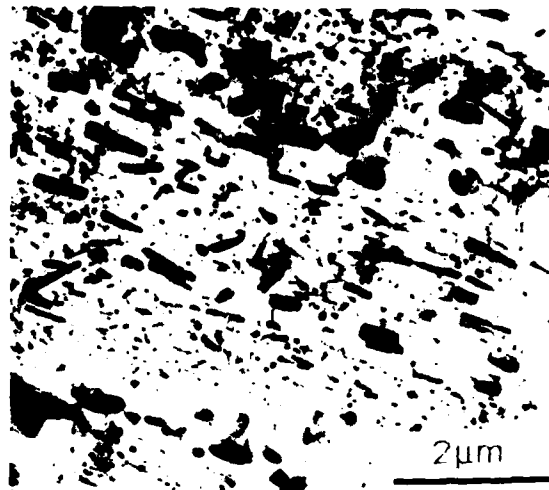
NL



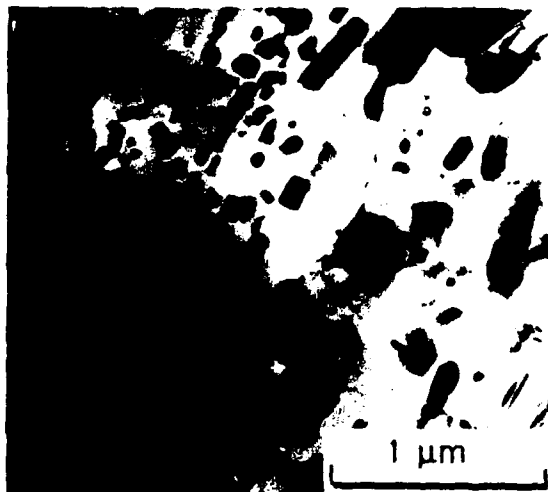




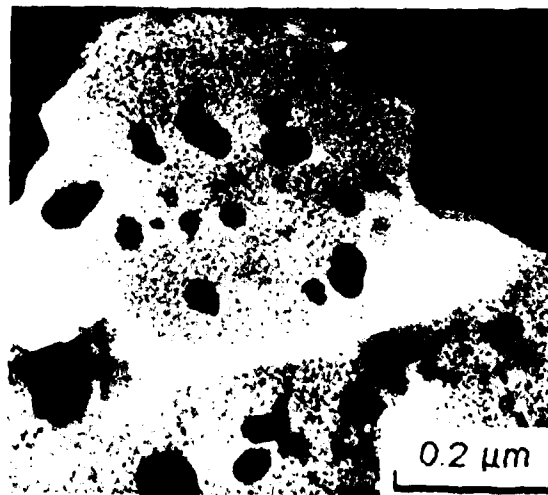
(a)



(b)



(c)

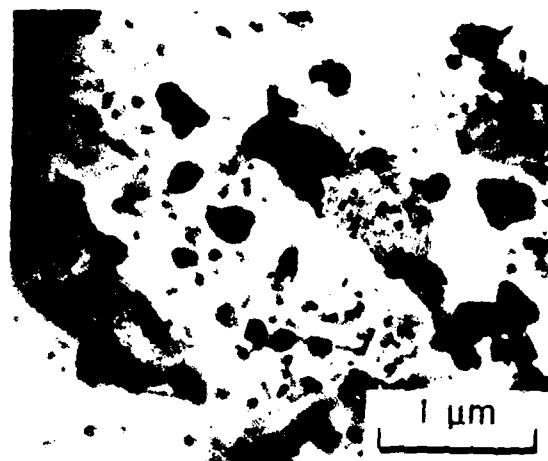


(d)

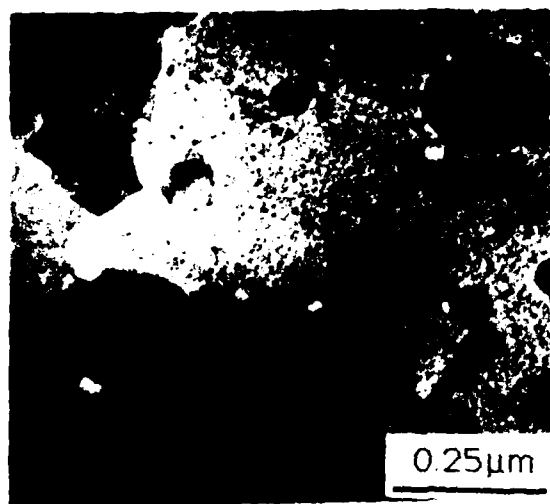
Figure 49 Transmission electron micrographs of the manganese modified alloy in T6 temper extruded at 400° C.



(a)



(b)

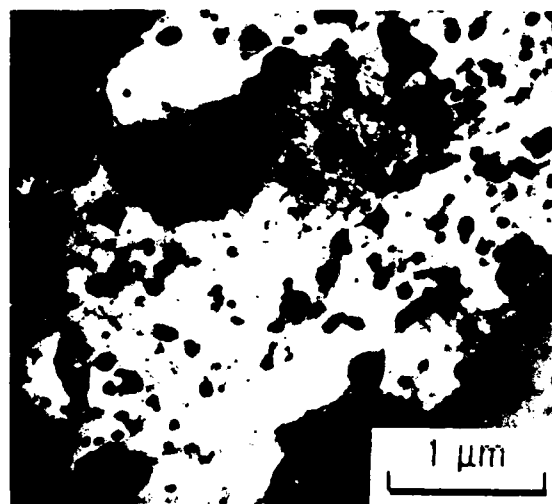


(c)

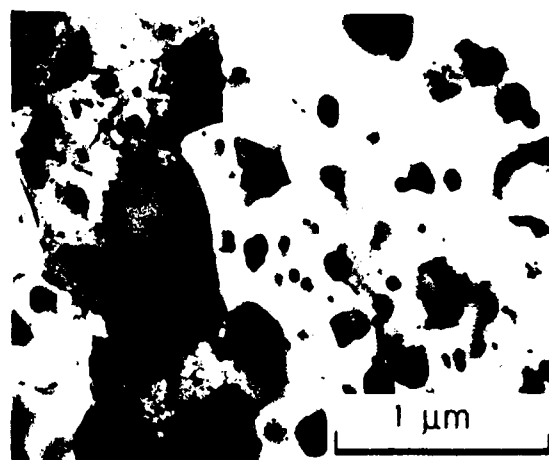


(d)

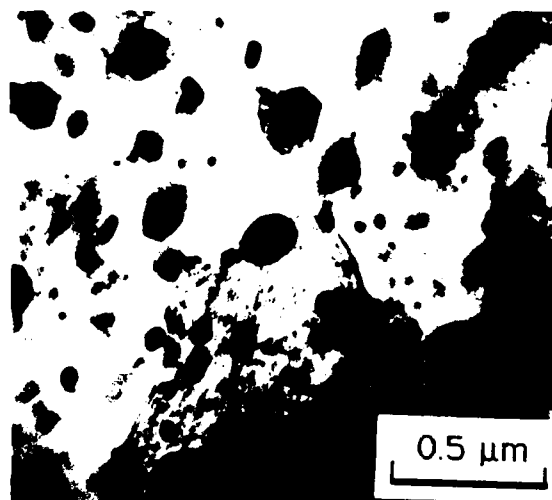
Figure 50 Transmission electron micrographs of the silicon modified alloy in T6 temper extruded at 300° C.



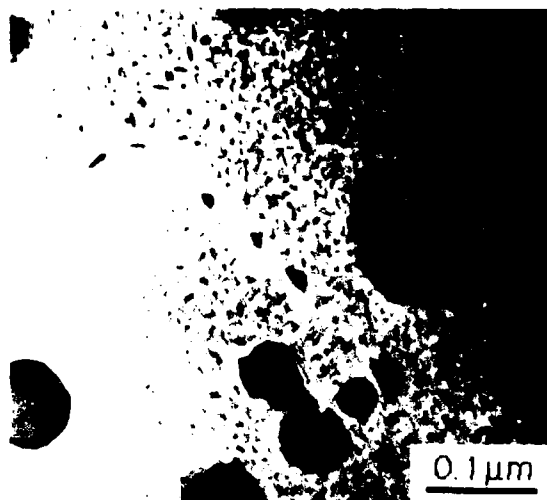
(a)



(b)



(c)



(d)

Figure 51 Transmission electron micrographs of the silicon modified alloy in T6 temper extruded at 450° C.

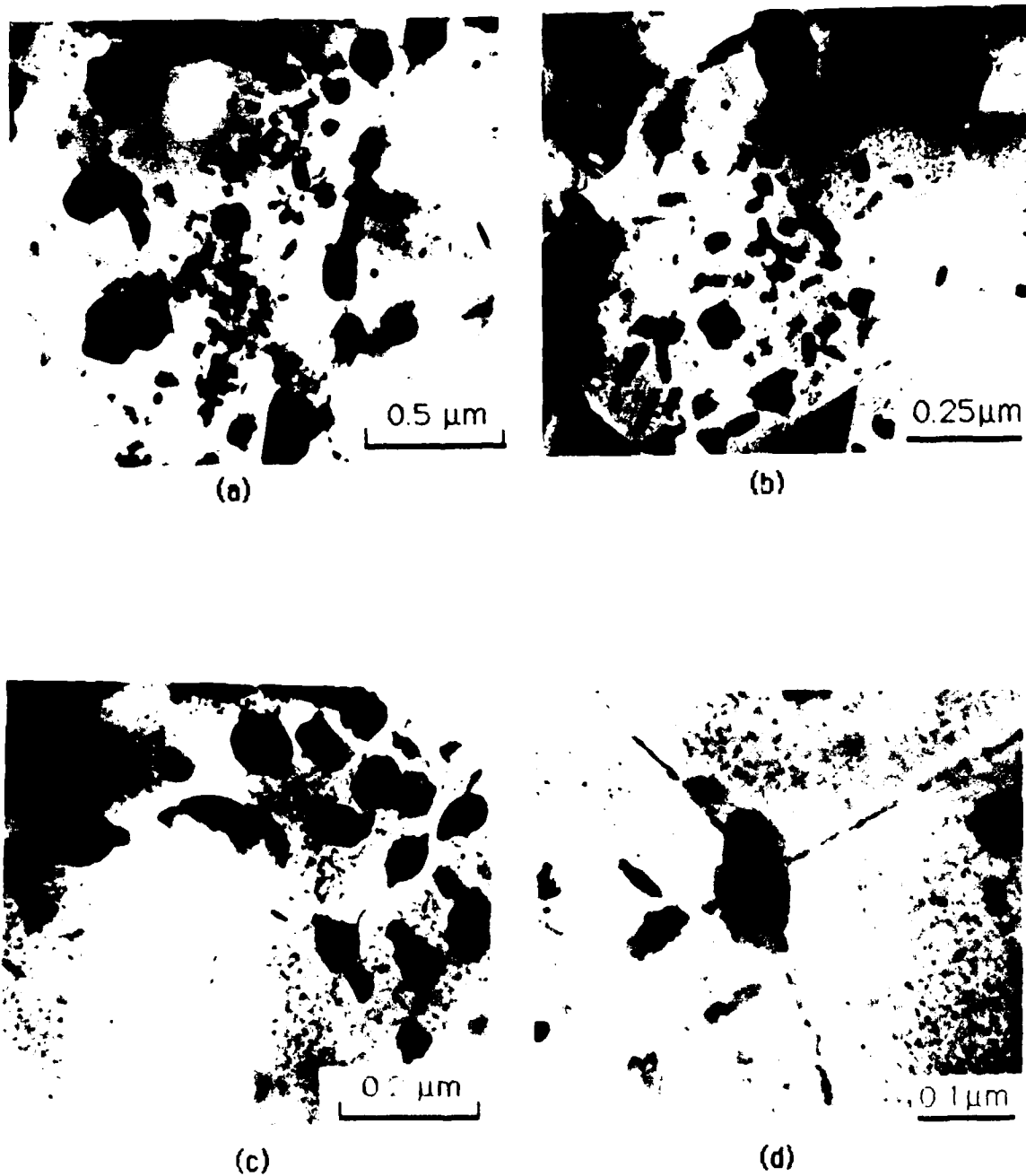


Figure 52 Transmission electron micrographs of the chromium modified alloy in T6 temper extruded at 300°C.

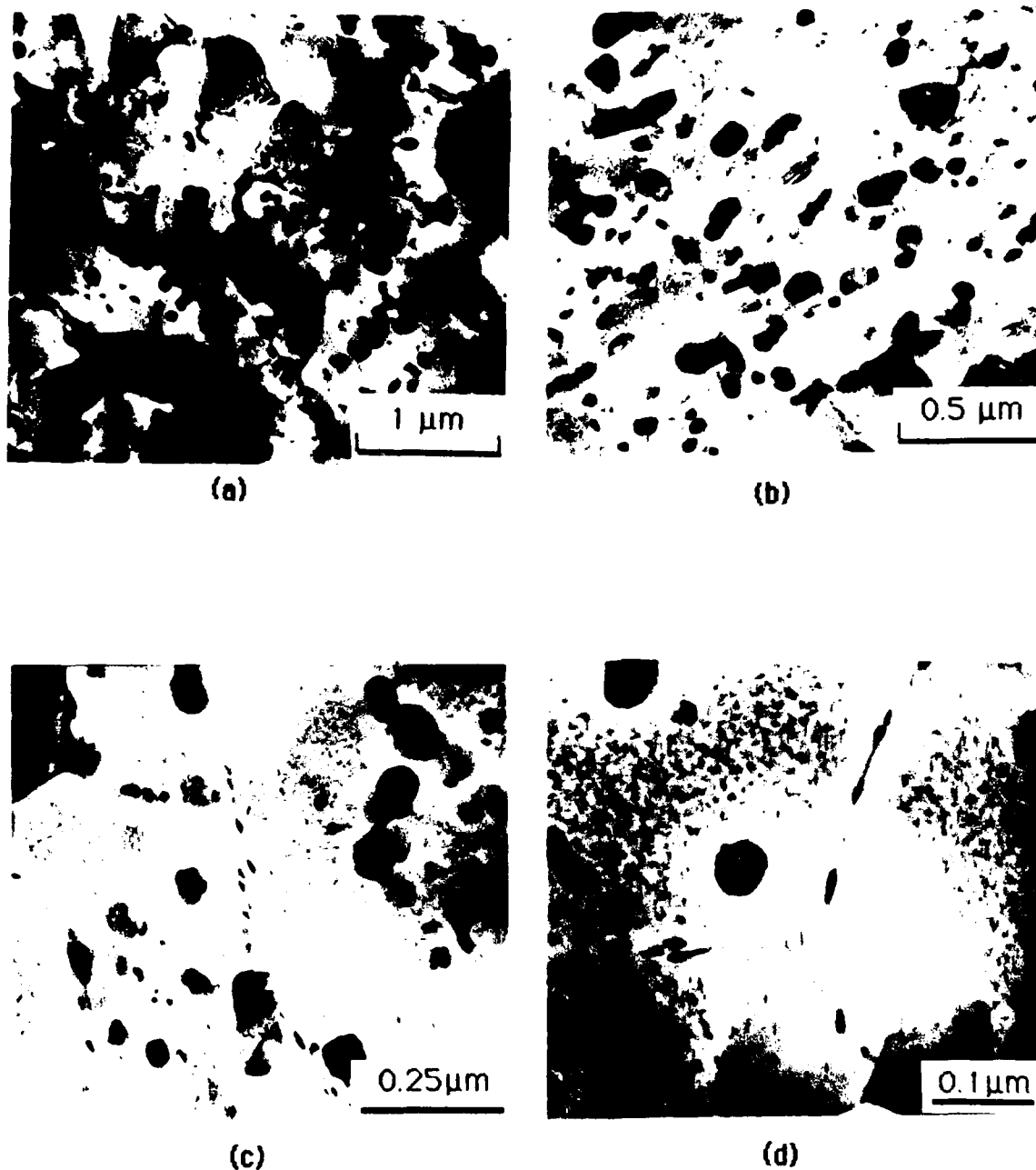


Figure 53 Transmission electron micrographs of the chromium modified alloy in T6 temper extruded at 450° C.

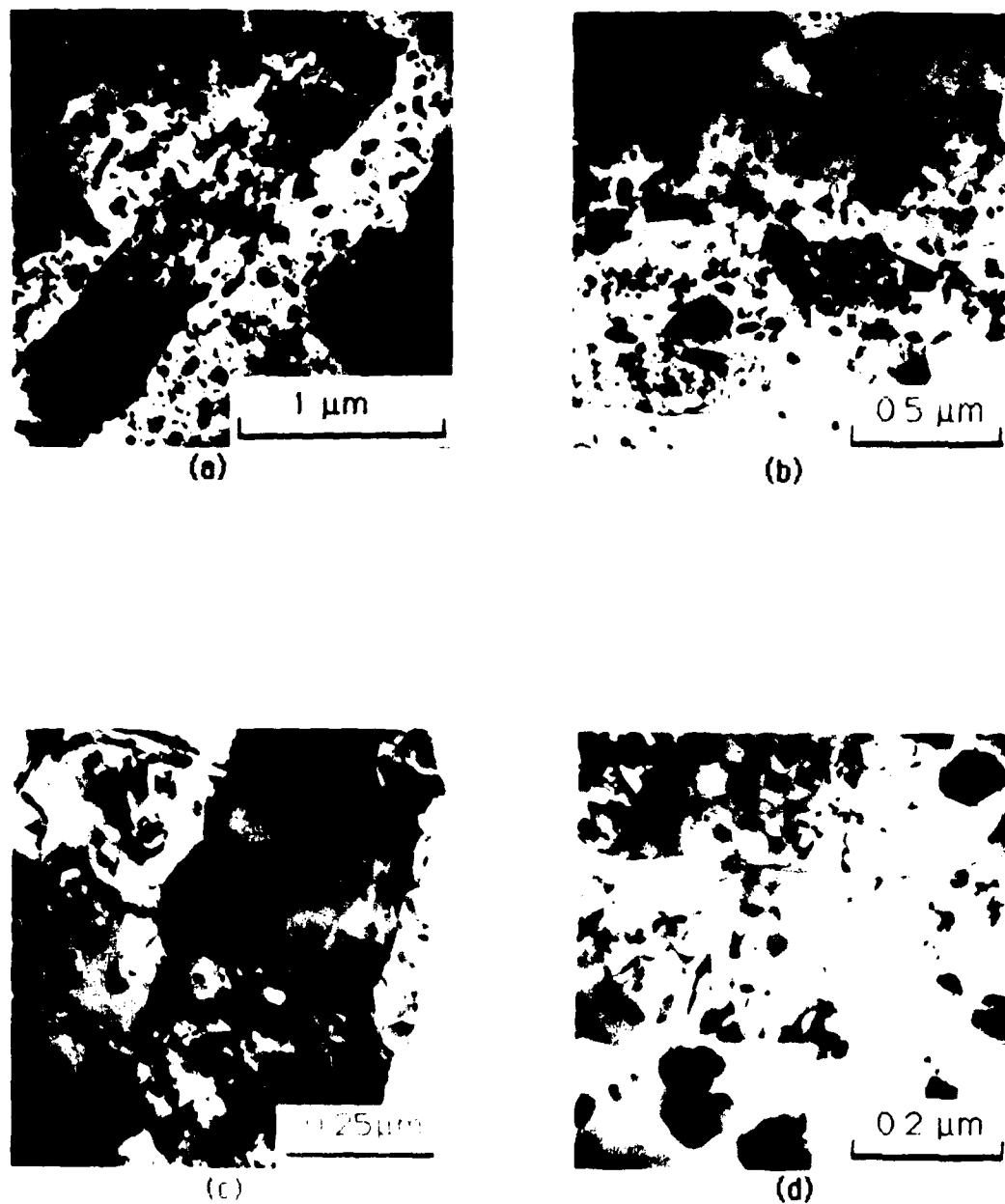
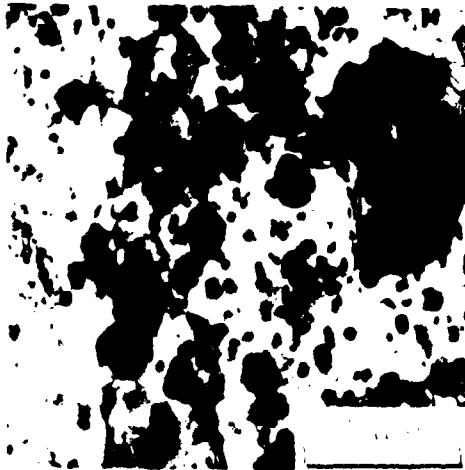
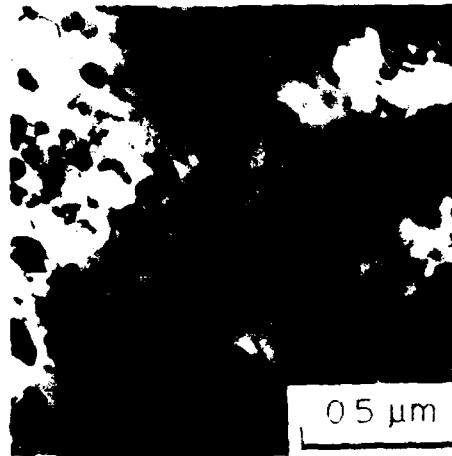


Figure 54 Transmission electron micrographs of the silicon modified alloy in as extruded condition at 300° C.



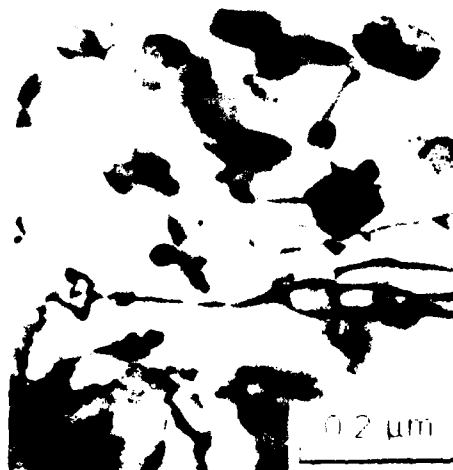
(a)



(b)

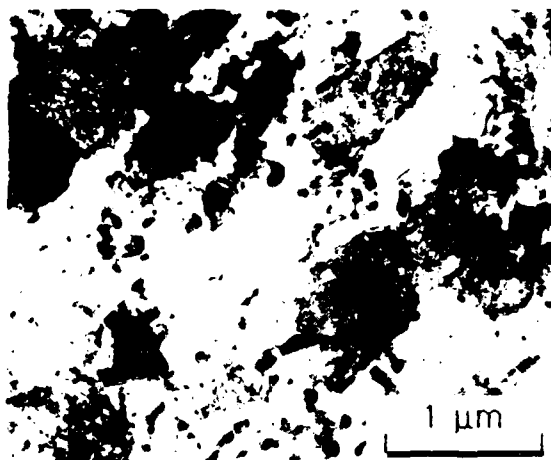


(c)

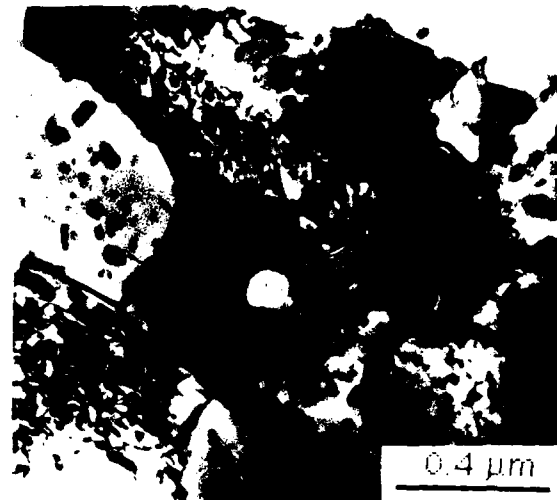


(d)

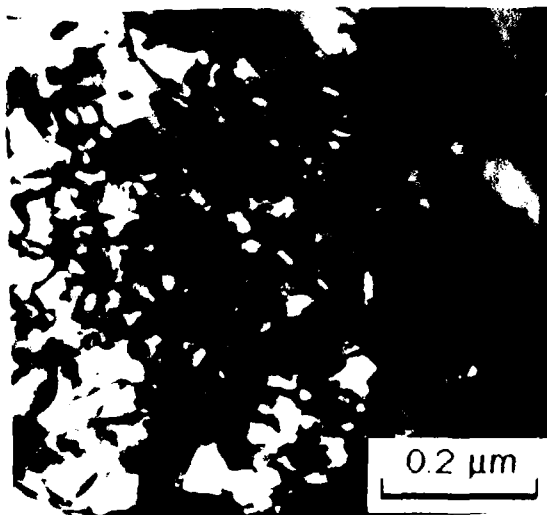
Figure 55 Transmission electron micrographs of the silicon modified alloy in as extruded condition at 450° C.



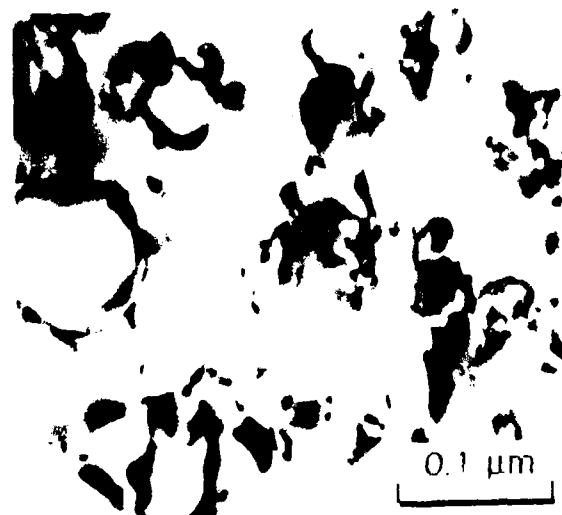
(a)



(b)

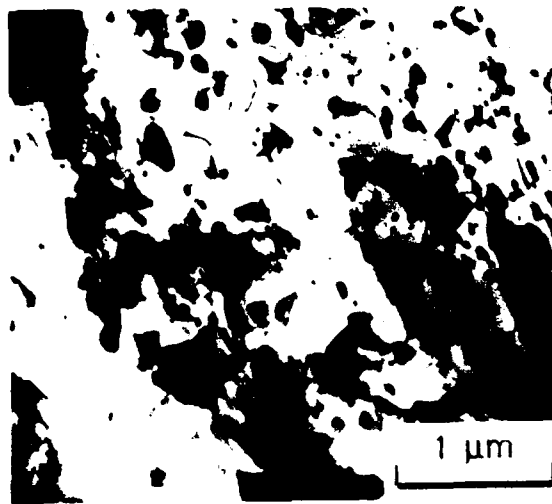


(c)

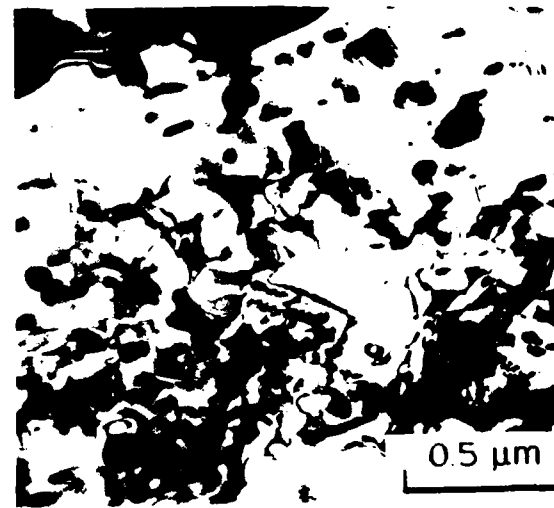


(d)

Figure 56 Transmission electron micrographs of the chromium modified alloy in as extruded condition at 300° C.



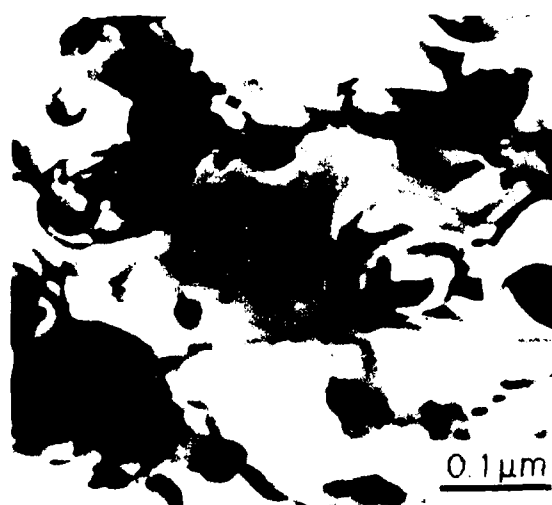
(a)



(b)

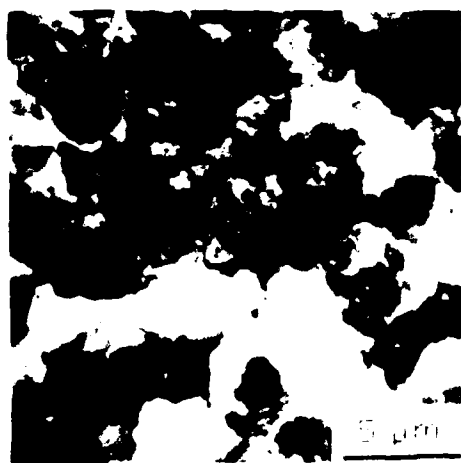


(c)

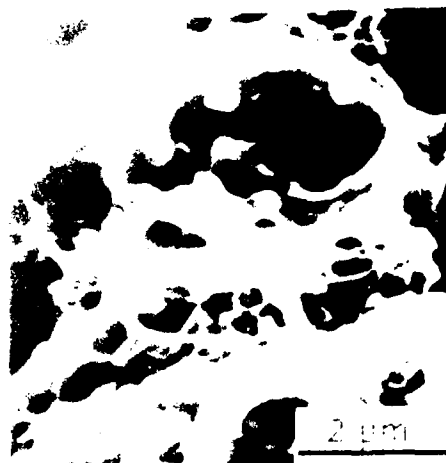


(d)

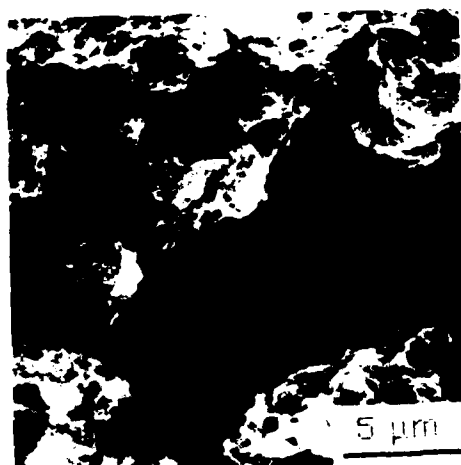
Figure 57 Transmission electron micrographs of the chromium modified alloy in as extruded condition at 450° C.



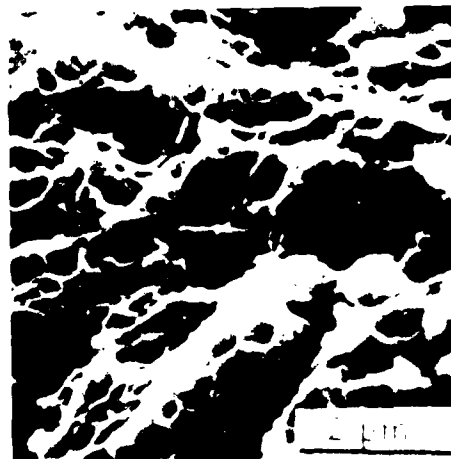
(a)



(b)

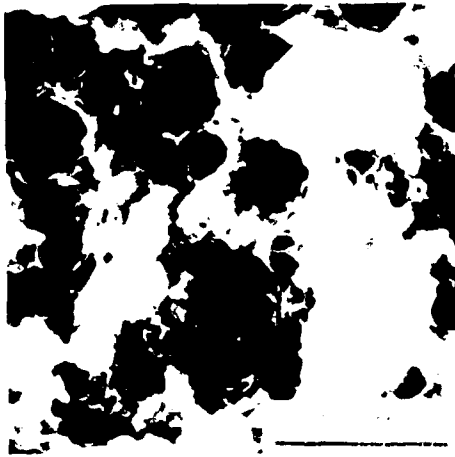


(c)

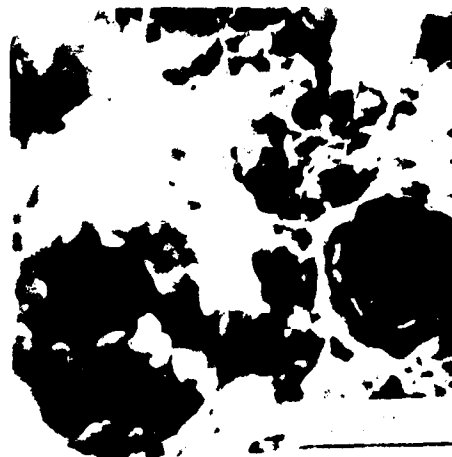


(d)

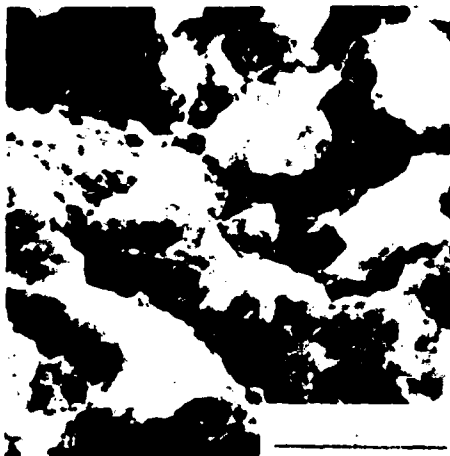
Figure 58 Fracture surfaces of tensile samples; silicon modified alloy T6 temper. (a) and (b) extruded at 300°C, (c) and (d) extruded at 450°C.



(a)



(b)



(c)



(d)

Figure 59 Fracture surfaces of tensile samples; chromium modified alloy T6 temper. (a) and (b) extruded at 300° C, (c) and (d) extruded at 450° C.

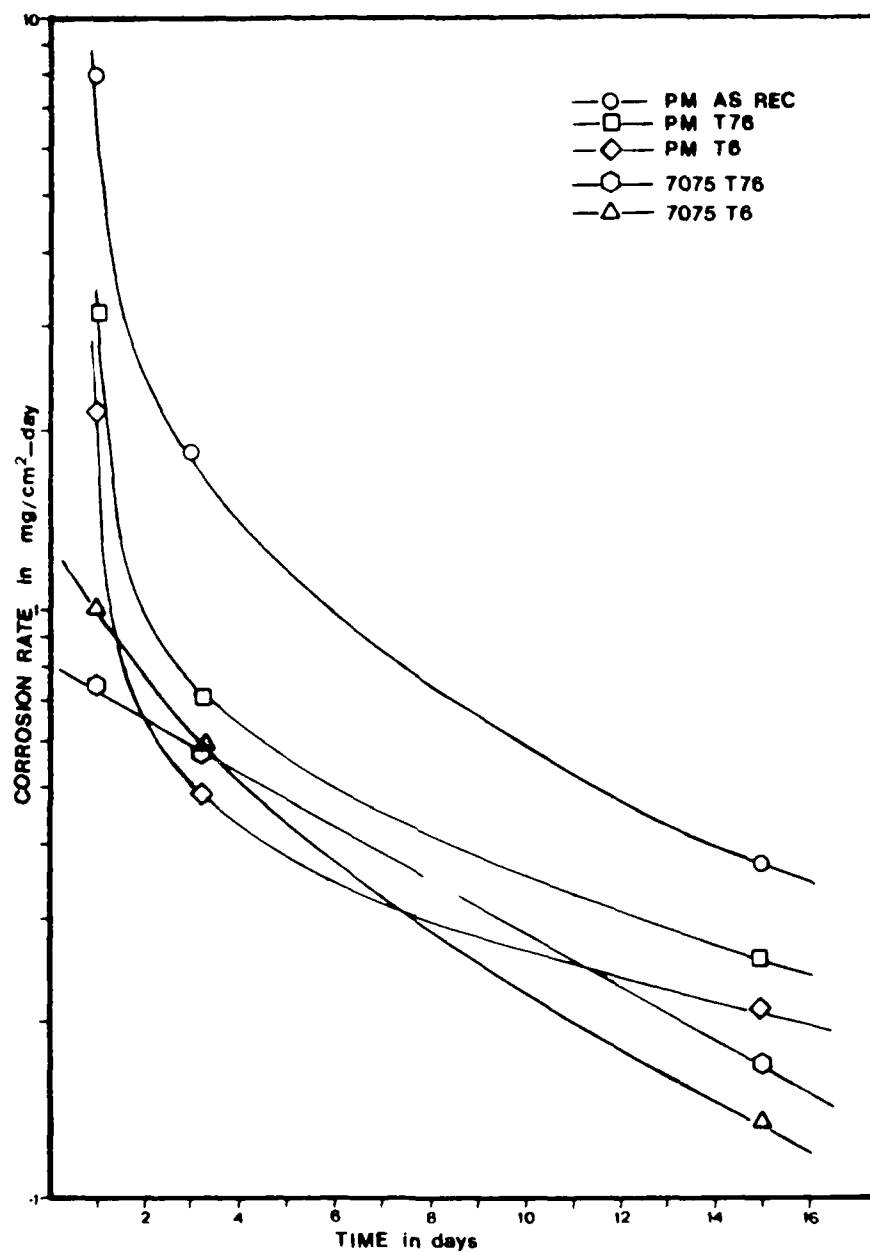


Figure 60 Comparison of weight loss as a function of time. PM represents prealloyed manganese alloy. Corrosion test medium: 1% NaCl + pH2.

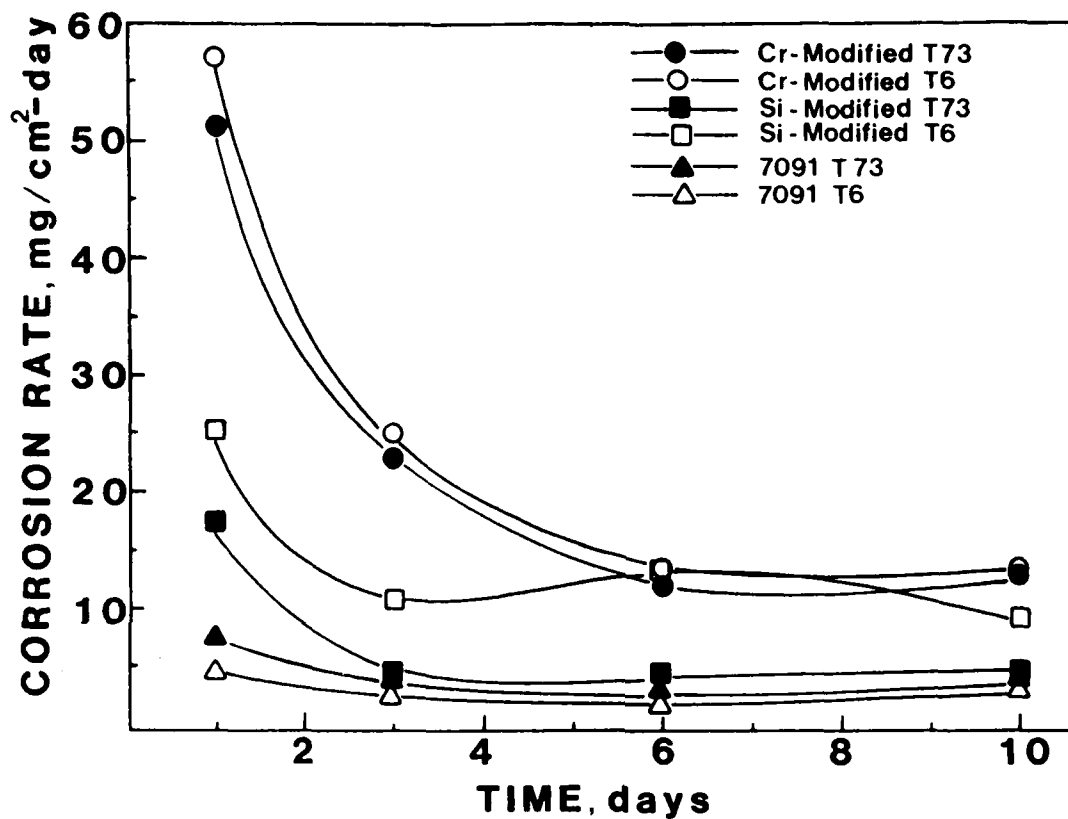


Figure 61 Comparison of corrosion rates of different aluminum alloys. Corrosion medium: 1% NaCl + pH2. Corrosion rate determined by weight loss.

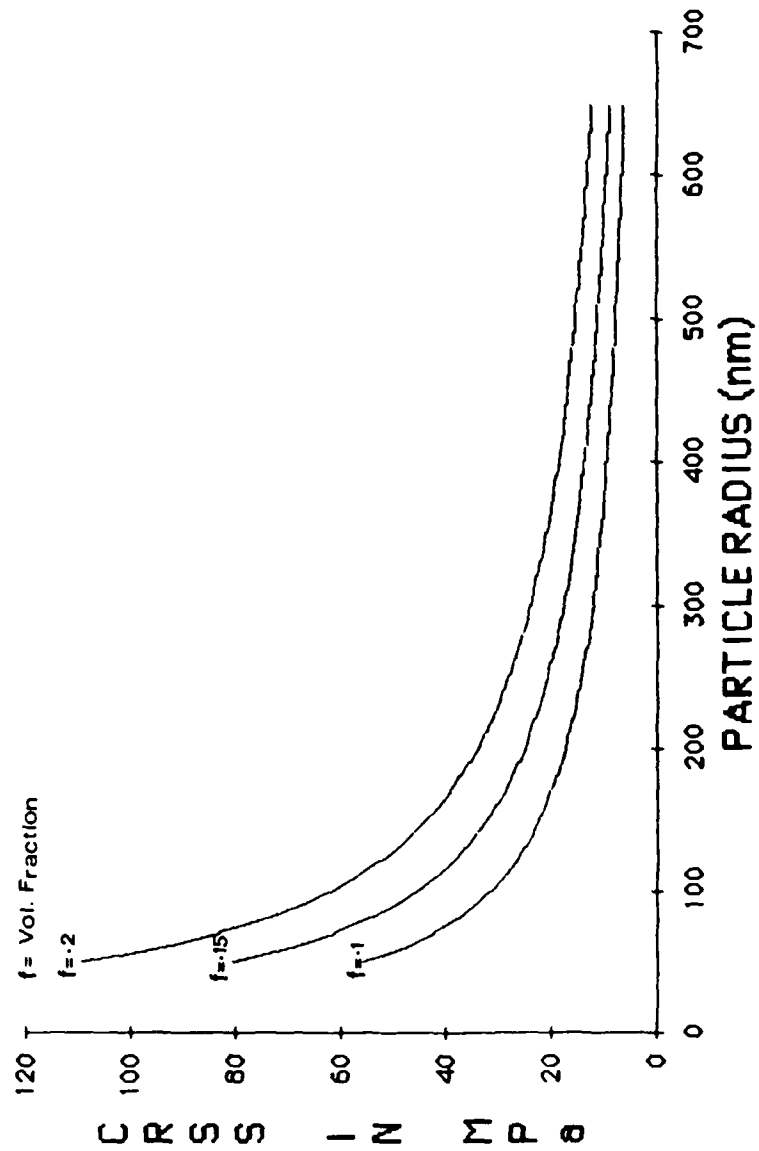


Figure 62 Plot of Increase in critical resolved shear stress with increasing volume fraction and particle size.

DISTRIBUTION LIST

Report No. NADC-86074-60

	No. of Copies
NAVAIRSYSCOM, Washington, DC 20361 (AIR-0004)	14
(2 for retention)	
(2 for AIR-530)	
(1 for AIR-320B)	
(1 for AIR-52032D)	
(1 for AIR-5302)	
(1 for AIR-53021)	
(1 for AIR-530215)	
(5 for AIR-5163D3)	
NAVSEASYSYSCOM, Washington, DC 20362	1
NAVAIRTESTCEN, Patuxent River, Maryland	1
NAVAVNSAFECEN, NAS, Norfolk, Virginia	1
NAVSHIPPRANDCEN, Bethesda, Maryland 20034	1
NAVSHIPPRANDCEN, Annapolis, Maryland 21402	1
NRL, Washington, DC 20375	2
(1 for Code 6120)	
(1 for Code 6306)	
ONR, Washington, DC 20350	2
(1 for Code 431, Dr. S. Fishman)	
(1 for Code 472)	
NAVAIREWORKFAC, NAS, Alameda (Code 340), California	1
NAVAIREWORKFAC, NAS, Jacksonville (Code 340), Florida	1
NAVAIREWORKFAC, NAS, Norfolk (Code 340), Virginia	1
NAVAIREWORKFAC, NAS, North Island (Code 340), California.	1
NAVAIREWORKFAC, NAS, Pensacola (Code 340), Florida	1
NAVAIREWORKFAC, MCAS, Cherry Point (Code 340), North California.	1
USAF SYSTEMS COMMAND, WPAFB, Ohio 45433	
(Attn: FBR)	1
(Attn: FB)	1
(Attn: LLD)	1
(Attn: FYA)	1
(Attn: LAM)	1
(Attn: FBA)	1
(Attn: LPH)	1
(Attn: FDTCT)	1

	No. of Copies
(Attn: LC)	1
(Attn: LN)	1
(Attn: LTF)	1
(Attn: LAE)	1
(Attn: MBC)	1
Naval Air Propulsion Test Center	1
Trenton, NJ 08628	
Attn: Mr. J. Glatz	
Naval Weapons Center	1
China Lake, CA 92555	
Naval Ship Engineering Center	1
Washington, DC 20360	
Attn: Code 6101E	
Drexel University	10
Philadelphia, PA 19104	
Attn: Dr. M.J. Koczak)	
Defense Technical Information Center	12
Cameron Station, Bldg. 5	
Alexandria, VA 22314	
Vought Corporation	1
Systems Division	
P.O. Box 6907	
Dallas, TX 75222	
Attn: G. Bourland	
NASA Headquarters	1
600 Independence Avenue, S.W.	
Washington DC 20546	
Attn: Code RV-2	
Mr. N. Mayer	
The Boeing Company	1
Aerospace Division	
P.O. Box 3707	
Seattle, WA 98124	
Boeing-Vertol Company	1
P.O. Box 16858	
Philadelphia, PA 19142	
Attn: Dept. 1951	

	No. of Copies
Naval Ordnance Laboratory Code 234 White Oak, Silver Spring, MD 20910	1
Defense Ceramic Information Center Battelle Memorial Institute 505 King Avenue Columbus, OH 43201	1
Illinois Institute of Technology Research Institute 10 West 35th Street Chicago, IL 60616 Attn: Dr. E. Hofer	1
Brunswick Corporation Technical Products Division 325 Brunswick Lane Marion, VA 24354	1
Acurex Aerospace Systems Division 485 Clyde Avenue Mountain View, CA 94042	1
Grumman Aerospace Corporation Bethpage, NY 11714 Attn: J. Mahon	1
AVCO Corporation Applied Technology Division Lowell, MA 01851	1
North American Aviation Columbus Division 4300 E. Fifth Avenue Columbus, OH 43216	1
Rockwell International Corporation 12214 Lakewood Blvd. Downey, CA 90241 Attn: M.C.R. Rousseau	1
McDonnell-Douglas Corporation P.O. Box #516 St. Louis, MO 63166 Attn: Mr. G. Bilow	1

	No. of Copies
General Electric Company Valley Forge Space Center Philadelphia, PA 19101	1
Materials Sciences Corporation 1777 Walton Road Blue Bell, PA 19422	1
U.S. Army Air Mobility R&D Laboratory Fort Eustis, VA 23064 Attn: SAVDL-EU-SS (Mr. J. Robinson)	1
McDonnell-Douglas Corporation McDonnell Aircraft Company P.O. Box 516 St. Louis, MO 63166 Attn: Mr. R. Juergens Dr. J. Carpenter	2
Fibers Materials, Inc Biddeford Industrial Park Biddeford, ME 04005 Attn: Mr. J. Herrick	1
Mr. M. Krenzke (Code 1720) David W. Taylor Naval Ship R&D Center Bldg. #19 Bethesda, MD 20084	1
NASA Langley Research Center Hampton, VA 23365 Attn: W. Howell	1
United Aircraft Corporation United Aircraft Research Labs. E. Hartford, CT 06108	1
United Aircraft Corporation Pratt & Whitney Aircraft Division East Hartford, CT 06108	1
United Aircraft Corporation Hamilton-Standard Division Windsor Lock, CT 06096 Attn: Mr. T. Zajac	1

	No. of Copies
United Aircraft Corporation Sikorsky Aircraft Division Stratford, CT 06602 Mr. J. Ray	1
Philco-Ford Corporation Aeronutronic Division Ford Road Newport Beach, CA 92663	1
University of Maryland College Park, MD 20742 Attn: Dr. W.J. Bailey	1
B.F. Goodrich Aerospace & Defense Products 500 South Main Street Akron, OH 44318	1
Lockheed-Georgia Company Marietta, GA 30063 Attn: Mr. L.E. Meade	1
Lockheed Missiles & Space Company Sunnyvale, CA 94088 Attn: Dr. D. Webster Dept. 81-35	1
TRW, Inc. 23555 Euclid Avenue Cleveland, OH 44117	1
E.I. DuPont de Nemours & Company Textile Fibers Dept. Wilmington, DE 19898	1
Bell Aerospace Company Buffalo, NY 14240 Attn: Mr. F.M. Anthony	1
Union Carbide Corporation Chemicals & Plastics One River Road Bound Brook, NJ 08805	1
General Dynamics Convair Aerospace Division P.O. Box 748 Fort Worth, TX 76101 Attn: Tech. Library	1

	No. of Copies
General Dynamics Convair Division P.O. Box 1128 San Diego, CA 92138 Attn: Mr. W. Scheck Dept. 571-10	1
TRW, Inc. Systems Group One Space Park, Bldg. 61, Rm. 2171 Redondo Beach, CA 90278	1
University of Wyoming Mechanical Engineering Dept. Laramie, WY 82071 Attn: Dr. D.F. Adams	1
Army Materials & Mechanics Research Center Polymers & Chemistry Division Watertown, MA 02172 Attn: G.L. Hagnauer R.E. Sacher	2
Mercules, Inc. Magna, UT 84044 Attn: R.E. Hoffman	1
E.I. DuPont Company Instrument Products Division Concord Plaza Wilmington, DE 19898 Attn: R.L. Blaine	1
General Electric R&D Center Box #8 Schenectady, NY 12301 Attn: Mr. W. Hillig	1
Stanford Research Institute 333 Ravenwood Avenue Bldg. #102B Menlo Park, CA 94025 Attn: Mr. M. Maximovich	1
University of California Lawrence Livermore Laboratory P.O. Box 808 Livermore, CA 94550 Attn: Mr. T.T. Chiao	1

	No. of Copies
Northrop Corporation	1
3901 W. Broadway	
Hawthorne, CA 90250	
Attn: R.L. Jones	
Dept. 3870-62	
Pratt & Whitney R&D Center	1
United Aircraft Corporation	
West Palm Beach, FL 33402	
Attn: Dr. J. Winfree	
NAVAIRDEVCE	13
(3 for Code 8131)	
(10 for Code 6063)	

END

2-87

DTic